COLLISIONS OF ROUND BEAMS AT THE CORNELL ELECTRON STORAGE RING IN PREPARATION FOR MÖBIUS OPERATION

A Dissertation

Presented to the Faculty of the Graduate School

of Cornell University

in Partial Fulfillment of the Requirements for the Degree of

Doctor of Philosophy

by

Elizabeth Marie Young

January 1998

COLLISIONS OF ROUND BEAMS AT THE CORNELL ELECTRON STORAGE RING IN PREPARATION FOR MÖBIUS OPERATION

Elizabeth Marie Young, Ph.D.

Cornell University 1998

Colliding round, rather than flat, beams promises to more than double the luminosity of electron-positron colliders. In simulations, round beams have been capable of producing large tune shifts, much greater than produced by flat beams, with acceptable beam blowup. The purpose of this work was to demonstrate experimentally the promise of round beams (made round by the coupling resonance) and to prepare for the installation of a Möbius insert (a group of skew quadrupoles that exchange horizontal and vertical motion on every turn) at the Cornell Electron Storage Ring. During the collision experiments, three interrelated measures of colliding beam performance, the emittance blowup, the beam-beam tune shift parameter, and the coherent π mode tune shift, were measured as functions of beam current and tune, and the luminosity was also measured at the highest beam currents. The results of these measurements confirm that round beams are capable of producing very large tune shifts and justify continued development of the Möbius scheme.

BIOGRAPHICAL SKETCH

Elizabeth Marie Young was born on October 9, 1967 in Dodge City, Kansas. She graduated from Dodge City Senior High School in May 1986 after being voted "Most Likely to Attend Graduate School" by her classmates; however they made no mention of when she might be expected to finish. She continued her education at the University of Kansas in Lawrence, Kansas and graduated in May 1990 with a Bachelor of Science degree in physics. She arrived in Ithaca, New York in August 1990 to pursue a graduate degree in physics at Cornell University. She completed her master's thesis and received a Master of Science degree in January 1995.

To Dan

ACKNOWLEDGMENTS

Rarely is a Ph.D. dissertation the product of one person working alone. It would not have been possible for me to complete my degree without the help of a number of people.

I think that the degree to which one enjoys graduate school is highly dependent on one's advisor, and I feel fortunate to have been in the right place at the right time to work with Richard Talman. His support, enthusiasm, participation, and guidance throughout this project has been invaluable.

It seems like nearly everyone in the CESR operations group has at one point or another lent a hand with the round beam studies. I thank David Rubin for granting generous amounts of machine studies time and also for serving on my advisory committee. I am particularly grateful to all those who spent long hours in the control room helping make round beam collisions happen, especially Stuart Henderson, Raphael Littauer, and Tom Pelaia. I am also indebted to Stu Peck, Mike Billing, Dave Sagan, and the CESR operators for their assistance in commissioning the round beam lattices.

I thank the Debbie Hatfield, Monica Norris, Tom Allen and the rest of the office staff in the Physics Department, Laboratory of Nuclear Studies, and Wilson Synchrotron Laboratory for helping me deal with all of Cornell's bureaucratic nonsense.

I could not have survived graduate school without the help of my friends. To the CESR graduate students, Cheng-Yang Tan, Scott Smith, Kern Ormond, Dan Fromowitz, and Edwin Anderson, and all the other attendees of the Willy Club, thank you for entertaining and educational diversions as well as for making my defense seem like a piece of cake. I thank the Monday dinner crowd, Ken Bloom, Bruce Berger, Francesca Pardo, Rolf Ragnarsson, and Kristin Ringland, for getting me out of the lab at least once a week. To Jens and Veronique Knobloch, thank you for putting up with Dan's and my video selections, and to Sören and Konstanze Prell, thank you for many enjoyable discussions over wine and brie.

I could not have made it to graduate school in the first place without the support of my family. Thank you for your patience as it probably seemed like I would never finish.

Finally, I want to thank Dan Bliss, but I hardly know where to begin. Thanks for stubbornly refusing to stay in California. Thanks for telling me the things I needed to hear, even the things that I sometimes did not want to hear. Thanks for putting a smile on my face.

Ithaca, New York *Elizabeth Marie Young*

September 4, 1997

TABLE OF CONTENTS

LIST OF TABLES

LIST OF FIGURES

Chapter 1
Introduction

The Cornell Electron Storage Ring (CESR) collides nine trains of two bunches each of electrons and positrons in the CLEO-II detector, usually at a center of mass energy of about 10.6 GeV, the $\Upsilon(4S)$ resonance, which is just above the threshold for the production of b quarks. Many current topics of research in the CLEO collaboration, such as CP violation in the decay of B mesons and the study of rare B decays, require large numbers of electron-positron interactions in order to accumulate a statistically significant number of events for these processes. In accelerator terminology, events per unit time per event cross section is called luminosity, $\mathcal{L}$. As of May 1997, the peak luminosity is $\mathcal{L}_{peak} = 4.1 \times 10^{32}$ cm^{-2}s^{-1}, and after the Phase III upgrade of CESR, it is expected to increase to $\mathcal{L}_{peak} > 10^{33}$ cm^{-2}s^{-1}, but for this facility to remain competitive in high energy physics, further upgrades will be needed.

1.1 Definitions of Common Terms and Symbols

As electrons and positrons circulate in CESR, they do not travel in a perfectly circular trajectory. Instead, they oscillate back and forth in the horizontal and vertical directions as they circulate, as illustrated in Figure 1.1, and the number of oscillations per revolution is called the tune, Q. The square of the amplitude of those oscillations is proportional to the β-function, $\beta(s)$, which is a function of the longitudinal position, s. Throughout this dissertation the horizontal and vertical β-functions at the interaction point (IP) in the CLEO-II detector are designated by a superscript asterisk, *i.e.* β_x^*, β_y^*. The β-functions also relate the horizontal and vertical sizes of the bunch distributions, σ_x and σ_y, to something called the emittance, $\sigma^2 = \beta\varepsilon$. The horizontal and vertical emittances, ε_x and ε_y, are proportional to the areas occupied by the bunch in x-x' and y-y' phase space, as illustrated in Figure 1.2, where $x' \equiv \frac{dx}{ds}$ and $y' \equiv \frac{dy}{ds}$ are the horizontal and vertical slopes of the particle trajectory. The emittances are the same everywhere in the ring, so the beam sizes vary with longitudinal position, and as with the β-functions, a superscript asterisk indicates the values at the IP, *i.e.* σ_x^*, σ_y^*.

The interaction rate per interaction cross section is called the luminosity. Assuming equal numbers of electrons and positrons in each bunch, the luminosity for a Gaussian particle distribution is

$$\mathcal{L} = \frac{1}{4\pi e^2 f} \frac{I^2}{\sigma_x^* \sigma_y^*}, \tag{1.1}$$

where e is the unit charge, f is the frequency of bunch collisions (equal to the revolution frequency for one bunch per beam), and I is the current per bunch. This formula is often rearranged as

$$\mathcal{L} = \frac{\gamma_0}{2er_e} \frac{\xi_y I}{\beta_y^*} \left(1 + \frac{\sigma_y^*}{\sigma_x^*}\right), \tag{1.2}$$

where r_e is the classical electron radius, $\gamma_0 = E/mc^2$, and ξ_y, called the vertical beam-beam tune shift parameter, parameterizes the strength of the force felt by individual particles of one bunch due to the electromagnetic fields of the opposing bunch as they collide. The beam-beam tune shift parameter will be discussed in

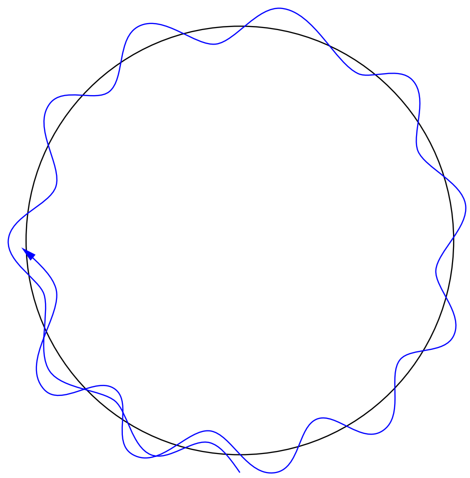

Figure 1.1: An example of single particle motion in a storage ring. The number of oscillations per revolution is called the tune, Q, and the square of the envelope of the particle trajectory is proportional to $\beta(s)$, the β-function.

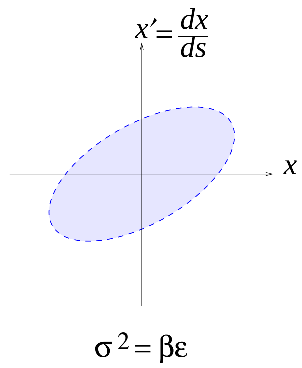

Figure 1.2: An example of a phase space plot. The area of the ellipse in phase space contains a fraction of the particles. For electron/positron machines, the convention is $\sigma^2 = \beta\varepsilon$, where σ is the standard deviation of a Gaussian distribution.

more detail in Chapter 2. In terms of other parameters, the vertical beam-beam tune shift parameter is

$$\xi_y = \frac{r_e}{2\pi e f \gamma_0} \frac{\beta_y^* I}{\sigma_y^*(\sigma_x^* + \sigma_y^*)}. \tag{1.3}$$

The meaning of this equation will be discussed further in the next section.

In most electron/positron storage rings, the dipole and quadrupole fields that guide the beam are aligned so that ideally the horizontal and vertical motions of the particles are independent of each other. Because storage rings generally lie in a horizontal plane, synchrotron radiation excites only horizontal motion, so electron/positron beams tend to have $\varepsilon_y \ll \varepsilon_x$. In addition, CESR is designed so that $\beta_y^* \ll \beta_x^*$, so the bunches have ribbon-like cross sections when they collide, $\sigma_y^* \ll \sigma_x^*$. By changing the ratios of the horizontal and vertical emittances and β-functions at the IP, the aspect ratio of the colliding bunches can be manipulated and made round. A strict definition of round beams is used in this dissertation, namely $\varepsilon_x = \varepsilon_y$ and $\beta_x^* = \beta_y^*$ so that $\sigma_x^* = \sigma_y^*$.

1.2 The Promise of Round Beams

During normal operation of CESR, flat beams are collided, and by decreasing β_y^*, increasing I, and minimizing sources of horizontal to vertical coupling that would otherwise increase the vertical beam size, CESR has been able to achieve record luminosity. Why then would one want to consider round beams, particularly beams made round through coupling, which is undesirable during flat beam operation? First, if one examines Equation 1.2, there is an automatic factor of two in going from flat to round because

$$
\begin{aligned}
\left(1+\frac{\sigma_y^*}{\sigma_x^*}\right) &\simeq 1 \text{ for flat beams,} \\
\left(1+\frac{\sigma_y^*}{\sigma_x^*}\right) &= 2 \text{ for round beams,}
\end{aligned}
\tag{1.4}
$$

all other things being equal. However, the primary potential advantage of round beams is their stability, particularly their stability against the detrimental effects of the beam-beam interaction. The electromagnetic beam-beam force has a tendency to increase the beam size as the current per bunch increases, which places limits on the maximum achievable beam-beam tune shift parameter and on the maximum achievable luminosity. At CESR, $\xi_y^{max} \simeq 0.04$ typically. However, in simulations round beams are capable of producing much higher tune shifts, $\xi^{max} > 0.1$, before becoming limited by the beam blowup[1, 2].[1]

1.3 An Overview of the Experiment

The reasons stated above were sufficient to motivate experimental investigation of round beams. Two methods of making round beams were considered: resonant coupling and the Möbius insert. By moving the horizontal and vertical tunes to a strong but stable resonance, $Q_x - Q_y = n$ where n is an integer, existing skew quadrupoles (quadrupoles rotated about their axes by 45° relative to normal quadrupoles) in CESR can be used to exchange horizontal and vertical motion on the order of 100's of revolutions, which is sufficient to make the beams round. A Möbius insert[1] consists of a section of five or six skew quadrupoles that are arranged so that $x \leftrightarrow y$ every time the bunch passes through that section. The Möbius scheme holds the most promise; however, it required a non-trivial modifi-

[1] Additional benefits, such as chromaticity sharing, are expected for beams made round by the Möbius scheme[1, 3], but this effect is beyond the scope of this dissertation.

cation of CESR, so the decision was made to use resonant coupling for preliminary studies of round beam collisions so that the promise of round beams could be explored as far as possible with minimal disruption of CESR providing a baseline for comparison with future Möbius experiments.

Colliding round beams in CESR was attempted previously in 1989-1990[4]. At that time there were two high energy experiments at CESR – CLEO-II at the south interaction point (SIP) and CUSB at the north interaction point (NIP).[2] The plan for this earlier round beam experiment had been to collide in the north only, first using "flat" beams ($\varepsilon_y \ll \varepsilon_x$ with nearly equal β at the collision point), then using fully coupled beams. Unfortunately, the first phase of the experiment was plagued with problems, and the second phase was never completed, although a few runs with coupled beams were done.

The plan for the experiments described in this dissertation was to collide resonantly coupled round beams at the SIP. Existing skew quadrupoles were used to couple the horizontal and vertical motions and make $\varepsilon_x = \varepsilon_y$. As was stated in Section 1.2, switching to round beams is expected to increase luminosity by an automatic factor of two and another factor of two from the increase in ξ^{max} *all other things being equal*, such as I and β_y^*. However, when the present interaction region (IR) was designed, the positions and polarities of the IR quadrupoles were chosen so that $\beta_y^* \ll \beta_x^*$ would be easy with the consequence that making $\beta_y^* = \beta_x^* = \beta^*$ was possible only for relatively large β^*. Furthermore, the plan was to collide a single bunch of electrons with a single bunch of positrons, which simplifies the interpretation of results but reduces the total current possible. While these factors limited achievable luminosity, the beam-beam tune shift parameter

[2] CUSB was dismantled in the fall of 1990.

for round beams is independent of β^*,

$$\xi = \frac{r_e}{4\pi e f \gamma_0} \frac{I}{\varepsilon}, \tag{1.5}$$

so it became the focus of the collision experiments, along with the beam size blow up, which eventually limits ξ, and the coherent π mode, another manifestation of the beam-beam interaction. The beam-beam interaction couples the colliding beams in a way that is analogous to a spring coupling two pendulums and can produce coherent beam-beam modes. One, called the σ mode, corresponds to the beams oscillating in phase at the collision point at the betatron tune. The other, called the π mode, corresponds to the beams oscillating 180° (*i.e.* π) out of phase. The frequency of the coherent π mode is higher than the single beam tune by an amount that is directly related to ξ.

1.4 Dissertation Outline

The contents of the remainder of this dissertation are as follows. Chapters 2 through 5 provide background material and additional details concerning the beam-beam interaction, round beams, and the experimental conditions. Beam-beam phenomena and their effects on colliding beam performance are discussed in Chapter 2, where most of formulas that are used in analyzing the colliding beam data are derived. A previously published theory for correlating the coherent π mode tune shift and beam-beam tune shift parameter is also described. Chapter 3 contains descriptions of two methods of making round beams – resonant coupling, which was the method used in these experiments, and the Möbius insert. The additional constraints on resonantly coupled round beam lattice design and Möbius lattice design imposed by the layout of CESR are discussed in Chapter 4. In preparation for these experiments, simulations were done by myself and my colleagues, and these are described in Chapter 5. In Chapter 6 the measurement methods are described, and the results are presented along with some interpretation. Measurements of the coherent π mode tune shift at various bunch currents were correlated with independent measurements of the beam-beam tune shift parameter, and the correlation was compared with the theory that was described in Chapter 2. The beam blowup and beam-beam tune shift parameters were also measured as a function of tune for unequal beam currents. Finally, although luminosity was not the focus, it was measured at the highest currents to verify the current and emittance measurements. Chapter 7 contains some final thoughts and possible avenues for further research. Supplementary material is provided in the appendices. Details of the projection approach to coupling as it applies to solenoid compensation are in Appendix A, and Appendix B contains tables of representative data and the corresponding beam profiles and spectra.

Chapter 2
Beam-Beam Phenomena

2.1 Luminosity

Ultimately, the important quantity for a collider is the amount of data it produces per unit time. If N_1 particles in one bunch collide with N_2 particles in the opposing bunch and the collision takes place within an area, A, then the rate for a particular interaction is $R = f\frac{N_1 N_2}{A}\sigma_{\mathrm{int}}$, where f is the frequency of collision and σ_{int} is the interaction cross section. Since physicists are interested in many different processes each with a different cross section, a more general measure of collider performance is interaction rate per interaction cross section, called luminosity, $\mathcal{L} = f\frac{N_1 N_2}{A}$.

For a distribution of particles, especially if the distributions are not the same for both bunches, the calculation of A is somewhat complicated, but can be completed in closed form for Gaussian distributions. The number of particles in small ring of width dr at radius r from the center of the a round Gaussian bunch is

$$dn(r) = \frac{N}{\sigma^2} e^{-r^2/2\sigma^2} r\ dr. \tag{2.1}$$

The area of that ring is $2\pi r\ dr$, so the contribution to the total luminosity is

$$\begin{aligned} d\mathcal{L} &= f\frac{dn_+ dn_-}{2\pi r\ dr} \\ &= \frac{f}{2\pi}\frac{N_+ N_-}{{\sigma_+^*}^2 {\sigma_-^*}^2} \exp\left[-\frac{r^2}{2}\left(\frac{1}{{\sigma_+^*}^2} + \frac{1}{{\sigma_-^*}^2}\right)\right] r\ dr. \end{aligned} \tag{2.2}$$

Thus, the total luminosity is

$$\mathcal{L} = \frac{f}{2\pi} \frac{N_+ N_-}{{\sigma_+^*}^2 {\sigma_-^*}^2} \int_0^\infty \exp\left[-\frac{r^2}{2}\left(\frac{1}{{\sigma_+^*}^2} + \frac{1}{{\sigma_-^*}^2}\right)\right] r\ dr,$$
$$= \frac{I_+ I_-}{2\pi e^2 f \beta^* (\varepsilon_+ + \varepsilon_-)}, \tag{2.3}$$

where $I = efN$. For $N_+ = N_-$ and $\sigma_+^* = \sigma_-^*$

$$\mathcal{L} = \frac{I^2}{4\pi e^2 f \beta^* \varepsilon}, \tag{2.4a}$$
$$= \frac{\gamma}{e r_e} \frac{\xi I}{\beta^*}, \tag{2.4b}$$

where ξ is the beam-beam tune shift parameter for round beams,

$$\xi = \frac{r_e}{4\pi e f \gamma_0} \frac{I}{\varepsilon}. \tag{2.5}$$

ξ parameterizes the strength of the electromagnetic beam-beam force, and it is discussed in more detail in the next section.

2.2 The Beam-Beam Tune Shift Parameter

Consider a round, Gaussian beam of n electrons traveling at relativistic speeds, $v/c \sim 1$. From Gauss' Law and the symmetry of the charge distribution, the transverse electric field of the beam is

$$E_r(r)\hat{\mathbf{r}} = -\frac{e\ n}{2\pi\epsilon_0}\left[1 - \exp\left(-\frac{r^2}{2\sigma^2}\right)\right]\frac{\hat{\mathbf{r}}}{r}, \tag{2.6}$$

where r is the transverse distance from the center of the beam, σ is the transverse standard deviation of the particle distribution, and ϵ_0 is the permitivity of free space. Similarly, the magnetic field is

$$B_\phi(r)\hat{\phi} = -\frac{e\ n\ v}{2\pi\mu_0}\left[1 - \exp\left(-\frac{r^2}{2\sigma^2}\right)\right]\frac{\hat{\phi}}{r}, \tag{2.7}$$

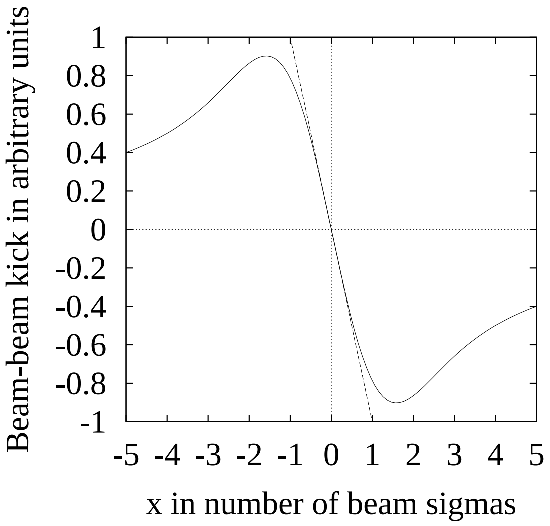

Figure 2.1: $\Delta x'$, Equation 2.8, in arbitrary units as a function of x/σ (solid line) and the linear approximation, Equation 2.10 (dashed line).

where μ_0 is the permeability of free space. It is usual to talk of the slope of a particle's trajectory, $x' \equiv dx/ds$ where s is the longitudinal coordinate, rather than its transverse momentum. Converting the Lorenz force, $\vec{\mathbf{F}} = e(\vec{\mathbf{E}} + \vec{\mathbf{v}} \times \vec{\mathbf{B}})$, to an angular deflection, or kick, and integrating over the bunch length, the change of slope of a positron's trajectory at a distance r from the center of the electron bunch is

$$\Delta x' = -\frac{2Nr_e}{\gamma_0}\left[1 - \exp\left(-\frac{r^2}{2\sigma^2}\right)\right]\frac{x}{r^2}, \tag{2.8}$$

where N is the total number of particles in the electron beam, r_e is the classical electron radius, and $\gamma_0 = E/mc^2$. Figure 2.1 shows $\Delta x'$ in arbitrary units as a function of x/σ.

Assuming that the displacement of the positron from the center of the electron bunch is small compared to σ, then the exponential can be approximated by the

Taylor series expansion

$$\exp\left(-\frac{r^2}{2\sigma^2}\right) = 1 - \left(-\frac{r^2}{2\sigma^2}\right) + \cdots, \tag{2.9}$$

and Equation 2.8 becomes

$$\Delta x' = -\frac{N r_e}{\gamma_0}\frac{x}{\sigma^2} = -\frac{x}{f}, \tag{2.10}$$

which is also plotted in Figure 2.1. A similar equation applies to $\Delta y'$. Thus, for small amplitude particles the beam-beam interaction is like a gradient error, and the tune of small amplitude particles is modified by the standard equation[5]

$$\cos 2\pi Q = \cos 2\pi Q_0 - 2\pi\xi \sin 2\pi Q_0, \tag{2.11}$$

where $Q_0 + \Delta Q = Q$ and ξ is the linear beam-beam tune shift parameter defined as ($\sigma^2 = \varepsilon\beta$)

$$\xi \equiv \frac{\beta^*}{4\pi f} = \frac{r_e}{4\pi\gamma_0}\frac{N}{\varepsilon}. \tag{2.12}$$

For small tune shifts, Equation 2.11 simplifies to $\Delta Q = \xi$, so ξ is just the tune shift of small amplitude particles due to the beam-beam interaction, which is the basis for calling ξ the "tune shift parameter."

Equations 2.12 and 2.4 predict that the beam-beam tune shift parameter increases linearly with beam current and that the luminosity increases as the square of the beam current. However, data from various colliders indicates that the beam sizes also increase with current so that the luminosity does not quite increase as the square of the beam current. At some point the beam-beam interaction increases the beam size enough so that the (vertical, since electron/positron colliders presently operate with flat beams) tune shift parameter saturates, and the luminosity becomes linear with current, as shown in Figure 2.2. Beyond the saturation point, the beam sizes continue to grow, and non-Gaussian tails may develop, limiting the maximum luminosity due to the resulting poor lifetime[6]. These effects of the beam-beam interaction cannot be addressed analytically and are usually examined using simulations. Simulations of round beams have indicated that they are more resistant to the detrimental effects of the beam-beam interaction and thus are capable of achieving higher tune shift parameters than flat beams, $\xi > 0.01$, before reaching the saturation point. Various beam-beam simulations, past and present, and their results will be discussed in more detail in Chapter 5.

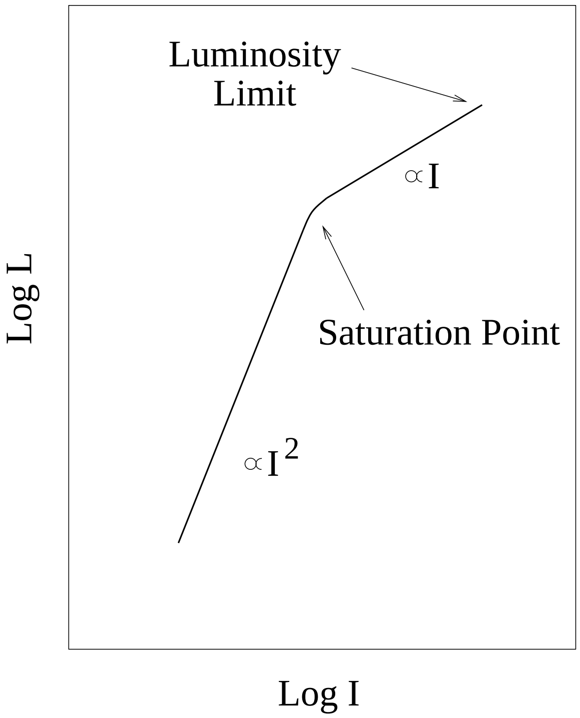

Figure 2.2: The dependence of the luminosity on beam current. At low beam currents, beam blowup is minimal and $\mathcal{L} \propto I^2$. Beyond the saturation point, the beam size increases with current such that the tune shift parameter is constant, and thus luminosity becomes linear with current. Eventually, the tails of the beam distribution are sufficiently large that the lifetime is significantly reduced.

2.3 The Coherent π Mode

2.3.1 Simple Coupled Pendulums

A way of conceptualizing the coherent motion of two beams in collision is by analogy to simple coupled pendulums, such as those shown in Figure 2.3. The equations of motion for small amplitude motion when the spring is absent are

$$\ddot{\theta}_{1,2} = -\omega_0^2\theta_{1,2}, \qquad \omega_0^2 = \frac{g}{l}, \tag{2.13}$$

where g is the acceleration due to gravity. When the pendulums are coupled via a spring with spring constant k, the equations of motion become

$$\ddot{\theta}_1 = -\omega_0^2\theta_1 - \frac{k}{m_1}(\theta_1 - \theta_2), \tag{2.14a}$$

$$\ddot{\theta}_2 = -\omega_0^2\theta_2 - \frac{k}{m_2}(\theta_2 - \theta_1). \tag{2.14b}$$

For the case $m_1 = m_2$, after diagonalizing the equations,

$$\ddot{\theta}_\sigma = -\omega_\sigma^2\theta_\sigma, \quad \omega_\sigma^2 = \omega_0^2, \tag{2.15a}$$

$$\ddot{\theta}_\pi = -\omega_\pi^2\theta_\pi, \quad \omega_\pi^2 = \left(\omega_0^2 + \frac{2k}{m}\right), \tag{2.15b}$$

where $\theta_\sigma = \theta_1 + \theta_2$ and $\theta_\pi = \theta_1 - \theta_2$. θ_σ corresponds to the pendulums oscillating in phase, and θ_π corresponds to them oscillating 180° out of phase. For weak coupling,

$$\omega_\pi = \omega_0\left(1 + \frac{2k}{m\omega_0^2}\right)^{\frac{1}{2}} \simeq \omega_0 + \frac{k}{m\omega_0}. \tag{2.16}$$

Notice that the σ mode oscillates at the same frequency as the uncoupled pendulums while the π mode oscillates with a higher frequency, and the difference, $\Delta\omega = k/m\omega_0$, is proportional to the strength of the spring.

Similarly, when particle beams are in collision, their horizontal oscillations are analogous to the two pendulums, and the beam-beam interaction is analogous

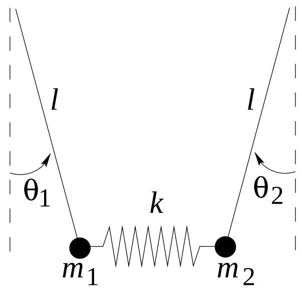

Figure 2.3: Coupled simple pendulums. The two normal modes of motion are the σ mode, in which the pendulums swing in phase, and the π mode, in which the pendulums swing 180° out of phase.

to the spring. Thus, the colliding electron and positron beams will have two modes of coherent motion, one at the single beam tune, Q_x, and one at a higher frequency, $Q_x + \Delta Q_\pi$. The vertical motion of the beams is analogous to a second pair of coupled pendulums, so there will be a vertical σ mode and a vertical π mode as well. Since the strength of the "spring," *i.e.* the beam-beam interaction, determines the size of the frequency shift, and since the strength of the beam-beam interaction is parameterized by ξ, it is reasonable to expect that the coherent π mode tune shift, ΔQ_π, and ξ will be proportional to one another,

$$\Delta Q_\pi = \lambda \xi, \tag{2.17}$$

where λ is called the "derating factor" and will be calculated in the following sections.

2.3.2 A Simple Model

Returning to particle beams to calculate λ, consider the bunch as a "macro-particle."[7, 8] The turn-by-turn evolution of the horizontal coordinates of the bunch, (x, x'), at a particular longitudinal position in the storage ring is described in general by a two 2×2 transfer matrix (assuming no x-y coupling),

$$\mathbf{M}_x = \begin{pmatrix} \cos\mu_x + \alpha_x \sin\mu_x & \beta_x \sin\mu_x \\ -\gamma_x \sin\mu_x & \cos\mu_x - \alpha_x \sin\mu_x \end{pmatrix}, \tag{2.18}$$

where $\alpha \equiv \frac{1}{2}\frac{d\beta}{ds}$, $\beta\,\gamma \equiv \alpha^2 + 1$ and $\mu \equiv 2\pi Q$. The evolution backwards in time is described by $\mathbf{M}^{-1}$, and the same is true for $x \to y$. The relationship between the horizontal coordinates at the collision point on three successive turns, $t-1$, t, and $t+1$, with a beam-beam kick, $\Delta x'$, on each turn is given by

$$\begin{pmatrix} x_{t+1} \\ x'_{t+1} - \Delta x'_{t+1}/2 \end{pmatrix} = \mathbf{M}_x \begin{pmatrix} x_t \\ x'_t + \Delta x'_t/2 \end{pmatrix}, \tag{2.19a}$$

$$\begin{pmatrix} x_{t-1} \\ x'_{t-1} + \Delta x'_{t-1}/2 \end{pmatrix} = \mathbf{M}_x^{-1} \begin{pmatrix} x_t \\ x'_t - \Delta x'_t/2 \end{pmatrix}, \tag{2.19b}$$

which can be rearranged into the useful equation

$$x_{t+1} - 2x_t \cos 2\pi Q_0 + x_{t-1} = \beta \Delta x'_t \sin 2\pi Q_0, \tag{2.20}$$

where Q_0 is the tune of the unperturbed bunch. Similar equations can be written for motion in the y-plane.

When colliding, if the centers of the distributions are offset, each beam feels a kick from the other. For small amplitude motion the angular deflection of the positron/electron trajectory is given by Equation 2.10 with x replaced by the distance between the centers of the bunches,

$$\Delta x'_{\pm} = -\frac{4\pi}{\beta}\xi_{\pm}(x^{\pm} - x^{\mp}), \tag{2.21}$$

where $x^{\pm}$ is the location of the center of the positron/electron bunch. The subscripts on Δx and ξ refer to the particle receiving the kick, and the linear beam-beam tune shift parameters experienced by each beam are no longer assumed to be the same (for example, $N_+ \neq N_-$),

$$\xi_\pm = \frac{N_\mp r_e}{4\pi\gamma_0\varepsilon_\mp}. \tag{2.22}$$

Substituting this into Equation 2.20, the perturbed equations of motion for the bunches are

$$x^+_{t+1} - 2(\cos 2\pi Q_0)x^+_t + x^+_{t-1} = -4\pi\xi_+(\sin 2\pi Q_0)(x^+_t - x^-_t), \tag{2.23a}$$

$$x^-_{t+1} - 2(\cos 2\pi Q_0)x^-_t + x^-_{t-1} = -4\pi\xi_-(\sin 2\pi Q_0)(x^-_t - x^+_t), \tag{2.23b}$$

which bear much resemblance to Equations 2.14. These equations can be diagonalized by using the normal mode variables $\Sigma = x^+ + x^-$ and $\Pi = x^+ - x^-$,

$$\Sigma_{t+1} - 2(\cos 2\pi Q_0)\Sigma_t + \Sigma_{t-1} = 0, \tag{2.24a}$$

$$\Pi_{t+1} - 2(\cos 2\pi Q_\pi)\Pi_t + \Pi_{t-1} = 0, \tag{2.24b}$$

and the frequency of the coherent π mode of oscillation, $Q_\pi = Q_0 + \Delta Q_\pi$, is

$$\cos 2\pi(Q_0 + \Delta Q_\pi) = \cos 2\pi Q_0 - 2\pi(\xi_+ + \xi_-)\sin 2\pi Q_0. \tag{2.25}$$

For small tune shifts and $\xi_+ = \xi_-$, this equation simplifies to

$$\Delta Q_\pi = \lambda\xi, \quad \text{with} \quad \lambda = 2 \tag{2.26}$$

2.3.3 An Improved Model

Measurements have shown that $\lambda = 2$ is wrong by roughly a factor of two at CESR[6]. The approach of the previous section assumed that each bunch could be treated as a single particle executing small amplitude motion, $x_\pm, y_\pm \ll \sigma_{x,y}$. In reality, the individual particles within the bunch do not move in lock-step, and many have large amplitudes. Furthermore, Figure 2.1 reveals that the linear approximation grossly overestimates the kick felt by a particle at $x, y > \sigma$ suggesting that it is necessary to average Equation 2.20 over the particle distributions.

The equations for the centroid motion of the beams are

$$\langle x_{t+1}\rangle_+ - 2\cos 2\pi Q_0\ \langle x_t\rangle_+ + \langle x_{t-1}\rangle_+ = \beta^* \sin 2\pi Q_0\ \langle \Delta x'_t\rangle_+, \tag{2.27a}$$

$$\langle x_{t+1}\rangle_- - 2\cos 2\pi Q_0\ \langle x_t\rangle_- + \langle x_{t-1}\rangle_- = \beta^* \sin 2\pi Q_0\ \langle \Delta x'_t\rangle_-, \tag{2.27b}$$

which are just Equations 2.20 integrated over the beam distributions, where $\langle x\rangle_\pm$ are the coordinates of the centroids and $\langle \Delta x'\rangle_\pm$ is the beam-beam deflection for an individual particle averaged over the distribution. Using the coordinate system illustrated in Figure 2.4, the average beam-beam kick (felt by the positrons) is thus

$$\begin{aligned}\langle \Delta x'\rangle_+ = -\frac{N_- r_e}{\pi\sigma_+^2\gamma_0}\int_{-\infty}^{\infty} dx \int_{-\infty}^{\infty} dy\ e^{-[(x-\delta x)^2+(y-\delta y)^2]/2\sigma_+^2} \\ \times \frac{(1-e^{-(x^2+y^2)/2\sigma_-^2})x}{x^2+y^2},\end{aligned} \tag{2.28}$$

where δx and δy are the horizontal and vertical distances between the centers of electron and positron distributions.

The figure exaggerates δx and δy, which are typically less than $\sigma_\pm$ for each beam. The amplitude of the centroid motion must be very small or else the beams would not stay in collision. Expanding $\langle \Delta x'\rangle_+$ in a Taylor series in δx and δy,

$$\langle \Delta x'\rangle_+ \simeq \delta x \left[\frac{\partial}{\partial \delta x}\langle \Delta x'\rangle_+\right]_{\delta x=0,\ \delta y=0} + \delta y \left[\frac{\partial}{\partial \delta y}\langle \Delta x'\rangle_+\right]_{\delta x=0,\ \delta y=0} + \cdots \tag{2.29}$$

Since δx and δy are parameters in the integrals, the partial derivatives can be calculated then evaluated at $\delta x = 0,\ \delta y = 0$ before doing the integrals over x and y,

$$\left[\frac{\partial}{\partial \delta y}\langle \Delta x'\rangle_+\right]_{\delta x=0,\ \delta y=0} = 0, \tag{2.30}$$

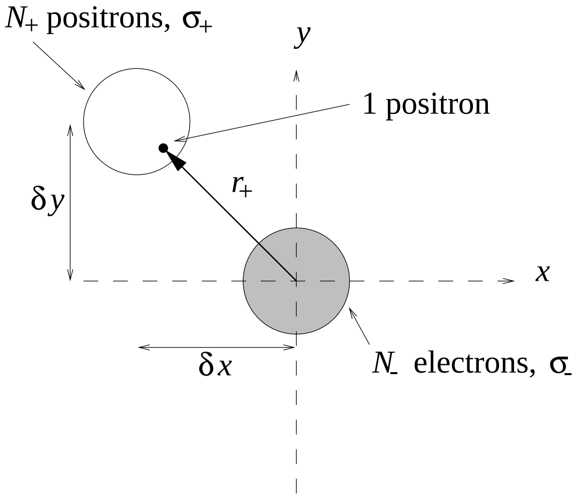

Figure 2.4: Coordinate system used for calculating the beam-beam interaction, $r_+^2 = (x+\delta x)^2 + (y+\delta y)^2$.

$$\begin{aligned}
\left[\frac{\partial}{\partial \delta x}\langle \Delta x' \rangle_+\right]_{\delta x=0,\ \delta y=0} &= -\frac{N_- r_e}{\pi\gamma_0\sigma_+^2}\left[\int_{-\infty}^{\infty} dx \int_{-\infty}^{\infty} dy \frac{\left(1-e^{-\frac{x^2+y^2}{2\sigma_-^2}}\right)}{x^2+y^2} x \right. \\
&\quad \left. \times\ (x-\delta x)\frac{e^{-\frac{(x-\delta x)^2+(y-\delta y)^2}{2\sigma_+^2}}}{\sigma_+^2}\right]_{\delta x=0,\ \delta y=0} \\
&= -\frac{N_- r_e}{\pi\gamma_0\sigma_+^2\sigma_-^2}\int_0^{\infty} dr \int_0^{2\pi} d\theta\ r\cos^2\theta\ \exp\left[-r^2\left(\frac{\sigma_+^2+\sigma_-^2}{2\sigma_+^2\sigma_-^2}\right)\right] \\
&= -\frac{N_- r_e}{\gamma_0(\sigma_+^2+\sigma_-^2)}. \qquad (2.31)
\end{aligned}$$

Thus, $\langle \Delta x' \rangle_+$ is

$$\begin{aligned}
\langle \Delta x' \rangle_+ &= -\frac{N_- r_e}{\gamma_0(\sigma_+^2+\sigma_-^2)}(\langle x\rangle_+ - \langle x\rangle_-) \qquad (2.32a) \\
&= -\frac{4\pi}{\beta^*}\Xi(\langle x\rangle_+ - \langle x\rangle_-), \text{ where} \qquad (2.32b)
\end{aligned}$$

$$\Xi_+ \equiv \frac{N_\mp r_e}{4\pi\gamma_0(\varepsilon_+ + \varepsilon_-)}. \qquad (2.33)$$

with similar expressions for $\langle \Delta x' \rangle_-$ and ξ_-. Substituting this into Equations 2.27 results in coupled equations that are very similar to Equations 2.23 so that they also can be diagonalized by $\Sigma = \langle x^+ \rangle + \langle x^- \rangle$ and $\Pi = \langle x^+ \rangle - \langle x^- \rangle$. The equation for the π mode frequency is therefore the same as Equation 2.25 with $\xi_\pm \to \Xi_\pm$.

$$\cos 2\pi(Q_0 + \Delta Q_\pi) = \cos 2\pi Q_0 - 2\pi \xi_{\mathit{eff}} \sin 2\pi Q_0, \tag{2.34}$$

where $\xi_{\mathit{eff}} \equiv \Xi_+ + \Xi_-$. When the beams are symmetric, $N_+ = N_- = N$ and $\sigma_+ = \sigma_- = \sigma$, $\Xi_\pm = \frac{1}{2}\xi_\pm$, and $\xi_{\mathit{eff}} \Rightarrow \xi$. So for small tune shifts and symmetric beams, Equation 2.34 simplifies to

$$\Delta Q = \lambda \xi_{\mathit{eff}}, \quad \text{with} \quad \lambda = 1. \tag{2.35}$$

This derivation is similar to a more general one done by Hirata[9] that results in the following equations,

$$2 \cos \bar{\mu}_{\sigma,\pi} = \cos \mu_+ + \cos \mu_- - 2\pi \Xi_+ \sin \mu_+ - 2\pi \Xi_- \pm \sqrt{\mathcal{Q}}, \tag{2.36}$$

$$\mathcal{Q} = (\cos \mu_+ - \cos \mu_- - 2\pi \Xi_+ \sin \mu_+ + 2\pi \Xi_- \sin \mu_-)^2 + 16\pi^2 \Xi_+ \Xi_- \sin \mu_+ \sin \mu_-,$$

which reduces to Equation 2.34 when the beams have the same tune and energy.

2.3.4 A More Realistic Model

The previous models both assume at some point that the small amplitude motion description applies to coherent motion; however, since the particles oscillate independently, extracting the coherent part is complicated. Yokoya and Koiso[10], using a linearized Vlasov equation, calculate λ for several beam aspect ratios and fit these points to a polynomial,

$$\frac{\Delta Q_\pi}{\xi_x} = \lambda(r) = 1.330 - 0.370\ r + 0.279\ r^2 \tag{2.37a}$$

$$\frac{\Delta Q_\pi}{\xi_y} = \lambda(1 - r), \tag{2.37b}$$

where $r = \sigma_y^*/(\sigma_x^* + \sigma_y^*)$. Other researchers have independently calculated values that are consistent with this model[11, 12]. For round beams, $r = 0.5$, so

$$\boxed{\lambda = 1.21}. \tag{2.38}$$

Strictly speaking Yokoya and Koiso's values for λ are valid only for $2\pi\xi \ll 1$, but round beams are expected to achieve tune shift parameters of $2\pi\xi \sim 1$. For comparing theory to measured tune shifts at TRISTAN, Koiso *et al.*[13] use the trigonometric expression,

$$\cos 2\pi(Q_0 + \Delta Q_\pi) = \cos 2\pi Q_0 - 2\pi\lambda\xi \sin 2\pi Q_0. \tag{2.39}$$

The question still arises of what to do when $\xi_+ \neq \xi_-$. For equal beam sizes, $\varepsilon_+ = \varepsilon_-$, but unequal tune shift parameters, $\xi_+ \neq \xi_-$, the above mentioned model[10] predicts that

$$\Delta Q_\pi \sim \lambda \xi_{avg}, \quad \text{where here} \quad \xi_{avg} = \frac{1}{2}(\xi_+ + \xi_-), \tag{2.40}$$

is a reasonable approximation provided that the ratio of tune shift parameters is not too large, $\frac{1}{2} < \xi_-/\xi_+ < 2$. This method of averaging the effects of beam asymmetry differs from the method derived in Section 2.3.3 where

$$\xi_{\mathit{eff}} = (\Xi_+ + \Xi_-) \propto \frac{N_+ + N_-}{\varepsilon_+ + \varepsilon_-},$$

instead of

$$\xi_{avg} = \frac{1}{2}(\xi_+ + \xi_-) \propto \frac{N_+}{\varepsilon_+} + \frac{N_-}{\varepsilon_-}.$$

When $\varepsilon_+ \approx \varepsilon_-$, these two "effective" tune shift parameters are approximately the same. A calculation of this sort for the case when both $\xi_+ \neq \xi_-$ and $\varepsilon_+ \neq \varepsilon_-$ has not been done. However, for $\xi_+ \neq \xi_-$ with $\varepsilon_+ = \varepsilon_-$, λ does not vary much and only increases from 1.21 to 1.28 as $\xi_+ : \xi_-$ increases from 1:1 to 2:1.

Chapter 3
Methods for Making Round Beams

The horizontal size of the beam arises from radiation effects[14]. The quantum emission of radiation randomly decreases the energy of particles. This changes the radius of curvature of the particle's orbit so that it passes through the quadrupoles horizontally off-axis, which excites betatron oscillations since the particle receives some extra focusing. The RF cavities replace the average energy lost per turn independently of the horizontal or vertical positions of the particles, which has a net damping effect on the transverse motion. The equilibrium between these two processes determines the horizontal emittance. With no coupling and no vertical bends, quantum emission of radiation does not change the vertical orbit and thus will not excite vertical motion. Due to conservation of momentum, the transverse momentum of the particle does change when it emits a photon, but since the angular spread of the emitted photons is extremely small, $\theta \approx 1/\gamma_0$, this is a negligible effect. Thus, even for "flat" beams, the observed vertical beam size is due primarily to extraneous coupling between horizontal and vertical motion, such as from imperfectly compensated solenoids or misaligned magnets.

3.1 Resonant Coupling

Many papers discuss the effects of weak coupling on beam behavior[15, 16, 17, 18]. This section is an attempt to summarize several of these, with an emphasis on the behavior of the normal modes near the difference resonance, $Q_x - Q_y = n$, where n is an integer.

The one turn, 4×4 transfer matrix for horizontal and vertical motion in an ideal ring (no coupling) is

$$\mathbf{T} = \begin{pmatrix} \mathbf{M}_x & \mathbf{0} \\ \mathbf{0} & \mathbf{M}_y \end{pmatrix}, \tag{3.1}$$

where $M_{x,y}$ are given by Equation 2.18. It is convenient to transform to normalized coordinates[1] so that the one turn matrix becomes a rotation matrix,

$$\begin{aligned} \mathbf{T} &= \begin{pmatrix} \mathbf{G}_x & \mathbf{0} \\ \mathbf{0} & \mathbf{G}_y \end{pmatrix} \begin{pmatrix} \mathbf{M}_x & \mathbf{0} \\ \mathbf{0} & \mathbf{M}_y \end{pmatrix} \begin{pmatrix} \mathbf{G}_x^{-1} & \mathbf{0} \\ \mathbf{0} & \mathbf{G}_y^{-1} \end{pmatrix} \\ &= \begin{pmatrix} \mathbf{R}(\mu_x) & \mathbf{0} \\ \mathbf{0} & \mathbf{R}(\mu_y) \end{pmatrix}, \end{aligned} \tag{3.2}$$

where $\mathbf{G_{x,y}}$ are the transformation matrices,

$$\mathbf{G}_{x,y} = \begin{pmatrix} 1/\sqrt{\beta_{x,y}} & 0 \\ \alpha_{x,y}/\sqrt{\beta_{x,y}} & \sqrt{\beta_{x,y}} \end{pmatrix}. \tag{3.3}$$

In general, however, there will be some amount of coupling, so the one turn matrix is not block diagonal,

$$\mathbf{T} = \begin{pmatrix} \mathbf{M} & \mathbf{m} \\ \mathbf{n} & \mathbf{N} \end{pmatrix}. \tag{3.4}$$

which can be block diagonalized by the transformation

$$\mathbf{U} \equiv \begin{pmatrix} \mathbf{A} & \mathbf{0} \\ \mathbf{0} & \mathbf{B} \end{pmatrix} \tag{3.5a}$$

[1] In unnormalized coordinates, assuming no coupling between horizontal and vertical motion, the turn-by-turn coordinates of a particle at a particular point in the ring trace out an ellipse in x-x' and y-y' phase space (see Figure 1.2). In normalized phase space, the axes are rescaled so that the particle traces out a circle. In either case, the area of phase space occupied by a beam is its emittance, $\varepsilon_{x,y}$.

$$= \mathbf{V}^{-1}\mathbf{T}\mathbf{V}, \tag{3.5b}$$

$$= \begin{pmatrix} \gamma_c\mathbf{I} & -\mathbf{C} \\ \mathbf{C}^\dagger & \gamma_c\mathbf{I} \end{pmatrix} \begin{pmatrix} \mathbf{M} & \mathbf{m} \\ \mathbf{n} & \mathbf{N} \end{pmatrix} \begin{pmatrix} \gamma_c\mathbf{I} & \mathbf{C} \\ -\mathbf{C}^\dagger & \gamma_c\mathbf{I} \end{pmatrix} \tag{3.5c}$$

where the parameters of the transformation matrix $\mathbf{V}$ satisfy $\gamma_c^2 + \det\mathbf{C} = 1$ and $\mathbf{A}$ and $\mathbf{B}$ are rotation matrices for the normal modes. After some matrix manipulation, it is possible to show that

$$\mathbf{C} = \frac{-\mathbf{H}}{\gamma_c \mathrm{Tr}(\mathbf{A}-\mathbf{B})}, \tag{3.6}$$

$$\gamma_c = \sqrt{\frac{1}{2} + \frac{1}{2}\left|\frac{\mathrm{Tr}(\mathbf{M}-\mathbf{N})}{\mathrm{Tr}(\mathbf{A}-\mathbf{B})}\right|}, \tag{3.7}$$

$$\mathbf{A} = \mathbf{M} - \frac{1}{\gamma_c}\mathbf{m}\mathbf{C}^\dagger, \quad \mathbf{B} = \mathbf{N} + \frac{1}{\gamma_c}\mathbf{C}^\dagger\mathbf{n}, \text{ and} \tag{3.8}$$

$$[\mathrm{Tr}(\mathbf{A}-\mathbf{B})]^2 = [\mathrm{Tr}(\mathbf{M}-\mathbf{N})]^2 + 4\det\mathbf{H} \tag{3.9}$$

where the matrix $\mathbf{H}$ is defined as

$$\mathbf{H} \equiv \mathbf{m} + \mathbf{n}^\dagger, \tag{3.10}$$

and the $\dagger$ symbol on a 2×2 matrix represents the transformation

$$\begin{pmatrix} a & b \\ c & d \end{pmatrix}^\dagger = \begin{pmatrix} d & -b \\ -c & a \end{pmatrix} \tag{3.11}$$

The normal mode coordinates, $\mathbf{W}^T = (w, w', v, v')$, are related to $\mathbf{X}$ by

$$\mathbf{W} = \mathbf{V}^{-1}\mathbf{X}, \qquad \mathbf{X} = \mathbf{V}\mathbf{W}, \tag{3.12}$$

so on the nth turn, the particle coordinates in the laboratory frame are

$$\mathbf{X}_n = \mathbf{V}\mathbf{U}^n(\mathbf{V}^{-1}\mathbf{X}_0) = \mathbf{V}\mathbf{U}^n\mathbf{W}_0. \tag{3.13}$$

If only mode A is excited, then $\mathbf{W}^T = (\sqrt{\varepsilon_A}\cos\phi_0^A, \sqrt{\varepsilon_A}\sin\phi_0^A, 0, 0)$, and n turns later

$$x/\sqrt{\beta_A} = \sqrt{\varepsilon_A}\gamma_c\cos(n\mu_A - \phi_0^A), \tag{3.14a}$$

$$y/\sqrt{\beta_B} = -\sqrt{\varepsilon_A}\left[C_{22}\cos(n\mu_A - \phi_0^A) + C_{12}\sin(n\mu_A - \phi_0^A)\right], \tag{3.14b}$$

where $\mu_A \equiv 2\pi Q_A$ and Q_A is the tune of mode A. Similarly if mode B is excited, $\mathbf{W}^T = (0, 0, \sqrt{\varepsilon_B}\cos\phi_0^B, \sqrt{\varepsilon_B}\sin\phi_0^B)$, and

$$x/\sqrt{\beta_B} = \sqrt{\varepsilon_B}\left[C_{11}\cos(n\mu_B - \phi_0^B) - C_{12}\sin(n\mu_B - \phi_0^B)\right], \tag{3.15a}$$

$$y/\sqrt{\beta_B} = \sqrt{\varepsilon_B}\gamma_c\cos(n\mu_B - \phi_0^B). \tag{3.15b}$$

If the coupling is weak, then the components of $\mathbf{C}$ are small. Consequently, mode A is nearly horizontal, and mode B is nearly vertical. Figure 3.1 illustrates two special cases. If $C_{12} = 0$ at a particular location in the storage ring, the modes at that location are linear oscillations, just like the ideal horizontal and vertical motion, except that the normal mode axes are rotated from the x and y axes but not necessarily by the same angle,

$$\theta_A = \tan^{-1}\left(\frac{C_{22}}{\gamma_c}\sqrt{\frac{\beta_B}{\beta_A}}\right), \tag{3.16a}$$

$$\theta_B = \tan^{-1}\left(\frac{C_{11}}{\gamma_c}\sqrt{\frac{\beta_A}{\beta_B}}\right), \tag{3.16b}$$

as shown in the figure. If $C_{11} = C_{22} = 0$, then the modes are ellipses with axes parallel to the x and y axes, and the lengths of the axes of the mode ellipses are

$$x^A_{\max} = \sqrt{\varepsilon_A\beta_A}\gamma_c, \quad y^A_{\max} = \sqrt{\varepsilon_A\beta_B}|C_{12}|, \tag{3.17a}$$

$$y^B_{\max} = \sqrt{\varepsilon_B\beta_B}\gamma_c, \quad x^B_{\max} = \sqrt{\varepsilon_B\beta_A}|C_{12}|. \tag{3.17b}$$

In general, because $\mathbf{C}$ is a function of azimuthal position, the orientation of the modes tends to vary between these two cases as a function of position.

Up to this point, the effects of variations in particle energy have been ignored, but the trajectory a particle that has a slightly lower/higher energy than the design energy will have a smaller/larger radius of curvature. The average position about which an off-energy particle oscillates is

$$x = \eta_x\,\delta, \quad \delta \equiv \frac{\Delta E}{E}, \tag{3.18}$$

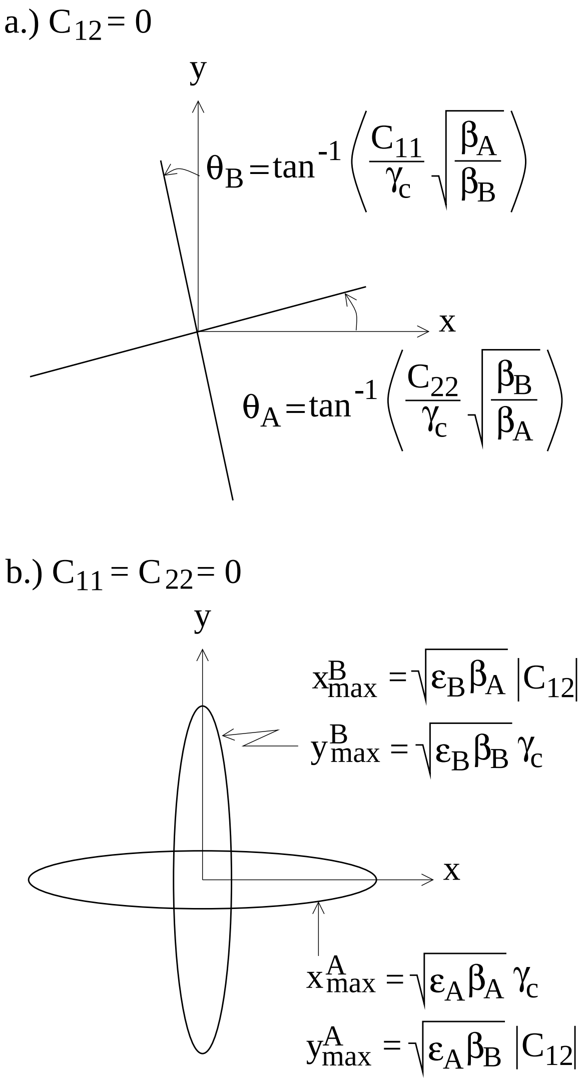

Figure 3.1: The coupled single beam modes for two special cases: a.) $C_{12} = 0$, b.) $C_{11} = C_{22} = 0$.

where η_x is called the horizontal dispersion. Like the β-function, dispersion varies with position, and because the beam has a finite energy spread, σ_E, it contributes to the horizontal beam size, $\sigma^2 = \beta\varepsilon + \eta_x^2\delta^2$, so storage rings are usually designed to have zero dispersion at collision points to minimize σ^*. With no coupling, variations in energy affect only horizontal motion, so the vertical dispersion is automatically zero. But in addition to mixing the horizontal and vertical motion, coupling can also introduce vertical dispersion,

$$(\eta_x, \eta_x', \eta_y, \eta_y')^T = \mathbf{V}(\eta_A, \eta_A', \eta_B, \eta_B')^T, \tag{3.19}$$

if the couplers are located in regions with $\eta_x \neq 0$ for the ideal lattice. Thus, transverse coupling can blow up the beam vertically in two ways. First, wherever $C_{12} \neq 0$, mode A is a nearly horizontal ellipse in x-y space, and so has a vertical component. Second, even though mode B is mostly vertical, ε_B can be excited by quantum emission of radiation wherever $\eta_y \neq 0$ and also wherever the mode has a horizontal component and $\eta_x \neq 0$.

3.1.1 The Coupling Resonance

The difference resonance, $Q_x - Q_y = n$, is also called the coupling resonance. Recall that Equation 3.9 gave the relationship between Q_x, Q_y, Q_A, Q_B, and the matrix $\mathbf{H}$,

$$[\mathrm{Tr}(\mathbf{A} - \mathbf{B})]^2 = [\mathrm{Tr}(\mathbf{M} - \mathbf{N})]^2 + 4 \det \mathbf{H},$$

and from Equation 3.8,

$$\mathbf{A} = \mathbf{M} - \frac{1}{\gamma_c}\mathbf{m}\mathbf{C}^\dagger, \quad \mathbf{B} = \mathbf{N} + \frac{1}{\gamma_c}\mathbf{C}^\dagger\mathbf{n}.$$

For weak coupling, the effects of known couplers at various longitudinal positions can be "projected" to a particular longitudinal position[19], and the full turn matrix can then be written in a particularly simple form,

$$\mathbf{T}(s) = \begin{pmatrix} \mathbf{R}_x & \mathbf{0} \\ \mathbf{0} & \mathbf{R}_y \end{pmatrix} \begin{pmatrix} \mathbf{I} & \mathbf{F} \\ -\mathbf{F}^\dagger & \mathbf{I} \end{pmatrix} = \begin{pmatrix} \mathbf{R}_x & \mathbf{R}_x\mathbf{F} \\ -\mathbf{R}_y\mathbf{F}^\dagger & \mathbf{R}_y \end{pmatrix}, \tag{3.20}$$

where $\mathbf{F}$ is a sum of projection matrices[2], so $\mathrm{Tr}(\mathbf{M}-\mathbf{N}) = 2(\cos 2\pi Q_x - \cos 2\pi Q_y)$. Comparing Equations 3.9 and 3.8, we see that as Q_x approaches Q_y, the observed tunes, Q_A and Q_B, also approach each other, but their approach is limited to a minimum tune difference,

$$\cos 2\pi Q_A - \cos 2\pi Q_B = \sqrt{\det \mathbf{H}}. \tag{3.21}$$

Also, γ_c approaches $1/\sqrt{2}$ as the tunes approach the coupling resonance.

The matrix $\mathbf{H}$ can be split into two pieces, one sensitive to the difference resonance and the other sensitive to the (unstable) sum resonance,

$$\mathbf{H} = \mathbf{H}_+ \sin \pi(Q_x + Q_y) + \mathbf{H}_- \sin \pi(Q_x - Q_y). \tag{3.22}$$

So when $Q_x = Q_y$, the matrix $\mathbf{C}$ can be written as

$$\mathbf{C} = \frac{\mp \mathbf{H}_+}{2\gamma_c \sqrt{\det \mathbf{H}_+}}, \tag{3.23}$$

where the negative sign corresponds to $\mathrm{Tr}(\mathbf{A} - \mathbf{B}) > 0$. $\mathbf{H}_+$ at an arbitrary point in the ring (using only skew quadrupoles as couplers) is[18]

$$\mathbf{H}_+ = \sum_m q_m \; \mathbf{R}^\dagger[\pi(Q_x - Q_y)] \; \mathbf{R}[\overline{\phi_x(s_p) - \phi_x(s_m)} - \overline{\phi_y(s_p) - \phi_y(s_m)}], \tag{3.24}$$

where $q = \sqrt{\beta_x \beta_y}/f$ is the normalized skew quadrupole strength, $\phi(s)$ is the betatron phase advance from the IP to s, and $\overline{\phi(s_p) - \phi(s_m)}$ indicates the phase difference is modulo $2\pi Q$.

[2]The projection matrix approach is discussed in more detail in Appendix A and in the references.[17, 18, 19]

3.1.2 Exciting the Coupling Resonance in CESR

A number of skew quadrupoles exist in CESR that are normally used for compensating unwanted coupling. Each skew quadrupole is powered independently, and they are located in pairs that are symmetric with respect to the IP. Because of this symmetric placement, if the phase advance from the IP to one skew quad is $\phi_{x,y}$, the phase advance to its partner is $2\pi Q_{x,y} - \phi_{x,y}$, so for a pair of skew quadrupoles, $\mathbf{H}_+$ at the IP is

$$\begin{aligned}\mathbf{H}_+ =& q_1\ \mathbf{R}^\dagger[\pi(Q_x - Q_y)]\ \mathbf{R}[\phi_x - \phi_y] + \\ & q_2\ \mathbf{R}^\dagger[\pi(Q_x - Q_y)]\ \mathbf{R}[(2\pi Q_x - \phi_x) - (2\pi Q_y - \phi_y)].\end{aligned} \tag{3.25}$$

On the coupling resonance, $Q_x = Q_y$, and so for $q_1 = q_2 - q$, $\mathbf{H}_+$ becomes

$$\mathbf{H}_+ = 2q\cos(\phi_y - \phi_x)\ \mathbf{I}. \tag{3.26}$$

Since $(H_+)_{12} = 0$, the normal modes at the IP resemble the first case illustrated in Figure 3.1. From Equation 3.7, $\gamma_c = 1/\sqrt{2}$ on the coupling resonance, so the tilt angles of the modes are

$$\theta_A = \tan^{-1}\left(\sqrt{\frac{\beta_B}{\beta_A}}\right), \tag{3.27a}$$

$$\theta_B = \tan^{-1}\left(\sqrt{\frac{\beta_A}{\beta_B}}\right), \tag{3.27b}$$

and the amplitudes are

$$\mathcal{A}_A = \sqrt{\varepsilon_A(\gamma_c^2 + C_{22}^2)} = \sqrt{\varepsilon_A}, \tag{3.28a}$$

$$\mathcal{A}_B = \sqrt{\varepsilon_B(\gamma_c^2 + C_{11}^2)} = \sqrt{\varepsilon_B}. \tag{3.28b}$$

When $\beta_A = \beta_B$, $\theta_A = \theta_B = \pi/4$. Elsewhere the modes will generally be tilted ellipses, with the tilt angle and aspect ratio varying from point to point around the ring, and also depending on q. Thus, the degree to which the B-mode emittance is excited depends on q, so with strong enough skew quadrupoles, $\varepsilon_B = \varepsilon_A$ is possible.

3.2 The Möbius Twisted Storage Ring

In an ideal ordinary storage ring, the horizontal and vertical motion is independent, so one could visualize a storage ring as a circular strip of paper with the horizontal motion plotted on one side and the vertical motion on the other. Motion in a storage ring with a Möbius twist can be visualized as this same strip of paper being cut, twisted by 180°, and rejoined so that $x \to y$ and $y \to -x$ (or $y \to x$) on every turn, thus the name "Möbius."

3.2.1 Stability

The one turn transfer matrix of the original lattice at the location where the twist occurs can be written as a 4×4 matrix partitioned into 2×2 matrices,

$$\mathbf{M}_0 = \begin{pmatrix} \mathbf{M}_x & \mathbf{0} \\ \mathbf{0} & \mathbf{M}_y \end{pmatrix}, \tag{3.29}$$

where $\mathbf{M}_x$ and $\mathbf{M}_y$ are given by Equation 2.18. For now assuming that the twist section has zero length, the twist can be represented as

$$\mathbf{R} = \begin{pmatrix} \mathbf{0} & -\mathbf{I} \\ \mathbf{I} & \mathbf{0} \end{pmatrix}, \tag{3.30}$$

so the one turn matrix for the Möbius twisted lattice is

$$\mathbf{M} = \mathbf{R}\ \mathbf{M}_0 = \begin{pmatrix} \mathbf{0} & -\mathbf{M}_y \\ \mathbf{M}_x & \mathbf{0} \end{pmatrix}. \tag{3.31}$$

The eigenvalues of $\mathbf{M}$ form reciprocal pairs, λ and $1/\lambda$[5].[3] Their sum, $\Lambda = \lambda + 1/\lambda$, provides the normal mode tunes of the Möbius twisted lattice,

$$Q_{\pm} = \frac{1}{2\pi} \cos^{-1} \frac{\pm\sqrt{\mathcal{E}}}{2}, \tag{3.32}$$

where $\mathcal{E}$ is defined as

$$\mathcal{E} \equiv \det |\mathbf{E}|, \quad \mathbf{E} \equiv \mathbf{M}_x - \mathbf{M}_y^{-1}. \tag{3.33}$$

[3] λ in this context is not the derating factor.

Two consequences are immediately apparent. First, the motion will be stable in the Möbius twisted lattice if $0 \le \mathcal{E} \le 4$. Second, the observed tunes, $Q_{\pm}$, are no longer independently adjustable, and because the cosine function is antisymmetric about $\pi/2$, $Q_{\pm}$ are symmetrically located above and below 0.25.

In terms of the β-functions and related parameters for the untwisted lattice, $\alpha \equiv -\frac{1}{2}\frac{d\beta}{ds}$ and $\beta\,\gamma \equiv 1+\alpha^2$, $\mathcal{E}$ is given by

$$\mathcal{E} = 2 - \{2\cos(\mu_x+\mu_y) - S_x S_y[-2 - 2\alpha_x\alpha_y + \frac{\beta_x}{\beta_y}(1+\alpha_y^2) + \frac{\beta_y}{\beta_x}(1+\alpha_x^2)]\} \quad (3.34)$$

Defining a coefficient, R, for the general case of $\beta_x \neq \beta_y$ and $\alpha_x \neq \alpha_y$ at the ends of the Möbius insert,

$$R = \left(\sqrt{\frac{\beta_x}{\beta_y}} - \sqrt{\frac{\beta_y}{\beta_x}}\right)^2 + \left(\sqrt{\frac{\beta_x}{\beta_y}}\alpha_y - \sqrt{\frac{\beta_y}{\beta_x}}\alpha_x\right)^2, \quad (3.35)$$

the stability requirement becomes

$$0 \le 2(1-\cos(\mu_x+\mu_y)) + R S_x S_y \le 4. \quad (3.36)$$

If the twist occurs at a "waist" in the untwisted lattice such that the β-functions and their slopes are matched, $\beta_x = \beta_y$ and $\alpha_x = \alpha_y = 0$, then $R = 0$, and the stability condition becomes $-1 \le \cos(\mu_x+\mu_y) \le 1$. Thus, if the motion is stable in the untwisted lattice (μ_x and μ_y are real), then the motion will also be stable in the Möbius twisted lattice. However, in the real world some mismatch is inevitable. Figure 3.2 shows the regions of stability for the Möbius lattice for a gross mismatch, $\alpha_x = \alpha_y = 0$, and $\beta_x = 1$ meter, $\beta_y = 2$ meters[1]. Although this is a much worse mismatch than one might reasonably expect, areas of instability exclude only a modest region of tune space.

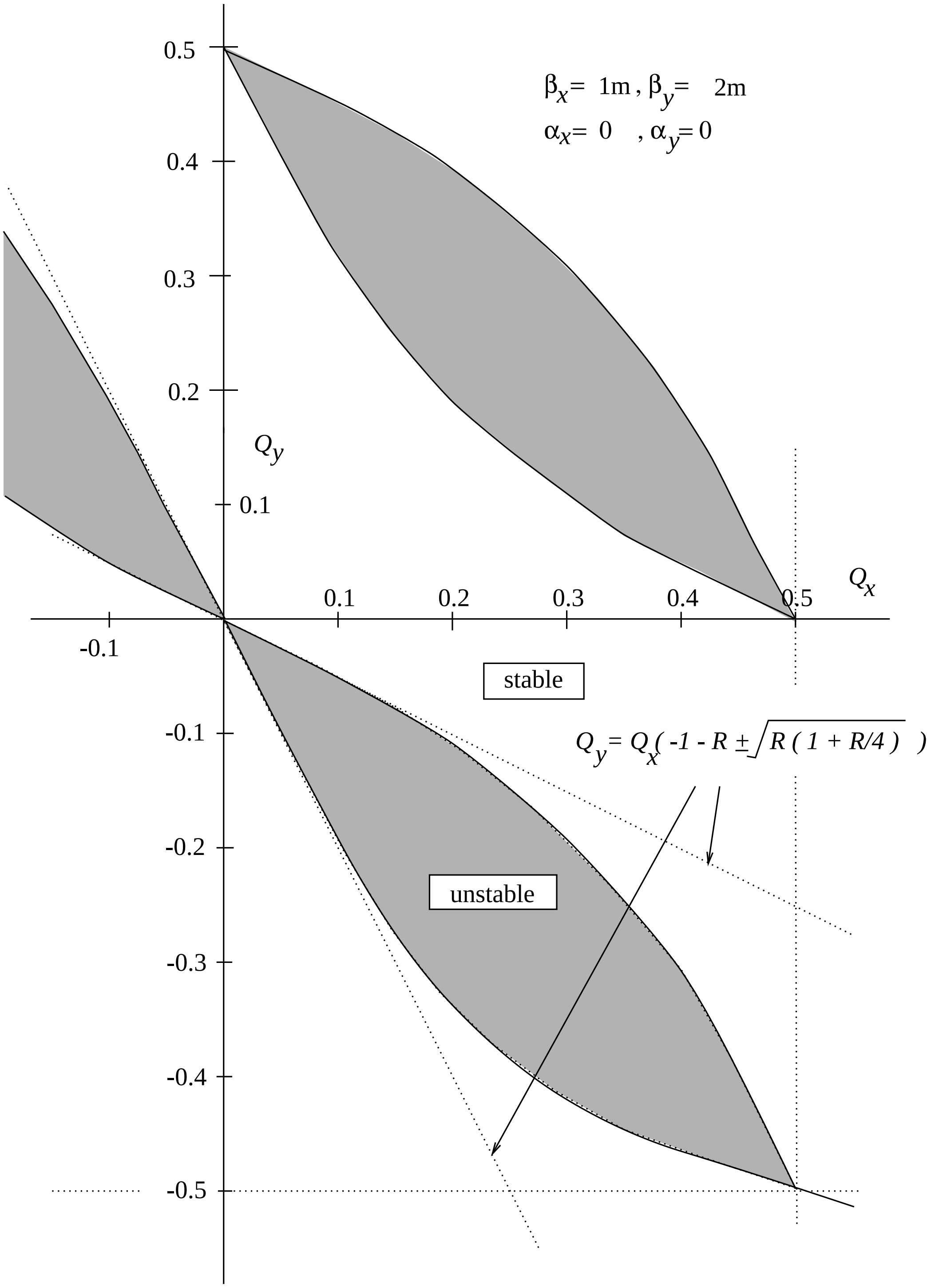

Figure 3.2: Stable and unstable regions of the Q_x-Q_y tune plane for a lattice with a mismatched Möbius insert[1]; $\beta_x = 1$ meter, $\beta_y = 2$ meters, and $\alpha_x = \alpha_y = 0$ at the match point.

3.2.2 Design of a Möbius Insert

The transformation $(x, x', y, y') \rightarrow (y, y', x, x')$ implies a particular phase advance through the Möbius twist insert; however, it is only necessary to transform an orbit lying in the horizontal plane just before entry to exit with displacement and angle lying in the vertical plane and vice versa, $(x, x', y, y') \rightarrow (ay + by', cy + dy', ex + fx', gx + hx')$. Thus, the goal is a transfer line that is block off-diagonal like Equation 3.30, but not necessarily with $\pm\mathbf{I}$ for the off-diagonal blocks.

The transfer matrix for a line consisting of nothing but drift sections and normal quadrupoles is

$$\mathbf{M} = \begin{pmatrix} \mathbf{A} & \mathbf{0} \\ \mathbf{0} & \mathbf{D} \end{pmatrix}, \tag{3.37}$$

where $\mathbf{A}$ and $\mathbf{D}$ are 2×2 matrices. Azimuthal rotation of either the transverse coordinate system or the line itself by angle ϕ can be represented by

$$\mathbf{M}(\phi) = \mathbf{R}(\phi)\ \mathbf{M}\ \mathbf{R}(-\phi) = \begin{pmatrix} c^2\mathbf{A} + s^2\mathbf{D} & cs(-\mathbf{A} + \mathbf{D}) \\ cs(-\mathbf{A} + \mathbf{D}) & s^2\mathbf{A} + c^2\mathbf{D} \end{pmatrix}, \tag{3.38}$$

where $c = \cos\phi$, $s = \sin\phi$, and

$$\mathbf{R}(\phi) = \begin{pmatrix} c\mathbf{I} & s\mathbf{I} \\ -s\mathbf{I} & c\mathbf{I} \end{pmatrix}. \tag{3.39}$$

$\mathbf{M}(\phi)$ can be made block off-diagonal if and only if $\mathbf{A} = -\mathbf{D}$ and $c^2 = s^2 = 1/2$. The latter is true for $\phi = \pm\pi/4$. In that case the transfer matrix of the insert after rotation about its axis by $\pm\pi/4$ is

$$\mathbf{M}(\pm\pi/4) = \begin{pmatrix} \mathbf{0} & \mathbf{D} \\ \mathbf{D} & \mathbf{0} \end{pmatrix}. \tag{3.40}$$

The transfer matrix for the configuration of quadrupoles and drift spaces illus-

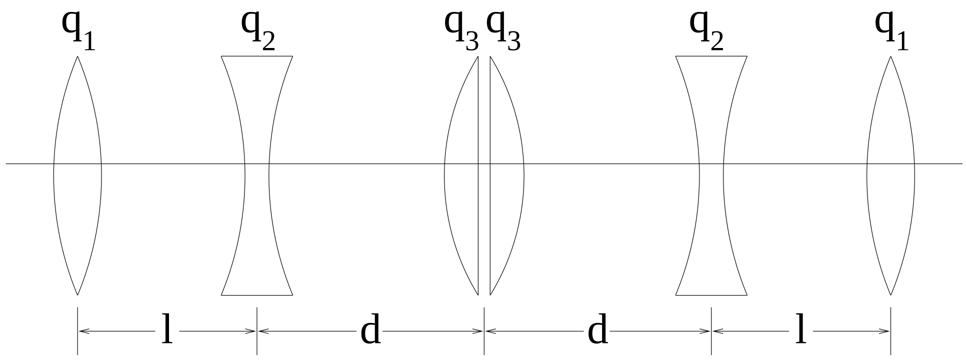

Figure 3.3: An arrangement of focusing and defocusing quadrupoles that can become a Möbius insert. Quadrupoles q_1 and q_3 are assumed to be focusing in the horizontal plane, while q_2 is assumed to be defocusing in the horizontal plane. The two quadrupoles labeled q_3 are drawn as half lenses in order to place them with no space between them, as if for instance they were a single quadrupole. In general, there could be some space between these, as is actually the case for the Möbius quadrupoles in CESR.

trated in Figure 3.3 can be designed to have the form[20, 21]

$$\mathbf{M} = \begin{pmatrix} -1 & -\mathcal{L} & 0 & 0 \\ 0 & -1 & 0 & 0 \\ 0 & 0 & 1 & \mathcal{L} \\ 0 & 0 & 0 & 1 \end{pmatrix}, \tag{3.41}$$

where $\mathcal{L}$ has the dimension of length and is left undetermined initially. Since this has the form $\mathbf{A} = -\mathbf{D}$, it can also serve as a Möbius insert. The transfer matrix from the end of the insert to the center of the insert can be written as

$$\mathbf{M}_{3\leftarrow 1} = \begin{pmatrix} X_x & X_f & 0 & 0 \\ F_x & F_f & 0 & 0 \\ 0 & 0 & Y_y & Y_g \\ 0 & 0 & G_y & G_g \end{pmatrix}, \tag{3.42}$$

and because the insert is made up of only quadrupoles and drifts, the transfer matrix from the center to the end is

$$\mathbf{M}_{1\leftarrow 3} = \begin{pmatrix} F_f & X_f & 0 & 0 \\ F_x & X_x & 0 & 0 \\ 0 & 0 & G_g & Y_g \\ 0 & 0 & G_y & Y_y \end{pmatrix}. \tag{3.43}$$

The transfer matrix for the whole configuration is therefore

$$\begin{aligned} \mathbf{M} &= \mathbf{M}_{1\leftarrow 3}\mathbf{M}_{3\leftarrow 1}, \\ &= \begin{pmatrix} X_xF_f + X_fF_x & 2X_fF_f & 0 & 0 \\ 2X_xF_x & X_xF_f + X_fF_x & 0 & 0 \\ 0 & 0 & Y_yG_g + Y_gG_y & 2Y_gG_g \\ 0 & 0 & 2Y_yG_y & Y_yG_g + Y_gG_y \end{pmatrix}. \end{aligned} \tag{3.44}$$

For this matrix to have the same form as Equation 3.41,

$$-1 = X_xF_f + X_fF_x, \tag{3.45a}$$

$$0 = X_xF_x, \tag{3.45b}$$

$$1 = Y_yG_g + Y_gG_y, \tag{3.45c}$$

$$0 = Y_yG_y, \tag{3.45d}$$

$$0 = X_fF_f + Y_gG_g. \tag{3.45e}$$

In addition, transfer matrices have the property that their determinants are equal to one, so

$$1 = X_xF_f - X_fF_x, \tag{3.46a}$$

$$1 = Y_yG_g - Y_gG_y. \tag{3.46b}$$

From Equation 3.45b, either $X_x = 0$ or $F_x = 0$, but Equation 3.45a and Equation 3.46a are both true only if $X_x = 0$. Similarly, Equations 3.45c, 3.45d, and 3.46b agree if $G_y = 0$. ($F_x = 0$ and $Y_y = 0$ will satisfy the equations if the overall sign of $\mathbf{M}_E$ is reversed.) So the minimum number of constraints that must be satisfied are

$$0 = X_x, \tag{3.47a}$$

$$0 = G_y, \tag{3.47b}$$

$$0 = X_f F_f + Y_g G_g. \tag{3.47c}$$

Assuming that the quadrupoles can be approximated by thin lenses, Equations 3.47 in terms of l, d, and the quadrupole strengths, q_1, q_2, and q_3, are

$$0 = 1 - (l + d)q_1 - dq_2 + ldq_1q_2, \tag{3.48a}$$

$$0 = q_1 + q_2 + q_3 + lq_1q_2 + (l + d)q_1q_3 + dq_2q_3 + ldq_1q_2q_3, \tag{3.48b}$$

$$0 = l + d + l^2dq_2^2 + 2(l + d)ldq_2q_3. \tag{3.48c}$$

Because there are three equations and five unknowns, there is not a unique solution to this system of equations. Additional constraints on l, d, q_1, q_2, and q_3 arise from hardware limitations and from the necessity to fit this line into the rest of the storage ring.

3.2.3 Matching a Möbius Insert to CESR

In theory it is not necessary to design a Möbius twisted lattice that also works with the Möbius insert erect. However, in practice the easiest path is to first commission a normal lattice with an insert that satisfies the constraints in Equation 3.47, then rotate the quadrupoles in the insert about their axes by $\pi/4$. Furthermore, this simplifies the process of simulating and predicting the behavior of such a lattice. Making such an insert requires matching the β-functions and their slopes at the junctions between the insert and the rest of the lattice such that $\beta_x = \beta_y$ and $\alpha_x = \alpha_y$.

For the purposes of matching, the Möbius insert can include additional drift space outside the quadrupoles. In the following formulas, the entrance and exit points of the insert are designated by subscripts J and J' respectively. Because of the symmetry of CESR, $\beta_J = \beta_{J'}$ and $\alpha_{J'} = -\alpha_J$. At J and J', $\beta_x = \beta_y$ and $\alpha_x = \alpha_y$ is assumed, as is necessary for the Möbius insert to match the rest of the ring whether erect or rotated. With these assumptions the transfer matrix for the entire erect insert is

$$\mathbf{M}^E_{J' \leftarrow J} = \begin{pmatrix} C_x + \alpha_J S_x & \beta_J S_x & 0 & 0 \\ \frac{-(1-\alpha_J^2)S_x + 2\alpha_J C_x}{\beta_J} & C_x + \alpha_J S_x & 0 & 0 \\ 0 & 0 & C_y + \alpha_J S_y & \beta_J S_y \\ 0 & 0 & \frac{-(1-\alpha^2)S_y + 2\alpha C_y}{\beta_j} & C_y + \alpha_J S_y \end{pmatrix}, \tag{3.49}$$

where $C_{x,y} = \cos\psi_{x,y}$, $S_{x,y} = \sin\psi_{x,y}$, $\beta = \beta_J$, and $\alpha = \alpha_J$. The transfer matrix after the quadrupoles have been rotated by $\pi/4$ is

$$\mathbf{M}^R_{J' \leftarrow J} = \frac{1}{2} \begin{pmatrix} \mathbf{T}_x + \mathbf{T}_y & -\mathbf{T}_x + \mathbf{T}_y \\ -\mathbf{T}_x + \mathbf{T}_y & \mathbf{T}_x + \mathbf{T}_y \end{pmatrix} \tag{3.50}$$

where $\mathbf{T}_{x,y} = (\beta_J, -\alpha_J; \beta_J, \alpha_J; \psi_{x,y})$ and $\mathbf{T}(\beta_2, \alpha_2; \beta_1, \alpha_1; \phi)$ is the general transfer matrix between two points,

$$\mathbf{T}(\beta_2, \alpha_2; \beta_1, \alpha_1; \phi) = \begin{pmatrix} \sqrt{\frac{\beta_2}{\beta_1}}(C + \alpha_1 S) & \sqrt{\beta_1\beta_2}S \\ \frac{-(1+\alpha_1\alpha_2)S + (\alpha_1 - \alpha_2)C}{\sqrt{\beta_1\beta_2}} & \sqrt{\frac{\beta_1}{\beta_2}}(C - \alpha_2 S) \end{pmatrix}. \tag{3.51}$$

$C = \cos\phi$ and $S = \sin\phi$. In order for this matrix to have the form $\mathbf{A} = -\mathbf{D}$, $\cos\psi_x = -\cos\psi_y$ and $\sin\psi_x = -\sin\psi_y$, which is true for

$$\psi_x = \psi_y \pm \pi. \tag{3.52}$$

Choosing $\psi_y = \psi$ and $\psi_x = \psi + \pi$ (since $Q_x > Q_y$ in CESR), $\mathbf{M}^R_{J'\leftarrow J}$ becomes

$$\mathbf{M}^R_{J'\leftarrow J} = \begin{pmatrix} \mathbf{0} & \mathbf{T}(\beta_J, -\alpha_J; \beta_J, \alpha_J; \psi) \\ \mathbf{T}(\beta_J, -\alpha_J; \beta_J, \alpha_J; \psi) & \mathbf{0} \end{pmatrix}. \tag{3.53}$$

Thus, to summarize, when designing a Möbius lattice, assuming that it is centered on a symmetry point, there are three constraints on the β-functions and their slopes at the junction of the insert and the phase advances across the insert:

$$\boxed{\begin{aligned} \beta_{x,J} = \beta_{y,J} = \beta_J, \\ \alpha_{x,J} = \alpha_{y,J} = \alpha_J, \\ \psi_x = \psi_y \pm \pi = \psi \pm \pi. \end{aligned}} \tag{3.54}$$

The specific values of β_J, α_J, and ψ will be determined by the physical layout of the storage ring and limits on the strengths of the quadrupoles, particularly those in the insert.

When the Möbius quadrupoles are erect, the tunes of the lattice are

$$\tilde{\mu}_y = \mu_y^{arc} + \psi \tag{3.55}$$

$$\tilde{\mu}_x = \mu_x^{arc} + \psi + \pi \tag{3.56}$$

where $\mu_{x,y}^{arc}$ are the betatron phase advances from J' to J through the SIP. Assuming that there is no other coupling in the lattice outside the Möbius insert, the one turn transfer matrix at the SIP is simply

$$\mathbf{M}_{\text{SIP}} = \begin{pmatrix} \mathbf{T}(\beta^*, 0; \beta^*, 0; \tilde{\mu}_x) & \mathbf{0} \\ \mathbf{0} & \mathbf{T}(\beta^*, 0; \beta^*, 0; \tilde{\mu}_y) \end{pmatrix}. \tag{3.57}$$

When the Möbius quadrupoles are rolled, the one turn matrix at the SIP becomes

$$\begin{aligned} \mathbf{M}^R_{\text{SIP}} &= \mathbf{M}_{S\leftarrow J'} \mathbf{M}^R_{J'\leftarrow J} \mathbf{M}_{J\leftarrow S} \\ &= \begin{pmatrix} \mathbf{T}(\beta^*, 0; \beta_J, -\alpha_J; \frac{\mu_x^{arc}}{2}) & \mathbf{0} \\ \mathbf{0} & \mathbf{T}(\beta^*, 0; \beta_J, -\alpha_J; \frac{\mu_y^{arc}}{2}) \end{pmatrix} \end{aligned}$$

$$\times \begin{pmatrix} \mathbf{0} & \mathbf{T}(\beta_J, \alpha_J; \beta_J, -\alpha_J; \psi) \\ \mathbf{T}(\beta_J, \alpha_J; \beta_J, -\alpha_J; \psi) & \mathbf{0} \end{pmatrix}$$
$$\times \begin{pmatrix} \mathbf{T}(\beta_J, \alpha_J; \beta^*, 0; \frac{\mu_x^{arc}}{2}) & \mathbf{0} \\ \mathbf{0} & \mathbf{T}(\beta_J, \alpha_J; \beta^*, 0; \frac{\mu_y^{arc}}{2}) \end{pmatrix}$$
$$= \begin{pmatrix} \mathbf{0} & \mathbf{T}(\beta^*, 0; \beta^*, 0; \bar{\mu} - \frac{\pi}{2}) \\ \mathbf{T}(\beta^*, 0; \beta^*, 0; \bar{\mu} - \frac{\pi}{2}) & \mathbf{0} \end{pmatrix}, \tag{3.58}$$

where $\bar{\mu}$ is the average of the uncoupled tunes,

$$\begin{aligned} \bar{\mu} &= \frac{\tilde{\mu}_x + \tilde{\mu}_y}{2} \\ &= \frac{\mu_x^{arc} + \mu_y^{arc}}{2} + \psi + \frac{\pi}{2}. \end{aligned} \tag{3.59}$$

Recall that the eigen-tunes of the Möbius lattice given by Equation 3.32 are

$$Q_{\pm} = \frac{1}{2\pi} \cos^{-1} \frac{\pm\sqrt{\mathcal{E}}}{2}.$$

From Equation 3.58 $\mathcal{E} = \det \left[\mathbf{T}(\beta^*, 0; \beta^*, 0; \bar{\mu} - \frac{\pi}{2}) + \mathbf{T}^{-1}(\beta^*, 0; \beta^*, 0; \bar{\mu} - \frac{\pi}{2})\right]$, so

$$Q_{\pm} = \frac{1}{2\pi} \cos^{-1} \left[\pm \cos\left(\bar{\mu} - \frac{\pi}{2}\right)\right] \tag{3.60}$$

where the convention $(Q_+ + Q_-)/2 = \overline{Q}$ has been chosen.

Chapter 4
Additional Constraints for CESR Lattices

4.1 Introduction

The configuration of magnet strengths and relative positions is commonly called a "lattice." Not all combinations are viable due to constraints that are independent of whether one is designing a round beam or a flat beam lattice. The three most prominent considerations are solenoid compensation, optimization of injection, and separation at unwanted collision points, and these will be discussed in this chapter.

4.2 Solenoid Compensation

During flat beam operation, extraneous sources of transverse coupling can produce undesirable effects which degrade luminosity, and the CLEO solenoid is the strongest potential source of this coupling. For instance, the width of the beam can be coupled to the height leading to an increase in the beam height at the IP which reduces beam density at the IP; this is of great concern during flat beam operation since the vertical beam size is much smaller than the horizontal beam size, so small increases can have a large effect on luminosity. Second, coupling can introduce vertical dispersion at the IP leading to an increase in the beam height due to the momentum spread of the beam and to misalignment if the beams have different average energies at the IP. Third, horizontal displacement of the beam in the arcs can contribute to vertical displacement at the IP resulting in non-head-on collision; this is a potential problem whether the beams are round or flat. Traditionally, the three pairs of "anti-symmetric" skew quadrupole components needed to compensate the CLEO solenoid have been introduced by rotating the pair of rare earth quadrupoles and the two pairs of iron core quadrupoles nearest the IP.[1] In the following the requirements for solenoid compensation are summarized. A more complete discussion can be found in Appendix A and in the references[19, 22].

In this discussion, it is assumed that the only source of coupling to be compensated is the CLEO solenoid, and that outside the interaction region (the arcs), the transfer matrices are block diagonal. Figure 4.1 provides an illustration of the notation used to distinguish various IR transfer matrices. To avoid the problems mentioned in the previous paragraph, the following requirements must be met:

1. In order for horizontal and vertical motion to be uncoupled outside the interaction region, the full turn transfer matrix must be block diagonal. If there are no coupling elements outside the IR, then the transfer matrix through the IR, $\mathbf{M}^{\mathrm{IR}}$, must be made block diagonal,

$$\mathbf{M}^{\mathrm{IR}} = \begin{pmatrix} \mathbf{A}^{\mathrm{IR}} & \mathbf{0} \\ \mathbf{0} & \mathbf{D}^{\mathrm{IR}} \end{pmatrix}. \tag{4.1}$$

2. To prevent horizontal displacements or angles from being transported to the interaction point as vertical displacements, the first two elements of the third

[1] Quadrupoles rotated about their axes by an arbitrary angle ϕ can be represented by the superposition of a normal quadrupole and a skew quadrupole. The term "anti-symmetric" means that the quadrupoles on the west side of the IP are rotated by angles equal and opposite to those on the east side, which is equivalent to skew quadrupoles on either side of the IP having equal absolute strengths but opposite polarities.

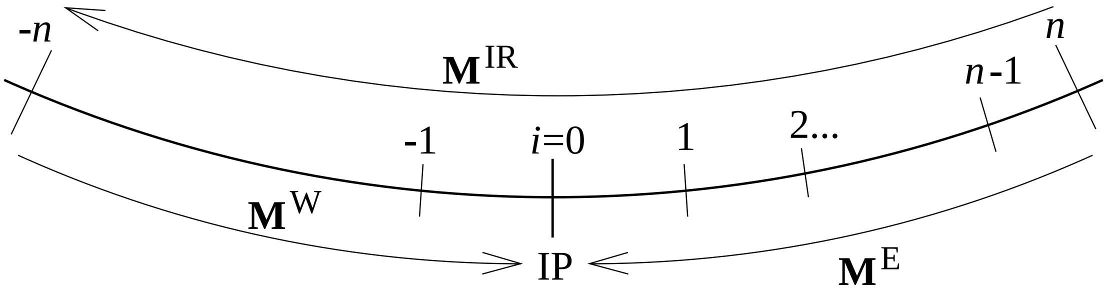

Figure 4.1: A schematic definition of $\mathbf{M}^{\mathrm{IR}}$, the transfer matrix from east to west through the interaction region (IR); $\mathbf{M}^{\mathrm{E}}$, the transfer matrix from the east end of the IR to the interaction point (IP); and $\mathbf{M}^{\mathrm{W}}$, the transfer matrix from the IP to the west end of the IR.

row of the transport matrices from the arcs to the IP must be zero,

$$M^{\mathrm{E}}_{31} = 0, \quad M^{\mathrm{E}}_{32} = 0, \quad M^{\mathrm{W}}_{31} = 0, \quad M^{\mathrm{W}}_{32} = 0. \tag{4.2}$$

3. If the compensation takes place within a region that contains no dipole magnets, then no vertical dispersion will be introduced at the IP. Since the solenoid is compensated by rolling the first three quadrupoles on either side of the IP, this is automatically true.

The above equations seem to imply that as many as twelve variable parameters are needed to achieve compensation, eight to make $\mathbf{M}^{\mathrm{IR}}$ block diagonal and four to satisfy Equations 4.2. However, transfer matrices are symplectic, which means that $\mathbf{M}^T\ \mathbf{S}\ \mathbf{M} = \mathbf{S}$ where $\mathbf{M}^T$ is $\mathbf{M}$ with rows and columns transposed and $\mathbf{S}$ is a $2k \times 2k$ matrix with $\begin{pmatrix} 0 & -1 \\ 1 & 0 \end{pmatrix}$ along the k 2×2 diagonal blocks and zeroes elsewhere[5]. For an arbitrary 4×4 symplectic matrix if one of the 2×2 off-diagonal blocks is zero, then the other off-diagonal block is zero as well. Also, for an interaction region containing a solenoid and anti-symmetric skew quadrupoles,

$$M_{31}^{\mathrm{W}} = -M_{31}^{\mathrm{E}}, \quad M_{32}^{\mathrm{W}} = M_{32}^{\mathrm{E}} \tag{4.3}$$

As mentioned in Chapter 3, for weak coupling any transfer matrix can be written as the product of the ideal uncoupled matrix and a "projection" matrix, so $\mathbf{M}^{\mathrm{E}}$ can be written as

$$\mathbf{M}^{\mathrm{E}} = \mathbf{M}^{\mathrm{E}'}\mathbf{M}^{\mathrm{E^o}}, \tag{4.4a}$$

$$\mathbf{M}^{\mathrm{E}'} = \begin{pmatrix} \mathbf{I} & \mathbf{F} \\ -\mathbf{F}^{\dagger} & \mathbf{I} \end{pmatrix}, \tag{4.4b}$$

$$\mathbf{M}^{\mathrm{E^o}} = \begin{pmatrix} \mathbf{M}_x & \mathbf{0} \\ \mathbf{0} & \mathbf{M}_y \end{pmatrix}, \tag{4.4c}$$

where $\mathbf{F}$ is a sum of projection matrices. The derivation of the above formulas is explained in more detail in Appendix A and in the references[19, 22]. A similar matrix, $\mathbf{M}^{\mathrm{IR}'}$, can be defined defined for transport across the IR. Assuming that the compensating elements are pairs of anti-symmetrically powered skew quadrupoles, then with a little algebra it is possible to show the following:

- If $M_{31}^{\mathrm{E}'} = 0$ and $M_{32}^{\mathrm{E}'} = 0$, then $M_{31}^{\mathrm{E}} = 0$ and $M_{32}^{\mathrm{E}} = 0$.
- If $\mathbf{M}^{\mathrm{IR}'}$ is block diagonal, then $\mathbf{M}^{\mathrm{IR}}$ is block diagonal also.
- If $M_{31}^{\mathrm{E}'} = 0$, $M_{32}^{\mathrm{E}'} = 0$, and $M_{42}^{\mathrm{E}'} = 0$, then $\mathbf{M}^{\mathrm{IR}'}$ is block diagonal.

Thus, to compensate the solenoid there are really only three constraints on the transfer matrices,

$$M_{31}^{\mathrm{E}'} = 0, \tag{4.5a}$$

$$M_{32}^{\mathrm{E}'} = 0, \tag{4.5b}$$

$$M_{42}^{\mathrm{E}'} = 0, \tag{4.5c}$$

so three pairs of skew quadrupoles are sufficient.

Assuming $\alpha_x^* = \alpha_y^* = 0$, then in terms of the β-functions and skew quadrupole strengths, Equations 4.5 become

$$\sum_i \tilde{q}_i S_y^i C_x^i + \theta\sqrt{\beta_x^*/\beta_y^*} = 0, \tag{4.6}$$

$$-\sum_i \tilde{q}_i S_x^i C_y^i + \theta\sqrt{\beta_y^*/\beta_x^*} = 0, \tag{4.7}$$

$$\sum_i \tilde{q}_i S_y^i S_x^i = 0. \tag{4.8}$$

where $\tilde{q}_i = q_i/\sqrt{\beta_x^i \beta_y^i}$ is the "normalized" strength of the skew quadrupoles, θ is the strength of the solenoid[2], $S_{x,y}^i = \sin\phi_{x,y}^i$, and $C^i = \cos\phi_{x,y}^i$. Each of the skew quadrupoles is characterized by an array of the coefficients, $V_i = (S_y^i C_x^i, -S_x^i C_y^i, S_y^i S_x^i)^T$. An economical arrangement of the skew quadrupoles has the V_i's nearly orthogonal. If such an arrangement is not possible, then the skew quadrupoles may need to be quite strong.

An assumption made in deriving Equation 4.8 was that the solenoid's transfer matrix could be approximated as a small angle rotation ignoring the focusing effect at the ends of the solenoid. In practice, the focusing at the ends of the solenoid cannot be ignored, however, in most cases, solving Equation 4.8 is a good first first approximation. More general forms for $\mathbf{M}^{\mathrm{E}}$ and $\mathbf{M}^{\mathrm{E}'}$ which can be used to refine the solution and which do not assume knowledge of the β-functions, are

$$\mathbf{M}^{\mathrm{E}} = \begin{pmatrix} \mathbf{A}^{\mathrm{E}} & \mathbf{B}^{\mathrm{E}} \\ \mathbf{C}^{\mathrm{E}} & \mathbf{D}^{\mathrm{E}} \end{pmatrix} \tag{4.9a}$$

$$\mathbf{M}^{\mathrm{E}'} = \mathbf{M}^{\mathrm{E}} \begin{pmatrix} \mathbf{A}_{\mathrm{E}}^{-1} & \mathbf{0} \\ \mathbf{0} & \mathbf{D}_{\mathrm{E}}{}^{-1} \end{pmatrix} = \begin{pmatrix} \mathbf{1} & \mathbf{B}^{\mathrm{E}'} \\ \mathbf{C}^{\mathrm{E}'} & \mathbf{1} \end{pmatrix}. \tag{4.9b}$$

Multiplying $\mathbf{M}^{\mathrm{E}'}$, Equations 4.5 expressed in terms of elements of $\mathbf{M}^{\mathrm{E}}$ are

$$M_{31}^{\mathrm{E}'} = M_{31}^{\mathrm{E}} M_{22}^{\mathrm{E}} - M_{32}^{\mathrm{E}} M_{21}^{\mathrm{E}} = 0, \tag{4.10a}$$

[2] $\theta = KL$, where L is the length of the solenoid and K is the strength of the solenoid. If B_0 is the longitudinal field of the solenoid, then $K = \frac{B_0}{2p/e}$.

$$M_{32}^{\mathrm{E}'} = M_{32}^{\mathrm{E}} M_{11}^{\mathrm{E}} - M_{31}^{\mathrm{E}} M_{12}^{\mathrm{E}} = 0, \tag{4.10b}$$

$$M_{42}^{\mathrm{E}'} = M_{42}^{\mathrm{E}} M_{11}^{\mathrm{E}} - M_{41}^{\mathrm{E}} M_{12}^{\mathrm{E}} = 0. \tag{4.10c}$$

If thin element skew quadrupoles are used in multiplying out $\mathbf{M}^{\mathrm{E}}$, then Equations 4.10c are polynomials in powers of the skew quadrupole strengths and are solved with a symbolic algebra program, such as Mathematica. If thick element skew quadrupoles are used, Equations 4.10c are polynomials in powers of transcendental functions of the skew quadrupole strength.

In the course of compensating the solenoid, the β-functions become distorted, which is a serious problem. The solution used at the time these experiments began was to treat the solenoid, rotated quadrupoles, and a few normal quadrupoles as an insert, and adjust quadrupole strengths and angles until the insert matched the β-functions at the IP and at the junction with the arcs. This solution was chosen because the lattice design machinery used at that time assumed an uncoupled machine. Later, the software package for designing CESR lattices was updated to handle weak coupling as simply another variable to be optimized, and the insert approach was abandoned.

4.3 Requirements for Injection

The injected bunch is accelerated to its full energy in a synchrotron before being transfered into CESR. During the injection cycle, the stored bunch's orbit is temporarily altered to bring it as close as possible to the injected bunch at the injection point. The injected bunch enters CESR at an angle and displaced from the orbit of the stored bunch and thus executes betatron oscillations about the stored bunch. The injected bunch may also be displaced longitudinally with respect to the stored bunch and thus oscillate relative to the stored beam in that dimension as well. Eventually, due to radiation effects, these oscillations damp down to the stored beam trajectory. In CESR, $\tau_x \approx \tau_y \approx 22$ msec (about 1000 turns), and $\tau_z \approx 13$ msec (about 500 turns). The initial amplitude of these oscillations depends on the separation between the injected and stored bunches, $\mathbf{X}_{inj} = (x_{inj}, x'_{inj}, y_{inj}, y'_{inj}, z_{inj}, \delta_{inj})^T$ (where z is the longitudinal displacement and δ is the fractional energy displacement), and care must be taken to insure that nowhere is this amplitude larger than the physical aperture of CESR. What follows is a discussion of injection that largely follows the treatment in Seeman[23]. Since the discussion concerns horizontal motion only, the subscript x has been dropped from the β-functions and dispersion to simplify the notation.

The injected bunch may differ in energy from the stored bunch, so the horizontal position and slope of the reference orbit of the stored and injected bunch will differ by $\delta\ \eta_{x,inj}$ and $\delta\ \eta'_{x,inj}$ respectively. The initial betatron amplitude of the injected bunch will be

$$x_{\beta,inj} = x_{inj} - \delta\ \eta_{inj}, \tag{4.11}$$

$$x'_{\beta,inj} = x'_{inj} - \delta\ \eta'_{inj}. \tag{4.12}$$

The resulting motion in CESR has two parts, betatron motion and energy oscillation,

$$x(s) = x_\beta(s) + \delta\ \eta(s). \tag{4.13}$$

The maximum excursion of the injected beam from the stored beam at a particular azimuthal position will be the sum of the betatron amplitude and the maximum energy excursion times the dispersion function,

$$\begin{aligned} X_{max}(s) &= x_\beta(s)|_{max} + |\delta_{max}|\eta(s), \\ &= \sqrt{W\beta(s)} + |\delta_{max}|\eta(s), \end{aligned} \tag{4.14}$$

where W is the Courant-Snyder invariant, $W \equiv [x^2 + (\beta x' + \alpha x)^2]/\beta$, or more explicitly, by substituting in expressions for W and $|\delta_{max}|$,

$$X_{max}(s) = \sqrt{\frac{\beta(s)}{\beta_{inj}}}\Big\{(x_{inj} - \eta_{inj}\delta_{inj})^2 +$$
$$\left[\beta_{inj}(x'_{inj} - \eta'_{inj}\delta_{inj}) + \alpha_{inj}(x_{inj} - \eta_{inj}\delta_{inj})\right]^2\Big\}^{\frac{1}{2}}$$
$$+ \left[\delta_{inj}^2 + (\frac{\Omega}{c\alpha_p}\Delta z_{inj})^2\right]^{\frac{1}{2}} \eta(s), \tag{4.15}$$

where Ω is the tune of the synchrotron motion, c is the speed of light, and α_p is the momentum compaction[3]. For $\delta_{inj} = 0$ and $\Delta z_{inj} = 0$, the second term becomes zero, and X_{max} becomes

$$X_{max}(s) = \sqrt{\frac{\beta(s)}{\beta_{inj}}}\left[x_{inj}^2 + (\beta_{inj}x'_{inj} + \alpha_{inj}x_{inj})^2\right]^{\frac{1}{2}}. \tag{4.16}$$

It is desirable to make $X_{max}(s)$ as small as possible everywhere so that the injected bunch does not impact on the physical aperture. The minimum occurs when

$$x'_{inj} = -x_{inj}\frac{\alpha_{inj}}{\beta_{inj}}, \tag{4.17}$$

which can be achieved by adjusting the trajectory of the injected bunch as it passes from the synchrotron into CESR. When Equation 4.17 is satisfied,

$$X_{max}(s) = \sqrt{\frac{\beta(s)}{\beta_{inj}}}|x_{inj}|, \tag{4.18}$$

so as one might expect, to minimize X_{max} further, x_{inj} should be as small as possible. The minimum practical x_{inj} depends on the dimensions of the injection septum and the sizes of stored and injected beam, which are illustrated in Figure 4.2[23]. Since this figure was made, a new septum has been installed in CESR, and $x_{wall} = 3$ mm.

[3] See the reference [14] for an explanation of momentum compaction.

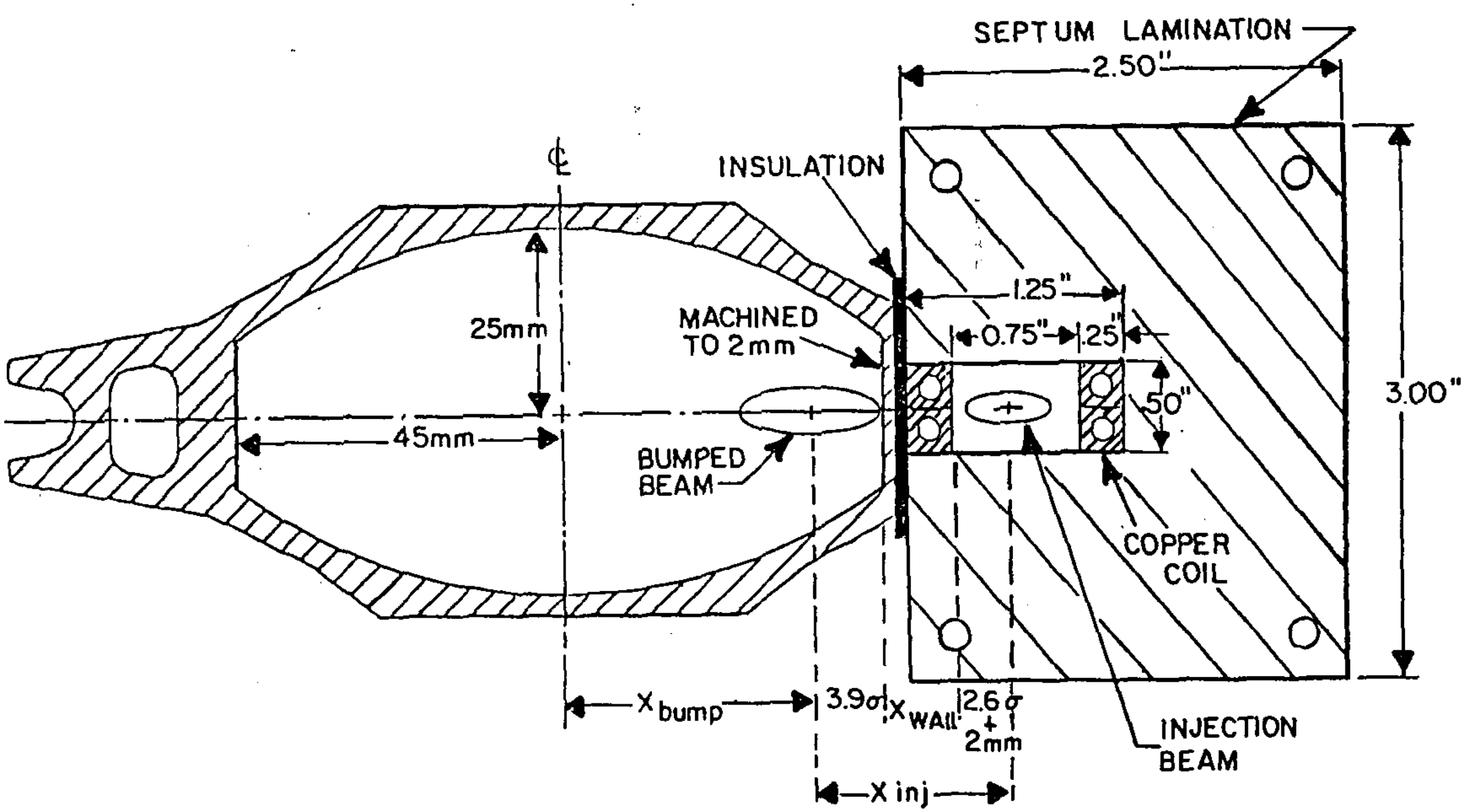

Figure 4.2: The cross section of the injection septum and CESR beam pipe[23]. Since this drawing was made, a new septum has been installed in CESR with a thinner wall, $x_{\text{new wall}} = 3$ mm.

In order to make x_{inj} as small as possible, a pulsed bump is used, which is made up of three pulsed kickers, two located upstream and one downstream of the septum, that are turned on and off in unison during the injection cycle to bring the stored bunch as close as possible to the septum. (The kickers cycle on and off in 15 μs, which is about six revolution periods.) Their relative strengths are such that outside the area of the septum, the orbit of the stored bunch is unaffected, or in other words, the orbit distortion due to the kickers forms a closed bump. Figure 4.3 illustrates the general characteristics of this bump[23]. The bump is double-lobed so that there will be no overall change in path length for the stored bunch.

If $\delta < 0$, then the reference orbit about which the injected bunch will oscillate is displaced toward the septum, and x_{inj} is smaller at the expense of making the second term in X_{max} non-zero everywhere $\eta(s)$ is non-zero. However, the largest β_x occur in the interaction region where $\eta_x = 0$, so injecting off-energy has the potential to decrease the aperture needed by the injected beam at just the place where it would help the most.

To further reduce X_{max}, a fast kicker, called a pinger, may be used. If fired on the right turn, the pinger changes the angle of the injected bunch's trajectory to bring it closer to the reference orbit of the stored bunch. In other words, the pinger can reduce the Courant-Snyder invariant of the injected bunch. For instance, if on a particular turn the horizontal position of the bunch is zero at the pinger, then before the kick, the angle of the injected bunch must be related to W_{inj} by

$$W_{inj} = \beta_{ping}(x'_{ping})^2, \tag{4.19}$$

where $W_{inj} = \left[x_{inj}^2 + (\beta_{inj}x'_{inj} + \alpha_{inj}x_{inj})^2\right]/\beta_{inj}$. Assuming that injection is done on-energy and x_{inj} has been adjusted to minimize X_{max}, then from Equations 4.14

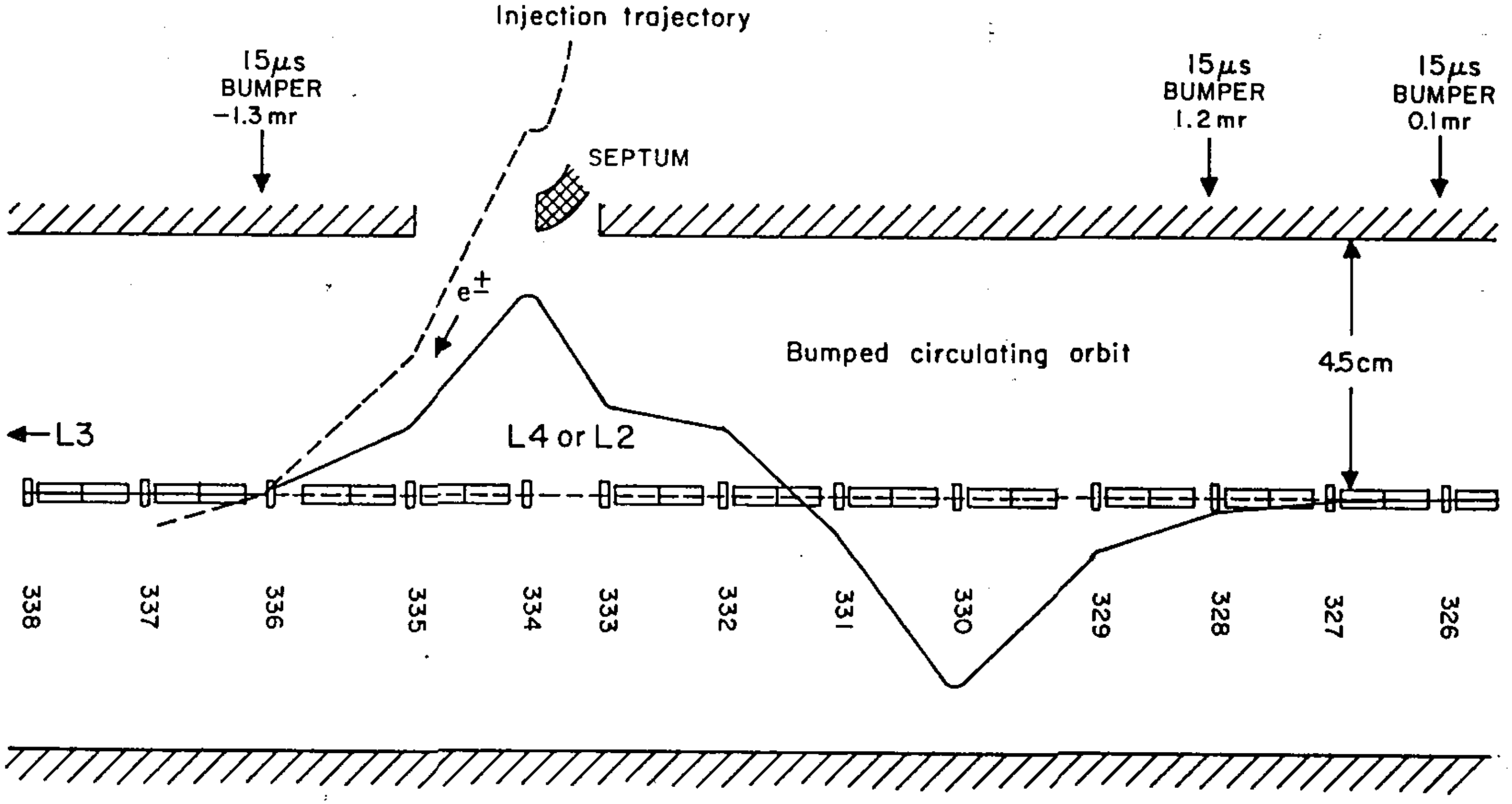

Figure 4.3: An example of the orbits of the stored and injected bunches with the pulsed bump[23]. The numbers 326-338 identify particular quadrupoles in CESR. The amplitudes of the kickers necessary to form a closed bump (-1.3 mrad, 1.2 mrad, and 0.1 mrad in the figure) will depend on the β-functions and betatron phase advances of the particular lattice.

and 4.18

$$W_{inj} = \frac{x_{inj}^2}{\beta_{inj}}, \tag{4.20}$$

After the kick, $x'_{ping} \rightarrow x'_{ping} + \theta_{ping}$, so the Courant-Snyder invariant becomes

$$W = \beta_{ping}(x'_{ping} + \theta_{ping})^2, \tag{4.21}$$

$$= W_{inj}\left(1 + \frac{\theta_{ping}}{x'_{ping}}\right), \tag{4.22}$$

and $X_{max}(s) = \sqrt{W\beta(s)}$ is reduced by $\left(1 + \frac{\theta_{ping}}{x'_{ping}}\right)^{\frac{1}{2}}$. Of course, the benefit of reducing X_{max} comes at the cost of inducing betatron oscillations in the stored bunch. While these will damp, if the initial amplitude is too large, the stored beam will come too close to the physical aperture, reducing its lifetime.

4.4 Requirements for Separation

If electrons and positrons circulate in opposite directions in a storage ring made up of only magnetic elements, they will travel on the same orbit, so n bunches of positrons and n bunches of electrons will collide in $2n$ locations; however, the equations for the coherent π mode tune shift in Chapter 2 assume only one collision point. Those equations can be extended to more than one collision point, but this complicates the analysis. Also, only in the CLEO-II detector can luminosity be measured. Thus, some sort of separation is needed on the north side of the ring during collisions. In addition, injection into CESR is done by first injecting positrons, then electrons, and while it is possible to inject electrons directly into collisions, it is generally preferable to separate the beams at the IP as well during injection. Electrostatic elements will cause the electron and positron orbits to be different, so they can be used to prevent unwanted collisions.

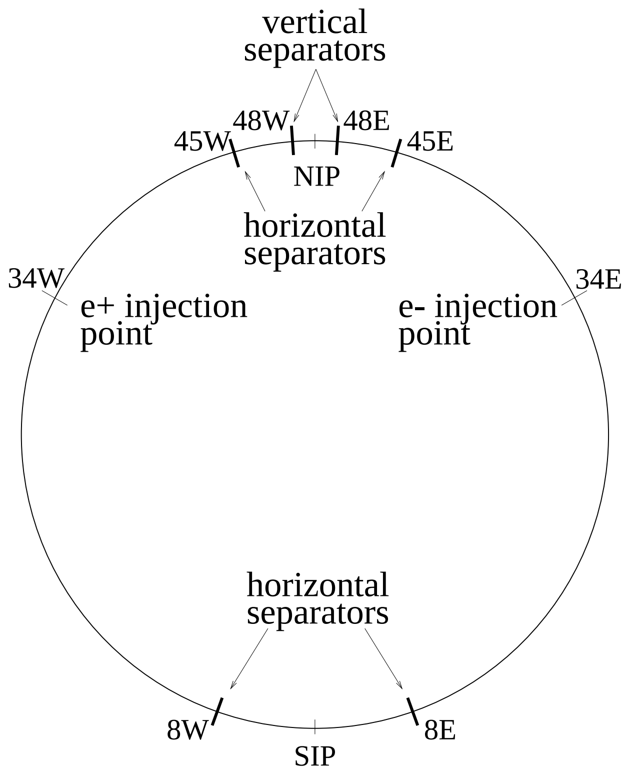

Figure 4.4: The locations of horizontal and vertical separators and the injection points in CESR relative to the north and south interaction points.

4.4.1 Resonantly Coupled Round Beams

Figure 4.4 shows the locations of the horizontal and vertical separators and the injection points in CESR. The separators are electrostatic kickers, so they are capable of making the electron and positron orbits different from one another. Even with only a single bunch per beam for the round beam collisions, there is still an extra collision point in the north. The vertical separators are conveniently positioned so that they can create an electrostatic bump that separates the electron and positron orbits at the NIP.

A kick on every turn at location s_1 produces a distortion in the closed orbit,

$$\Delta y(s) = \theta \frac{\sqrt{\beta_y(s_1)\beta_y(s)}}{2\sin \pi Q_y} \cos\left(\overline{\phi_y(s) - \phi_y(s_1)} - \pi Q_y\right), \tag{4.23}$$

where θ is the kick, and $\overline{\phi_y(s) - \phi_y(s_1)}$ is the betatron phase advance from the location of the kick, s_1, to an arbitrary position, s, modulo $2\pi Q_y$. The effects of multiple kicks can be superposed on one another, so just after the second vertical separator,

$$\Delta y = \theta_1 \frac{\beta_{y,1}}{2\sin 2\pi Q_y} \cos(\Delta\phi_y - \pi Q_y) + \theta_2 \frac{\beta_{y,2}}{2\sin 2\pi Q_y} \cos(-\pi Q_y). \tag{4.24}$$

where $\Delta\phi_y$ is the vertical betatron phase advance between the separators and $\beta_y(s_1) = \beta_y(s_2)$ due to the symmetry of CESR. Δy will be zero, closing the bump, if $\theta_1 = \theta_2$ and $\Delta\phi_y = \pi$. Since the separators deflect electrons and positrons in opposite direction, at the center of the bump the bunches will be separated by $2\Delta y = 2\theta_1\sqrt{\beta_y(s_1)\beta_y(s_N)}$.

During normal high energy physics operation, separation at all other unwanted collision points is accomplished using separators that make horizontal deflections. The horizontal separators are also arranged so that the bunches to collide at an angle, allowing closer spacing of the bunches and therefore more bunches in CESR. To prevent collisions during electron injection, the strengths of the horizontal separators are changed slightly to displace the orbits horizontally at the IP. For round beam electron injection the horizontal separators were used in a similar way, then turned off to bring the beams into head-on collisions, since collisions at an angle would destroy the symmetry of round beam collisions.

4.4.2 Möbius Insert

Beams in a Möbius lattice will also need separation in the north and south during injection and in the north during collisions for the same reasons as the resonantly coupled round beams. However, separation in the north is complicated by the fact that the Möbius insert is located between the vertical separators, so a vertical kick on one side cannot be canceled by the other vertical separator. Ideally, one would like to have one vertical and one horizontal separator in the north with the right phase advance between them. Since, when the CLEO solenoid has been compensated, there is no net coupling in the rest of the ring, the two southern horizontal separators powered symmetrically with $n\pi$ phase advance between them could be used to separate the beams at the IP during injection in the same way that the vertical separators are normally used in the north.

Using the notation of Chapter 3 and assuming that the match point of the Möbius insert is in the center of the vertical separators, J and J' will denote the locations of the vertical separators, and H and H' will denote the locations of the two north horizontal separators. The same symmetry applies so that $\beta_{H'} = \beta_H$ and $\alpha_{H'} = -\alpha_H$; however, the horizontal and vertical β-functions are not necessarily equal at H and H'. The betatron phase advances from J to H and from J' to H' are $\phi_{x,y}$. The transfer matrix from the vertical separator at J through the rolled Möbius insert to the horizontal separator at H' is thus

$$\begin{aligned}
\mathbf{M}_{H'\leftarrow J} &= \mathbf{M}_{H'\leftarrow J'}\mathbf{M}^R_{J'\leftarrow J} \\
&= \begin{pmatrix} \mathbf{T}(\beta_{x,H'}, \alpha_{x,H'}; \beta_J, -\alpha_J; \phi_x) & \mathbf{0} \\ \mathbf{0} & \mathbf{T}(\beta_{y,H'}, \alpha_{y,H'}; \beta_J, -\alpha_J; \phi_y)) \end{pmatrix} \\
&\times \begin{pmatrix} \mathbf{0} & \mathbf{T}(\beta_J, -\alpha_J; \beta_J, \alpha_J, \psi) \\ \mathbf{T}(\beta_J, -\alpha_J; \beta_J, \alpha_J; \psi) & \mathbf{0} \end{pmatrix}
\end{aligned}$$

$$= \begin{pmatrix} \mathbf{0} & \mathbf{T}(\beta_{x,H'}, \alpha_{x,H'}; \beta_J, \alpha_J; \psi + \phi_x) \\ \mathbf{T}(\beta_{y,H'}, \alpha_{y,H'}; \beta_J, \alpha_J; \psi + \phi_y) & \mathbf{0} \end{pmatrix}. \tag{4.25}$$

A vertical kick at J, $\mathbf{X}_J = (0, 0, 0, \theta_y)^T$, becomes a horizontal angle and displacement on the other side of the Möbius insert, and at H'

$$\mathbf{X}_{H'} =$$

$$\begin{pmatrix} \mathbf{0} & \mathbf{T}(\beta_{x,H'}, \alpha_{x,H'}; \beta_J, \alpha_J; \psi + \phi_x) \\ \mathbf{T}(\beta_{y,H'}, \alpha_{y,H'}; \beta_J, \alpha_J; \psi + \phi_y) & \mathbf{0} \end{pmatrix} \begin{pmatrix} 0 \\ 0 \\ 0 \\ \theta_y \end{pmatrix},$$

$$= \begin{pmatrix} \theta_y \sqrt{\beta_J \beta_{x,H'}} \sin(\psi + \phi_x) \\ \theta_y \sqrt{\frac{\beta_J}{\beta_{x,H'}}} [\cos(\psi + \phi_x) - \alpha_{x,H'} \sin(\psi + \phi_x)] \\ 0 \\ 0 \end{pmatrix}. \tag{4.26}$$

So to make a closed bump,

$$\sin(\psi + \phi_x) = 0 \;\Rightarrow\; \psi + \phi_x = n\pi, \text{and} \tag{4.27}$$

$$\theta_x = \pm \theta_y \sqrt{\frac{\beta_J}{\beta_{x,H'}}} \quad \begin{cases} + \text{ if } \psi + \phi_x = \pi, 3\pi, \ldots \\ - \text{ if } \psi + \phi_x = 2\pi, 4\pi, \ldots \end{cases}. \tag{4.28}$$

One disadvantage to the scheme of separation at the NIP is that since the vertical separator on one side of the Möbius insert and horizontal separator on the other side are not symmetrically positioned with respect to the IP, and since part of the bump is vertical and part of the bump is horizontal, the electron orbit and the positron orbit will not be the same. Their path lengths may be different leading to different beam sizes for each beam. This was thought to be one of the downfalls of the previous round beam experiment[4], so in designing a Möbius lattice for CESR, this should be taken into account. Since that is beyond the scope of this dissertation it will not be discussed further here.

Chapter 5
Simulations of Performance

5.1 Lattice Description

The input for TEAPOT (Thin Element Accelerator Program for Optics and Tracking) is a magnet by magnet description of a storage ring or transfer line, along with a set of commands for manipulating the lattice and tracking particle motion[24]. The magnetic and electrostatic elements are assumed to be "thin." For instance, a quadrupole of length L and strength K is modeled as a thin lens with focal length f, where $1/f = KL$, sandwiched between two drifts. Any "thick" (*i.e.* strong) elements can be represented by a sufficient number of thin elements in series. Longitudinal effects are included wherever RF cavities are included in the lattice description.

Figure 5.1 shows a closeup of the region between the NIP and one of the vertical separators with longitudinal lengths to scale. (A view of the positions of the separators with respect to the north and south IPs may be seen in Figure 4.4.) This configuration is mirrored on the other side of the NIP. Presently, it is possible to rotate the quadrupoles, labeled Q48, Q49, and Q50, by $\pm 45°$ about their axes, enabling this region to become a Möbius insert. However, at the time of the resonantly coupled round beam collisions, Q50 and the rotating platforms

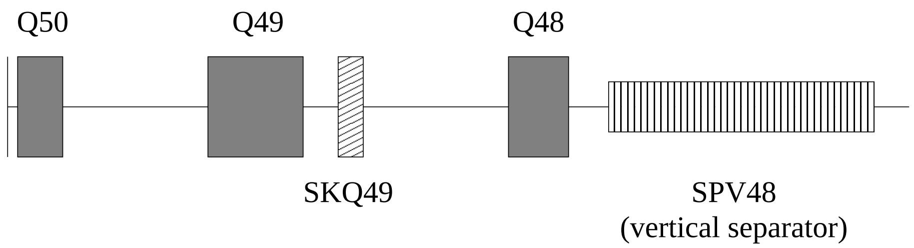

Figure 5.1: A close-up of the region between a vertical separator and the NIP. This arrangement is mirrored on the other side of the NIP, and the longitudinal lengths are to scale. The quadrupole labeled Q50 did not exist during the resonantly coupled round beam experiments and was installed for later use in a Möbius lattice.

for Q48 and Q49 had not been installed. A pair of skew quadrupoles, one on either side of the NIP and labeled SKQ49 in the figure, provided the coupling to make the beams round as described in Section 3.1.

Figure 5.2 shows a closeup of the interaction region from the SIP up to, but not including, the first bending magnet with longitudinal lengths to scale. This configuration is also mirrored on the other side of the SIP. The length of the CLEO-II solenoid shown is slightly longer than the physical length of the solenoid to include the effects of the fringe field, and this length has been empirically determined[25]. The three IR quadrupoles, labeled REQ (for **R**are **E**arth **Q**uadrupole, a permanent magnet), Q01, and Q02, can be rotated about their axes by an arbitrary small angle to compensate the CLEO-II solenoid, as described in Chapter 4 and Appendix A. Skew quadrupoles, such as the ones labeled SKQ02 and SKQ03 in the figure, are sometimes used during operations to fine tune the compensation.

Notice that REQ is positioned partially inside the solenoid. The TEAPOT lattice description commands do not include a way to directly describe overlap-

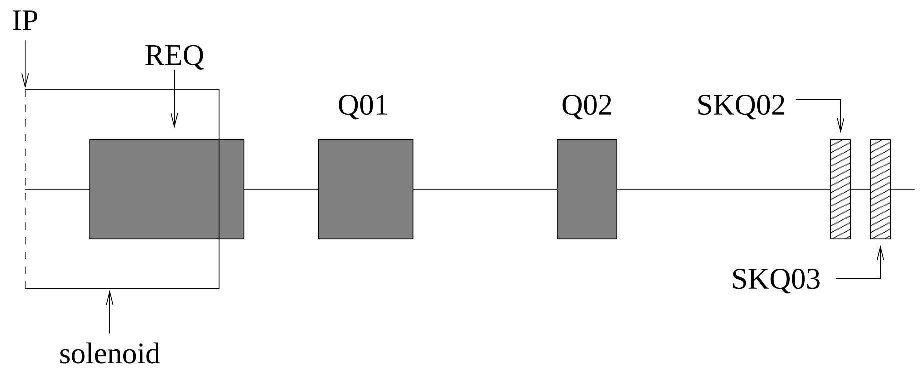

Figure 5.2: A close-up of one half of the interaction region up to, but not including, the first dipole. This arrangement is mirrored on the other side of the SIP, and the longitudinal lengths are to scale. The quadrupoles labeled REQ, Q01, and Q02 can be rotated about their axes by small angles in order to compensate the CLEO-II solenoid. The extent of the solenoid pictured here is an empirically derived length that includes the fact that the field extends slightly beyond the physical structure. The method by which the overlapping quadrupole and solenoid fields were modeled in TEAPOT is illustrated in Figure 5.3.

ping quadrupole and solenoid fields. This was overcome by modeling REQ by an alternating series of short quadrupoles and solenoids, as shown schematically in Figure 5.3. The total length of the quadrupole pieces is one half the total length of the REQ, so the strength of each must be twice the actual strength of the REQ. Similarly the solenoid pieces are twice the strength of the actual solenoid, except the end piece, the length of which was chosen so that the sum of KL for the pieces is equal to KL for the whole. A "fake" skew quadrupole of negligible length is included in the centers of all the IR quadrupoles (REQ, Q01, and Q02) for the purpose of adjusting the solenoid compensation, since TEAPOT's routine for global decoupling adjusts only skew quadrupole strengths.[1]

Tables 5.1 through 5.3 list some pertinent parameters calculated for the ideal theoretical lattices.

[1] A quadrupole of length L and strength K that has been rotated about its axis by an arbitrary angle ϕ about its axis can be represented as the superposition of a normal quadrupole with $1/f = KL\cos 2\phi$ and a skew quadrupole with $1/f = -KL\sin 2\phi$. This superposition can be accomplished in TEAPOT by placing a skew quadrupole of negligible length in the center of a normal quadrupole.

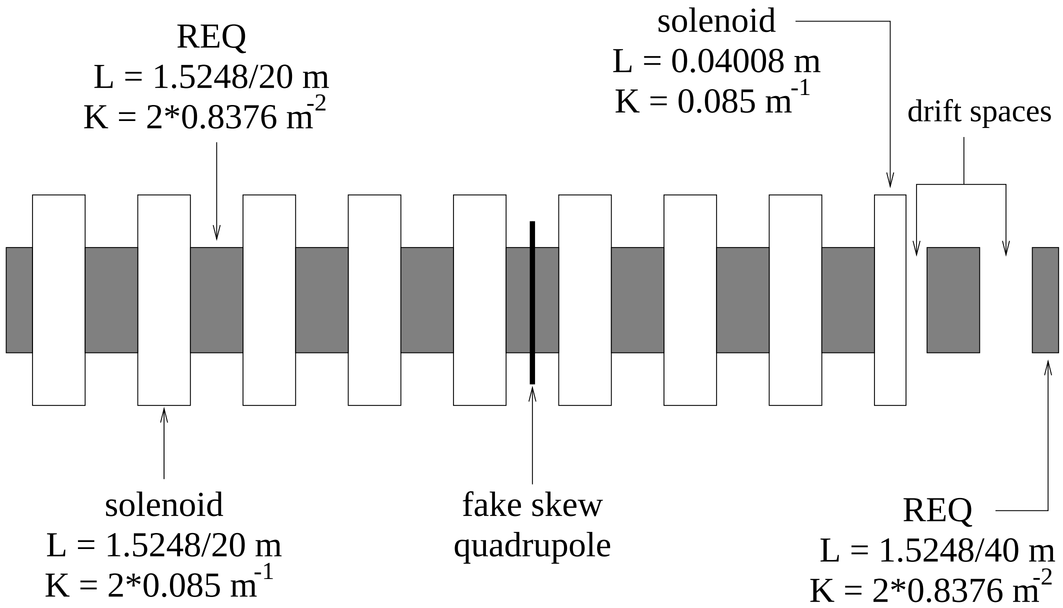

Figure 5.3: Schematic representation of the method used to model the overlapping solenoid and quadrupole fields in TEAPOT using an alternating series of short quadrupoles and solenoids. The total length of quadrupole pieces is one half the total length of the REQ, so the strength of each must be twice the strength of the REQ. Similarly the solenoid pieces are twice the strength of the actual solenoid, except the end piece, the length of which was chosen so that $\Sigma(KL)_i$ of the pieces is equal to KL for the whole. Since a quadrupole rolled by an arbitrary angle about its axis can be represented by an upright quadrupole and a skew quadrupole in series, a "fake" skew quadrupole of negligible length was included to allow TEAPOT to adjust the solenoid compensation.

Table 5.1: Calculated lattice parameters of the original resonantly coupled round beam lattice, designated E9A242400.JJ1_4S. At the time this lattice was designed, the lattice design software assumed zero coupling, so the solenoid compensation was designed as an insert.

Q_y	9.7700
Q_x	10.7701
ε_x	142 nm-rad

	SIP	NIP
β_y	0.237 m	7.842 m
β_x	0.243 m	0.833 m
η_x	0.001 m	0.073 m

At the injection point	
$\beta_{x,inj}$	34.65 m
$\eta_{x,inj}$	1.32 m

Table 5.2: Calculated lattice parameters for the final resonantly coupled round beam lattice, designated E9A303000.JJ1_4S_15KG. At the time this lattice was designed, weak coupling had been incorporated into the lattice design software, so that solenoid compensation was incorporated from the start.

Q_y	9.7700
Q_x	10.7705
ε_x	138 nm-rad

	SIP	NIP
β_y	0.300 m	7.543 m
β_x	0.301 m	0.830 m
η_x	0.000 m	0.161 m

At the injection point	
$\beta_{x,inj}$	35.16 m
$\eta_{x,inj}$	3.33 m

Table 5.3: Calculated lattice parameters for a preliminary Möbius lattice (all quadrupoles erect), designated D9B272706.FD1_4S. At the time this lattice was designed, the lattice design software assume zero coupling, so the solenoid compensation was designed as an insert.

Q_y	9.6177
Q_x	11.5547
ε_x	134 nm-rad

	SIP	NIP
β_y	0.271 m	10.593 m
β_x	0.304 m	5.162 m
η_x	0.065 m	-0.002 m

5.2 Dynamic Aperture

To lowest order, the only effect of small variations in energy on a particle's motion is to displace its reference orbit by $\eta_x \delta$, where $\delta = \Delta E/E$; that is to say, the net horizontal displacement is a sum of the betatron motion and the location of the off-energy reference orbit, $x = x_\beta + x_\delta = x_\beta + \eta_x \delta$. However, strictly speaking, the focusing strength of a quadrupole depends on the momentum of the particle, $f/f_0 = p/p_0$, so the tune of a particle's betatron motion depends on δ. (For highly relativistic beams, like the electron and positron beams in CESR, $pc \simeq E$, so p and E are often used interchangeably.) This variation of tune with energy is called chromaticity, $Q' \equiv \Delta Q/\Delta\delta$, and its natural value is typically $\approx -2Q$. This gives the particle distribution a spread of tunes, which may place a portion of the beam on resonance. Additionally, the "head-tail" effect[2] is stable only for zero and slightly positive chromaticities[26]. To an off-energy particle a sextupole placed where $\eta_x \neq 0$ "looks" like a quadrupole,

Quadrupole	Sextupole
on-energy particle	off-energy particle
$B_y = B' x_\beta$	$B_y = B''(\eta_x\delta) x_\beta$
$B_x = B' y_\beta$	$B_x = B''(\eta_x\delta) y_\beta$

Thus, the chromatic effect of the sextupoles can be used to compensate the natural chromaticity,

$$\Delta Q'_x = \frac{1}{2\pi}\left(\sum(\beta_x\eta_x S_F + \beta_x\eta_x S_D)\right) \tag{5.1a}$$

$$\Delta Q'_y = -\frac{1}{2\pi}\left(\sum(\beta_y\eta_x S_F + \beta_y\eta_x S_D)\right), \tag{5.1b}$$

[2] The "head-tail" effect is the potentially destabilizing effect of the wake field of the bunch on itself. Modeling the bunch as two macroparticles, the "tail" particle feels a force due to the wake field of the "head" particle that oscillates at its own natural frequency, the betatron tune. Half way through the synchrotron period, their roles switch, which has a stabilizing effect, but only for low currents. When the variation of the betatron tune with energy is included, the motion turns out to be stable for zero and slightly positive chromaticities[26].

where S is the strength of the sextupole, the subscripts F and D identify "families" of sextupoles that are focusing and defocusing in the horizontal plane respectively, and the sign convention is $S_F > 0$, $S_D < 0$. Since the strengths of the two families of quadrupoles have opposite sign, and since $\Delta Q' > 0$ is desired, focusing sextupoles are placed next to focusing quadrupoles (β_x is relatively large, and β_y is relatively small), and defocusing sextupoles are placed next to defocusing quadrupoles (β_x is relatively small, and β_y is relatively large). Even so, each family partially cancels the effect of other, so the sextupoles may need to be quite strong.[3]

The unfortunate side effect of chromaticity compensation is that it forces the introduction of (possibly strong) nonlinear fields into the lattice, which can restrict the dynamic aperture. With only linear elements (dipoles and quadrupoles), particle trajectories in normalized phase space are circles, no matter how large the initial amplitude. When nonlinear fields are added, at small amplitudes, the phase space trajectories are still approximately circular, but at large enough initial amplitudes, the motion is chaotic and unbounded. The stable region of phase space is called the dynamic aperture. Due to the complicated nature of nonlinear motion, tracking simulations are used to find the dynamic aperture of a lattice. Figure 5.4 shows the results of one such simulation that I did using the preliminary Möbius lattice with the Möbius section rolled. Particles were launched at the SIP with $\delta = 0\sigma_\delta$, $2\sigma_\delta$, $4\sigma_\delta$, and $6\sigma_\delta$ ($\sigma_\delta = \sigma_E/E$) then tracked for about one quarter damping period. The initial transverse coordinates, $(x, y)_0$, were adjusted to find the edge of the dynamic aperture. The irregularity of the contours is due to the nature of the algorithm for adjusting $(x, y)_0$, not to characteristics of the Möbius

[3] One of the potential advantages of the Möbius lattice over the resonantly coupled round beam lattice is the ability to take advantage of "chromaticity sharing"[3]. Preliminary observations of chromaticity sharing have been done at CESR, and the results are promising[27]. Further experiments await the commissioning of a Möbius lattice.

lattice. The motion of particles with initial coordinates outside the contours is not stable, so this plot shows that the dynamic aperture of off-energy particles is more restricted than that of on-energy particles. The large variation with energy is probably undesirable.

For comparison Figure 5.5 shows the results of a similar simulation for the final round beam lattice. In this case, the dynamic aperture is much larger and about the same for all particle energies. Since in practice the lifetime of both single and colliding bunches was good in that lattice, the goal of Möbius lattice design should be to achieve a lattice that has a qualitatively similar dynamic aperture.

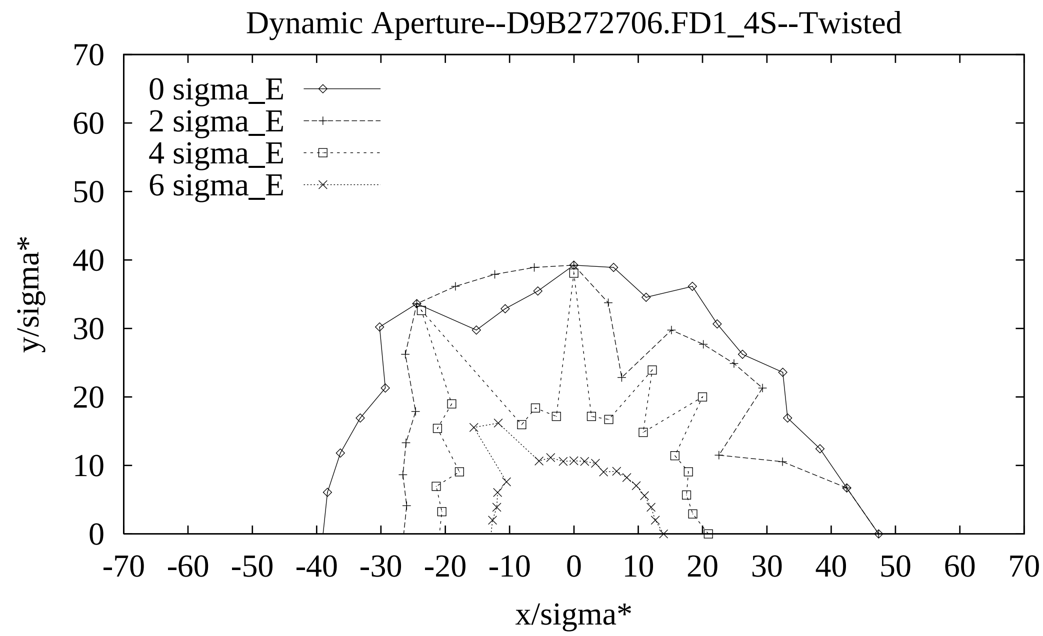

Figure 5.4: The dynamic aperture of the preliminary Möbius lattice, designated D9B272706.FD1_4S. The motion of particles with energy deviations of $0\sigma_E$, $2\sigma_E$, $4\sigma_E$, or $6\sigma_E$ and initial coordinates, $(x, y)_0$, outside the corresponding contours is not stable. Irregularities in the shape of the contours are due to the coarseness of the algorithm used to find the edge of the dynamic aperture, not to features of the lattice.

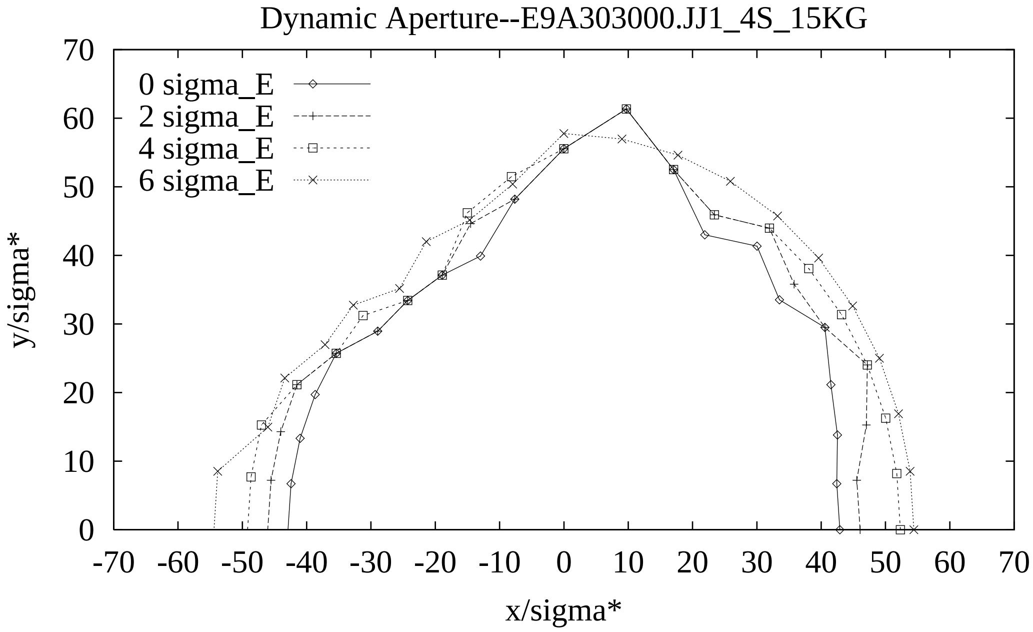

Figure 5.5: The dynamic aperture of the resonantly coupled round beam lattice, designated E9A303000.JJ1_4S_15KG. The motion of particles with energy deviations of $0\sigma_E$, $2\sigma_E$, $4\sigma_E$, or $6\sigma_E$ and $(x, y)_0$ outside the corresponding contours is not stable. Irregularities in the shape of the contours are due to the coarseness of the algorithm used to find the edge of the dynamic aperture, not to features of the lattice.

5.3 Injection

Prior to and during the commissioning of the round beam lattice, whether injection into a strongly coupled lattice was possible at all was questioned. Some sources claimed that in theory this would be problematic[23], while others claimed anecdotally that in practice, a little bit of coupling sometimes improved injection into CESR during normal operations.

Figures 5.6 through 5.9 illustrate the results of my simulation of the injection process using TEAPOT. To simulate injection, individual particles were launched at the injection septum with the pulsed kickers at their maximum value and tracked through the lattice. On each turn the strengths of the pulsed elements were decreased to simulate the effects of turning off the pulsed bump and sometimes the pinger was included as well. Using Equation 4.17 and the dimensions of the septa in CESR, the ideal initial coordinates for injected particles was estimated. If a particle survived for 1000 turns (about one damping time), it was declared stored. Figure 5.6 shows the trajectories for one such particle during its first four turns in lattice E9A242400.JJ1_4S. The pulsed bump is at its maximum amplitude on the first turn and is gradually turned off during the second and third turn, but the pinger was not used in this case. The width of the vacuum chamber is about 90 mm through most of the ring, so the amplitude of this injected particle takes up about half of that even after the pulsed bump is off. Using the pinger can reduce this, as can be seen by comparing the amplitudes of the injected particle's motion in Figure 5.6 with the amplitude of motion in Figure 5.7, which shows the first four turns of the same particle when the pinger fires on the first turn.

In both Figure 5.6 and 5.7, unusually large peaks are seen at two locations just over 500 m, corresponding to Q01 on either side of the IP (see Figure 5.2). This is

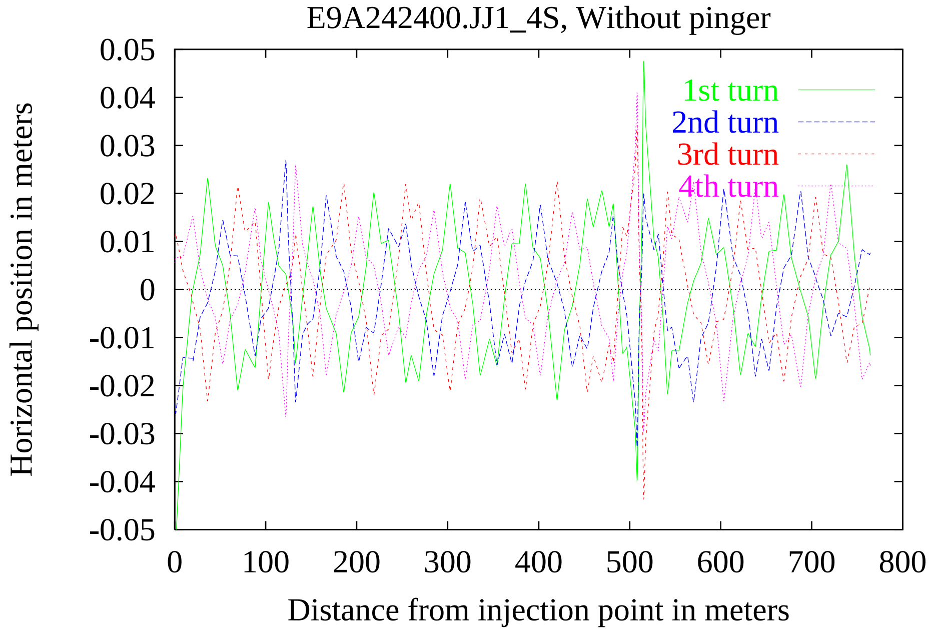

Figure 5.6: Simulation of injection into the original round beam lattice. The trajectory of a single injected particle during its first four turns is shown. During the first three turns, the pulsed bump is decreasing, and on the fourth turn all pulsed elements are turned off. The pinger was not used.

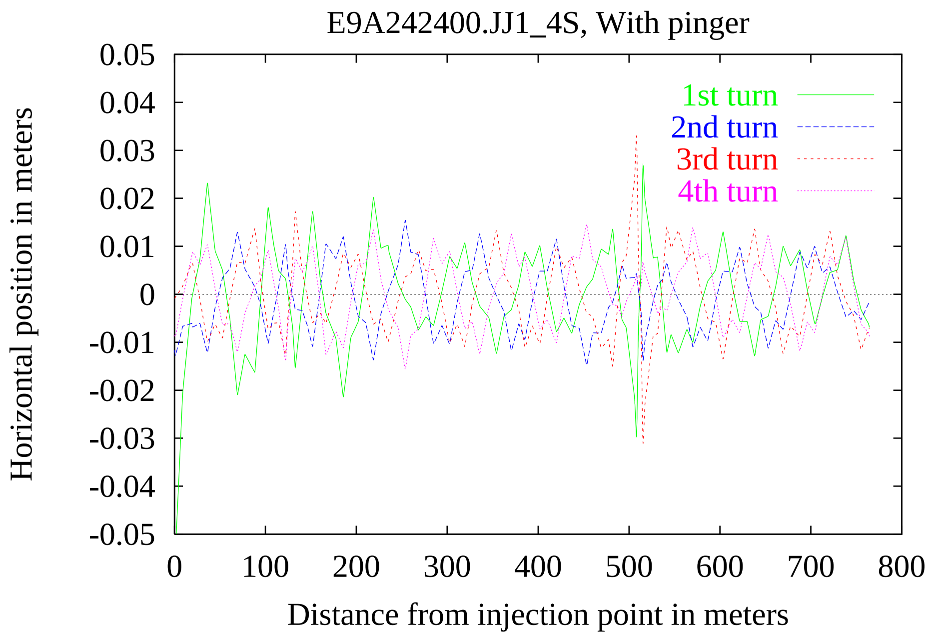

Figure 5.7: Simulation of injection into the original round beam lattice. The trajectory of a single injected particle during its first four turns is shown. The initial conditions for this particle were the same as for the particle shown in Figure 5.6, but this time the pinger was fired on the first turn.

due to the large value of β_x there. In most of CESR, $\beta_x < 40$ meters, but near Q01, the horizontal β-function reaches its maximum value, $\widehat{\beta}_x \simeq 200$ meters. When the original lattice was designed, it was thought that this particularly large value for $\widehat{\beta}_x$ (a result of changing the IP configuration from $\beta_y^* \ll \beta_x^*$ to $\beta_y^* = \beta_x^*$) would not pose a problem; however, it turned out to be extremely difficult to inject into the original round beam lattice. Particle losses during injection tended to occur near the IP, indicating that $\widehat{\beta}_x$ was the likely culprit.

When injection was possible, it was probably due in part to empirically adjusting the energy of the injected beam to take advantage of off-energy injection as described in Section 4.3, since $\eta_x \simeq 0,\ \eta_x' \simeq 0.0$ in the IR. Figure 5.8 shows a particle launched into the original lattice with the same initial coordinates as before, except that $\delta_{inj} = -0.0018$, which is about $3\sigma_\delta$. The amplitude of the betatron motion is perceptibly smaller than that in Figure 5.6 on all four turns, but not by much considering that $\delta_{inj} = 3\sigma_\delta$ is a large energy excursion. The benefits of off-energy injection are relatively small for this lattice because η_x at the injection point is not particularly large, $\eta_{inj} = 1.3$ m.

To improve injection, I designed a new round beam lattice with a smaller $\widehat{\beta}_x$ and a larger η_{inj}. The dispersion at the injection point was increased from 1.3 m to 3.3 m, and by increasing β^* from 24 cm to 30 cm, $\widehat{\beta}_x$ was reduced to 162 m. In addition, by the time this lattice was designed and commissioned, the lattice design software had been updated to include solenoid compensation as another variable to be optimized, so that the IR β's were not distorted by using an "insert" to compensate the CLEO-II solenoid, and an improved method of β correction had been adopted, so that in practice the β-functions of experimental lattice more closely matched the design. Figure 5.9 shows the first four turns of particle injected in to this final round beam lattice, E9A303000.JJ1_4S_15KG. The particle has approximately the same initial transverse coordinates as before and $\delta = -0.0018$. In this figure the beneficial effects of the pinger are particularly clear as well.

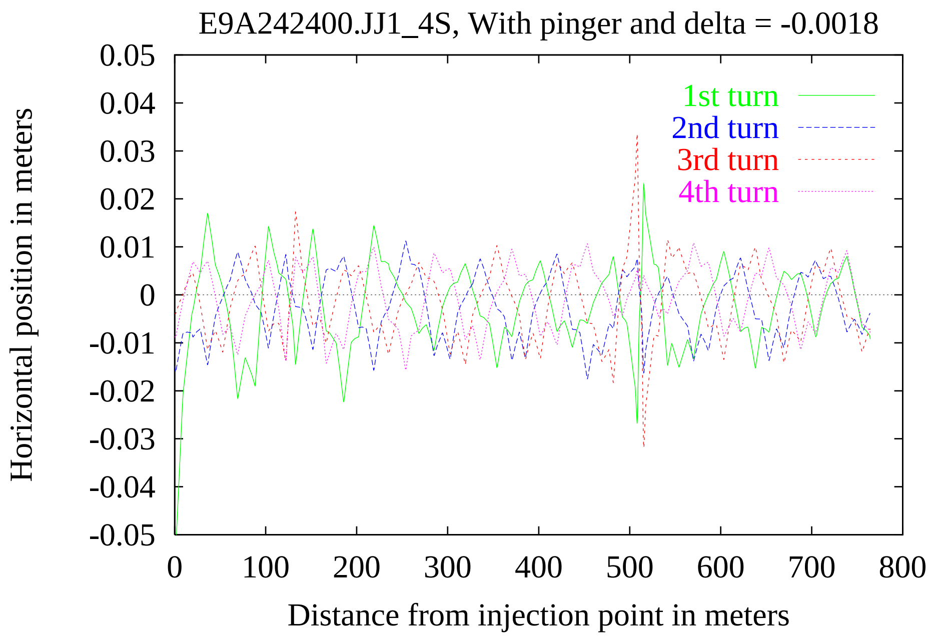

Figure 5.8: Simulation of off-energy injection into the original round beam lattice. The initial conditions for this particle were the same as for the particle shown in Figure 5.7 except that $\delta = -0.0018$. As before, during the first three turns, the pulsed bump is decreasing, and on the fourth turn all pulsed elements are turned off, and the pinger was fired on the first turn.

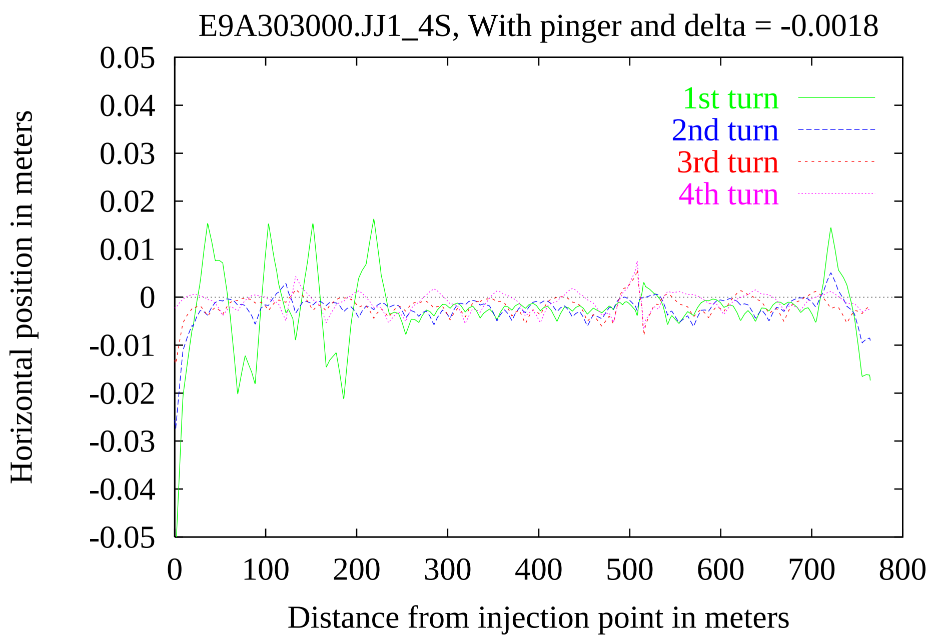

Figure 5.9: Simulation of off-energy injection into the improved round beam lattice. The initial coordinates for the particle shown here are similar to those of the particle shown in Figure 5.8, and $\delta = -0.0018$. (x_{inj} and x'_{inj} are not exactly the same since the β-functions at the injection septa are slightly different in the improved lattice.) As before, during the first three turns, the pulsed bump is decreasing, and on the fourth turn all pulsed elements are turned off, and the pinger was fired on the first turn.

5.4 Beam-Beam Simulations

Simulations have proven useful for modeling the beam-beam interaction. Since most colliders have been flat beam machines, most of the past simulations have also used flat beams, and the results of a few of these will be summarized here before discussing round beam simulations done by my colleagues in connection with the round beam and Möbius experiments.

Many beam-beam simulations have been in the weak-strong regime; that is, the distribution of the strong beam is held fixed while particles in the weak beam are tracked, and $\xi_{strong} > \xi_{weak}$. This has the advantage of simplifying the simulation, but eliminates the possibility of studying coherent effects. One weak-strong simulation of CESR[28] was directed toward understanding factors leading to luminosity limitations at CESR, and the results of that simulation indicated that the proximity of the $2Q_x - 2Q_y = Q_s$ synchro-betatron resonance was a significant factor in beam blowup for the operating point at that time. Strong-strong simulations have provided insights into mechanisms for beam size blowup due to the beam-beam interaction[29, 30]. In a strong-strong simulation, both beam distributions are allowed to evolve. The results of one strong-strong simulation of CESR, which matched experimental data well, suggested that parametrically driven beam-beam resonances are responsible for beam blowup[29]. An independent simulation pointed to beam-beam driven parametric and coupling resonances seen by individual particles, rather than coherent effects, as the primary culprits[30]. In any case, round beams seem to be resistant to these effects, and strong-strong simulations of round beams indicated that $\xi > 0.1$ are possible[1, 2].

To simulate beams in a storage ring, the beam is often described by a number of "macroparticles"; *i.e.* rather than track 10^{11} particles, 100 or so representative particles are tracked through the magnetic and electrostatic elements in the storage ring. For single beam simulations, the initial coordinates of the macroparticles can be Monte Carlo generated with a Gaussian distribution. For a weak-strong simulation, the effect of the beam-beam force on the weak beam macroparticles due to the strong beam particle distribution can be calculated from a static Gaussian since the weak beam is assumed not to perturb the strong beam. However, for a strong-strong simulation, the analytic distribution representing the beam-beam force must be allowed to evolve in order to remain consistent with the distribution of macroparticles. A flow diagram of a typical simulation[31] is shown in Figure 5.10. The input parameters of the first step in the diagram might include such items as the parameters of the initial distribution, the damping coefficient, and a description of the transport through the storage ring. Next, a bunch of macroparticles, say 100, is Monte Carlo generated using the relevant input parameters. These particles are then tracked for 1000 turns (about one damping time in CESR) during which time the beam-beam deflection is calculated using the analytic distribution. After 1000 turns, the parameters of the analytic distribution are updated to match the profile of the bunch of macroparticles. This cycle is repeated several times until self-consistency is reached.

The discussion of beam-beam phenomena in Chapter 2 assumed a round Gaussian particle distribution, which depends on a single parameter, σ, and which is also known as a Rayleigh distribution. When expressed in terms of $r = \sqrt{x^2 + y^2}$, the Gaussian distribution is

$$P_x(x;\sigma) = \frac{1}{\sqrt{2\pi}\sigma} \exp\left(-\frac{x^2}{2\sigma^2}\right), \quad {\sigma_x}^2 = \int_{-\infty}^{\infty} x^2 P_x(x;\sigma)dx = \sigma^2, \tag{5.2a}$$

$$P_y(y;\sigma) = \frac{1}{\sqrt{2\pi}\sigma} \exp\left(-\frac{y^2}{2\sigma^2}\right), \quad {\sigma_y}^2 = \int_{-\infty}^{\infty} y^2 P_y(y;\sigma)dy = \sigma^2, \tag{5.2b}$$

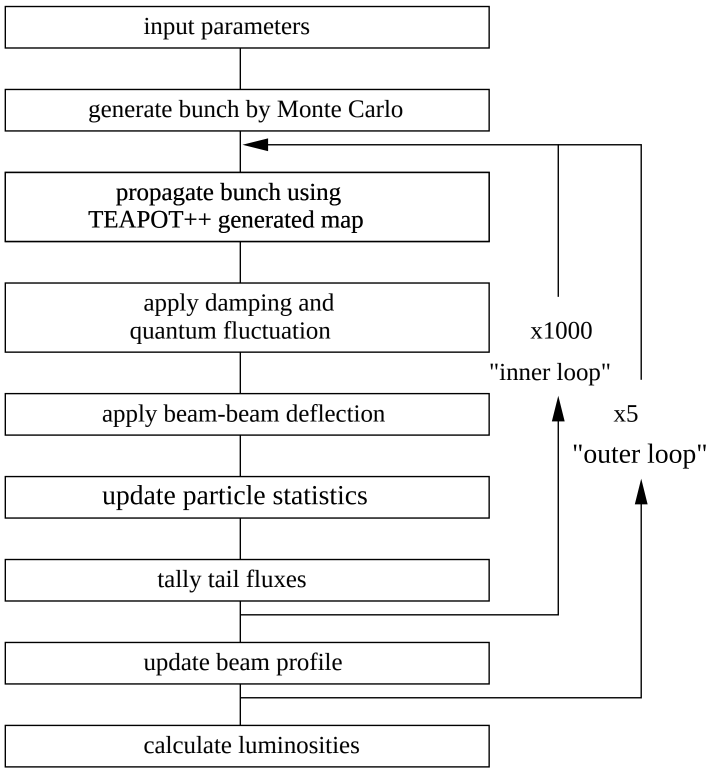

Figure 5.10: A flow diagram of a typical strong-strong simulation[31].

$$P_r(r;\sigma) = \frac{r}{\sigma^2}\exp\left(-\frac{r^2}{2\sigma^2}\right), \quad {\sigma_r}^2 = \int_0^\infty r^2 P_r(r;\sigma)dr = 2\sigma^2, \tag{5.2c}$$

$$C_r(r) = \int_0^r P_r(r';\sigma)dr' = 1 - \exp\left(-\frac{r^2}{2\sigma^2}\right), \tag{5.2d}$$

where $C_r(r)$ is the cumulative probability distribution of r. The low order moments of this distribution are

$$\begin{gathered} \langle r^0\rangle = 1, \qquad \langle r^1\rangle = \sqrt{\tfrac{\pi}{2}}\sigma, \qquad \langle r^2\rangle = 2\sigma^2, \\ \langle r^3\rangle = 3\sqrt{\tfrac{\pi}{2}}\sigma^3, \qquad \langle r^4\rangle = 8\sigma^4. \end{gathered} \tag{5.3}$$

The discussion in Chapter 2 also assumed that the particle distributions remain Gaussian during collisions, but in general this may not be the case. Beam-beam deflections are expected to cause the beam profile to grow a "tail" extending to large r, while the "core" of the distribution remains approximately Gaussian. A distribution that has an extra parameter and is hence capable of having these properties is the "near-Rayleigh" distribution,

$$P_r(r;\sigma,p) = \frac{p}{2^{2/p}\sigma^2\Gamma(2/p)} r \exp\left[-\frac{1}{2}\left(\frac{r}{\sigma}\right)^p\right], \tag{5.4}$$

and its low order moments are

$$\begin{aligned} \langle r^0\rangle &= 1, & \langle r^1\rangle &= 2^{1/p}\sigma\frac{\Gamma(3/p)}{\Gamma(2/p)}, \\ \langle r^2\rangle &= 2^{2/p}\sigma^2\frac{\Gamma(4/p)}{\Gamma(2/p)}, & \langle r^3\rangle &= 2^{3/p}\sigma^3\frac{\Gamma(5/p)}{\Gamma(2/p)}. \end{aligned} \tag{5.5}$$

Since the cumulative probability distribution, $C_r(r)$, cannot be written in terms of elementary functions, it is most convenient to interpolate in a table obtained by numerical integration.

Figure 5.11 shows some results of a beam-beam simulation done by one of my colleagues using an initially round Gaussian distribution[31]. The beam size, σ, and the parameter p for the final near-Rayleigh distribution are plotted as a function of the beam current. As the current increases, the beam size increases, and the distribution does not deviate significantly from Gaussian ($p = 2$ corresponds to a Gaussian distribution.), which is encouraging.

Similar simulations were used to choose the ideal tune for the resonantly coupled lattice[32]. Simulated luminosity and the beam-beam tune shift parameter, ξ, are plotted vs. average tune in Figure 5.12. In this simulation the current per bunch was 20 mA, and $\beta^* = 0.1$ meters. Although tunes near the integer and half integer produce higher luminosity in this simulation, $\overline{Q} = 0.77$ was chosen because it also corresponded to a peak in $\mathcal{L}$ vs. Q for a similar Möbius lattice, since one of the goals of the resonantly coupled round beam experiment was to provide a baseline for comparison with future Möbius experiment that would presumably be done at the optimum Möbius tune.

Simulations that included the beam-beam interaction were also used to predict the expected luminosity for resonantly coupled round beams with $Q_x = Q_y = 0.77$ and $\beta^* = 0.30$ meter[33], as shown in Figure 5.13.

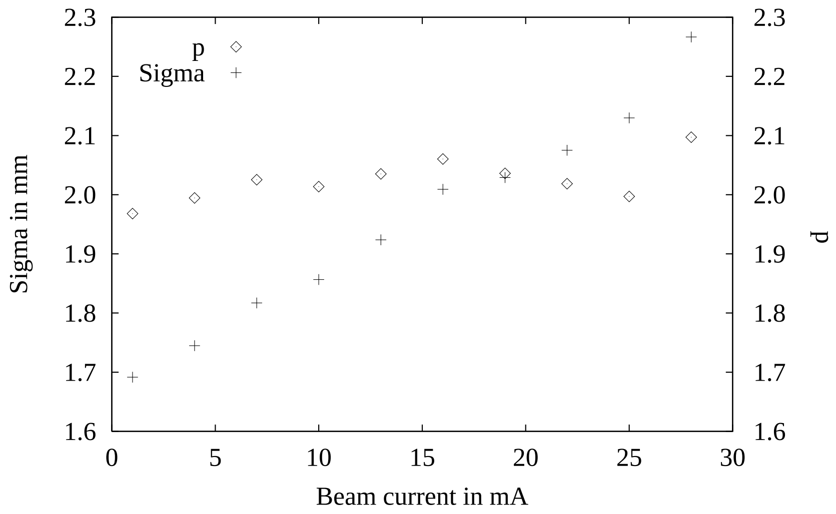

Figure 5.11: Beam size, σ, and the parameter p of a near-Rayleigh distribution of particles in a beam-beam simulation as function of beam current.

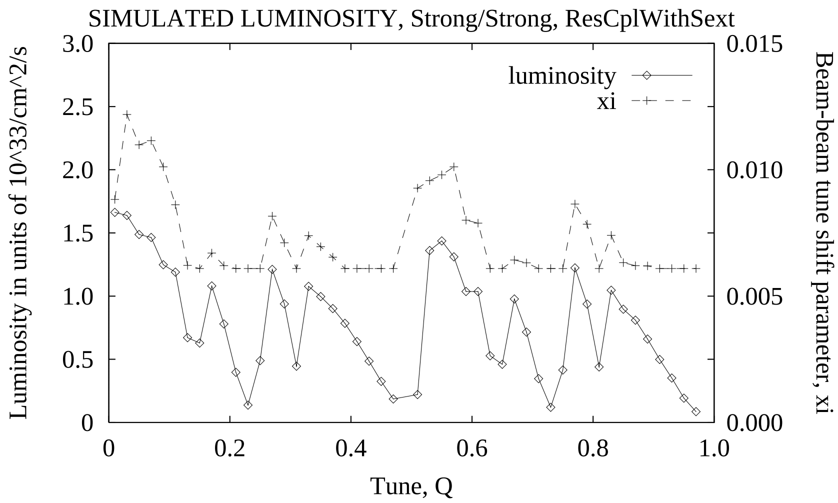

Figure 5.12: Simulated luminosity and beam-beam tune shift parameter, ξ, as a function of tune for round beams.

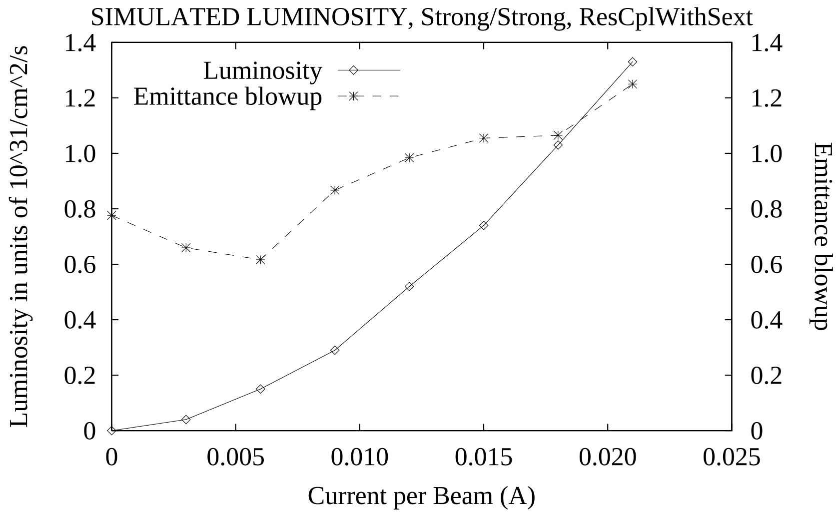

Figure 5.13: Simulated luminosity and beam size blowup as a function of beam current for the resonantly coupled round beam lattice, E9A303000.JJ1_4S_15KG. Emittance blowup is the square of the beam size blowup.

Chapter 6
Measurement Methods and Results

6.1 Introduction

As stated in Chapter 1, because hardware limits restricted the round beam lattice to a relatively large β-function at the interaction point ($\beta^* = 30$ m), large luminosity was not possible during these experiments, so the emphasis was on the linear beam-beam tune shift parameter, ξ, which is independent of β^* for round beams, along with the beam size blowup, which ultimately limits ξ, and the coherent π mode tune shift. In this chapter the methods of measuring these quantities are described, and the results of those measurements are presented. In addition, during the final two runs[1], the luminosity was measured to verify the current and emittance measurements.

6.2 Beam Profile

As charged particles are accelerated, they emit radiation. The light emitted by electrons and positrons in CESR in the visible range can be used to non-destructively

[1]A "run" consists of one cycle of injecting and colliding the beam, possibly including some adjustment of the tunes and other parameters to optimize the collision.

monitor the profile of the beams. Two charge coupled device (CCD) profile monitors exist in CESR for the purpose of monitoring the vertical beam size, one for each beam. The emittance can then be calculated from $\varepsilon_y = \sigma_y^2/\beta_y$. No horizontal profile monitors are available. The horizontal and vertical emittances are assumed to be equal due to the substantial coupling.

6.2.1 Linear CCD Array and COMET$^{\text{TM}}$ Digitizer

The CCD used is a linear array of 1728 photodiodes (pixels) with center-to-center spacing of 12.7 μm. The overall magnification of the optical system that guides and focuses the image on the CCD as reported in 1990 is 0.85[34]; the actual value may have changed in the intervening years, as is discussed in the next section. An input diode injects charge into the end two pixels of the array to provide a reference signal that is used by automatic gain control (AGC) circuitry. The AGC circuit varies the interval between exposure control pulses to prevent the CCD from saturating. Since the round beams were considerably larger vertically, and thus more diffuse, than typical flat beams in CESR, and since there was only one bunch per beam, often the longest possible time interval was used. However, sometimes even this was not long enough to produce a good signal, as seen in Figure 6.1, which is the profile of a 2 mA positron bunch that was colliding with a 12 mA electron bunch. That profile should be contrasted with Figure 6.2, recorded on the same day but for a different run in which the positron current was larger and the electron current was lower.

There are two primary sources of background for the CCD signal, dark current due to thermal effects and reflections of synchrotron light from the walls of the vacuum chamber and parts of the optics. In addition, presumably due

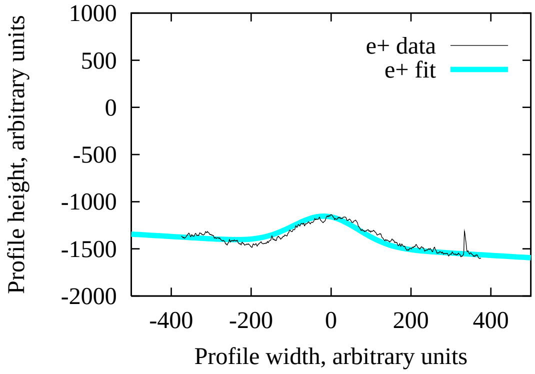

Figure 6.1: An example of the digitized beam profile of a low current, blown up beam (see CCD profile #78 in Appendix B). In the digitizer units, $\sigma = 81.7$, which corresponds to $\varepsilon = 135.4$ nm-rad.

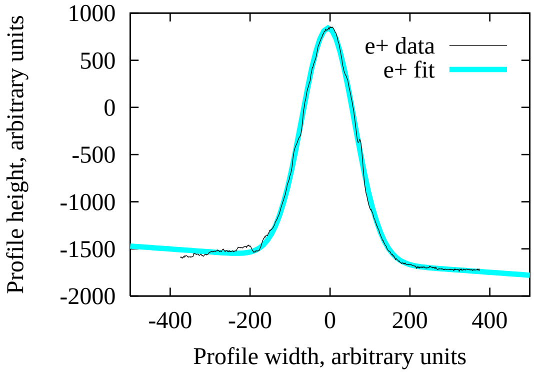

Figure 6.2: An example of the digitized beam profile and the Gaussian fitted to it (see CCD profile #51 in Appendix B). In the digitizer units, $\sigma = 58.2$, which corresponds to $\varepsilon = 68.6$ nm-rad.

to radiation damage, some pixels no longer respond linearly with light intensity. The dark current problem was exacerbated by the long exposure times typically required. The signal was maximized by adjusting the horizontal tilt of the synchrotron light mirror. The background was observed to be approximately linear and was removed by fitting the profile to a Gaussian plus a linear function, $y(x) = b + mx + a\exp[-(x-x_0)^2/2\sigma^2]$. The position of the image on the CCD array could be changed by adjusting the vertical angle of the synchrotron light mirror, striking a balance between minimizing the number of "bad" pixels in the core of the profile and minimizing the effects of reflections.

The output of each of the CCD light monitors was fed to a COMET$^{\mathrm{TM}}$ VME multichannel analog digitizer board, which is manufactured by Omnibyte Corporation[35]. The COMET$^{\mathrm{TM}}$ board provides, among other features, four independent, 12 bit analog-to-digital converters with on-board RAM for 64,000 samples per channel. For recording the beam profiles, the COMET$^{\mathrm{TM}}$ board was operated in the "circular buffer mode." In this mode the input to each channel is continuously digitized and written to RAM until a trigger, from software in this case, is received. If the end of the buffer is reached, storage "wraps around" to the beginning of the RAM, overwriting any previously digitized data. The sampling rate was set to the internal clock rate of 1 MHz. In addition, an external gate (an "or" logic gate) was supplied so that the digitizer was not in fact digitizing continuously, but was active only when one or the other CCD was being read out. After the software trigger is received, the most recent peaks in the RAM data, of sufficient height and width to be the profiles, are written to a file along with bunch currents and the frequencies of peaks in the beam spectrum. A second software trigger signals the digitizer to resume circular buffer mode.

The profiles were fit to the function $y(x) = b + mx + a\exp[-(x-x_0)^2/2\sigma^2]$. For most of the data, this was done off line using Mathematica. Figures 6.1 and 6.2 show profiles and the resulting fits. Some profiles were fit on line using a routine written in IDL by Stuart Henderson. The beam profiles, the conditions under which they were recorded, and the measured emittances are cataloged in Appendix B.

6.2.2 Measuring ε_0 with Scrapers

Inferring the absolute vertical emittance, $\varepsilon_y = \sigma_y^2/\beta_y$, requires knowledge of both the β-function at the source point of the synchrotron light and a conversion factor between COMET samples and actual beam size, which includes an optical magnification factor for the synchrotron light monitor. Although a value exists for the magnification factor[34], nearly a decade has passed since it was measured, so it is not certain that this value is correct or even the same for both the positron and electron monitors as modifications to both sets of optics may have occurred in the intervening years.[2] To calibrate and correct the magnification factor, the size of a single beam was inferred by restricting the vertical aperture with movable scrapers[14, 37] and comparing the beam size inferred this way with the CCD beam profile measurement. It is assumed that calibration factors are the same when the beams are in collision.

In normalized phase space coordinates, (r, θ), rather than (y, y'), the number of particles having oscillation amplitudes less than or equal to r is

$$N(r) = N_0 \int_0^r F(r')r'dr', \tag{6.1}$$

[2]Recently, a two dimensional CCD array and a fiber array were installed to observe synchrotron light from the electrons[36]. There is also a video camera for each set of optics so that changes in the beam profiles can be observed visually in the control room, so the synchrotron light must be split three times. The one dimensional CCD array was at the end of the chain so the amount of light incident on it was significantly reduced.

where N_0 is the number of particles in the beam, and $F(r)$ is the distribution function of particles in the beam. If the flux of particles moving toward the center of the beam at r is due nearly entirely to radiation damping, then that flux is equal to the number of particles changing amplitude at r times the rate of change of oscillation amplitude,

$$\Phi_{\text{in}}(r) = \left(\frac{dN}{dr}\right)\left(\frac{dr}{dt}\right) = N_0 F(r) r \left(-\frac{r}{\tau_d}\right), \tag{6.2}$$

where τ_d is the radiation damping time. If a scraper is inserted into the aperture to distance r from the center of the beam, the loss rate of particles from the beam, or beam lifetime τ, is equal to the outward flux, and in stable equilibrium, the magnitude of the outward flux of particles should equal the magnitude of the inward flux, so

$$\begin{aligned} \frac{1}{\tau} &= \frac{dN_0}{dt} = \Phi_{\text{out}} = -\Phi_{\text{in}} \\ &= \frac{N_0}{\tau_d} F(r) r^2. \end{aligned} \tag{6.3}$$

Rewriting this in terms of the vertical position of the scraper relative to the center of the beam,

$$\tau = \frac{\tau_d \sigma_y^2}{y^2} \exp(y^2/2\sigma_y^2). \tag{6.4}$$

Figure 6.3 shows a plot of τ vs. scraper position. The inset shows a close-up of the curves for three different damping times, $\tau_d = 15$, 20, and 25 msec. There is some uncertainty about the damping time for the round beam lattice. During chromaticity sharing experiments, $\tau_d \approx 22$ msec seemed to be typical of the uncoupled lattice, but with coupling under various conditions, $\tau_d \approx 8$ to 32 msec, and there was a definite difference between the damping times for the two modes. However, from Equation 6.4, a 25% variation in the damping time ($\tau_d = 20 \pm 5$ msec) re-

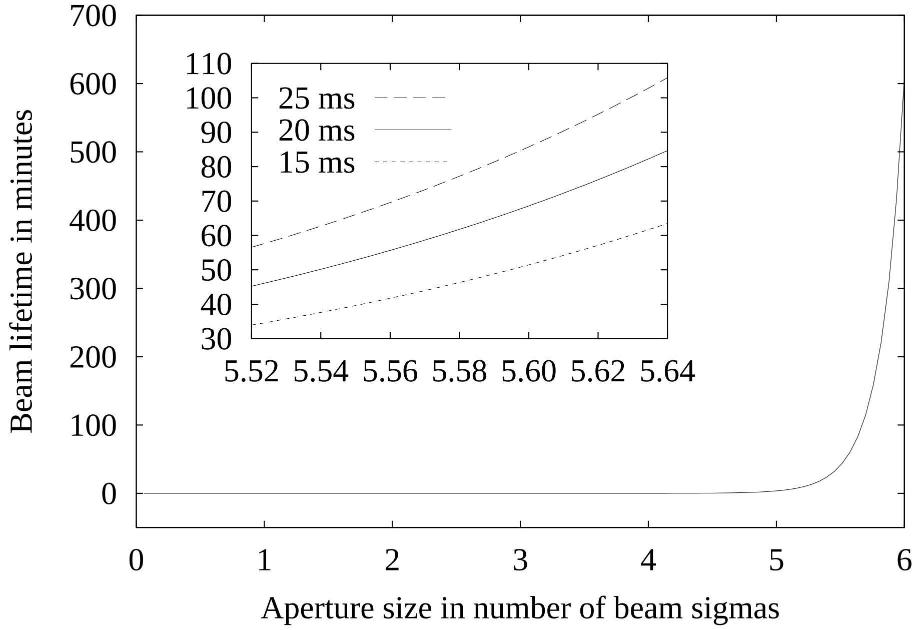

Figure 6.3: Beam lifetime as a function of aperture (or scraper position) in units of beam σ. The inset focuses on a particular range of apertures for a range of radiation damping times. The dashed line corresponds to $\tau_d = 25$ msec, the solid line corresponds to $\tau_d = 20$ msec, and the dotted line corresponds to $\tau_d = 15$ msec. For $\tau_d = 20$ msec, when the scraper aperture is 5.58 σ, the beam lifetime is about 60 minutes.

sults in only a 1% variation in beam size ($y = (5.58 \pm 0.05)\sigma_y$) corresponding to a particular beam lifetime ($\tau = 60$ sec).

Vertical scrapers at 43W and 43E (just to the south of the northern pair of horizontal separators; see Figure 4.4) were used to infer the vertical beam size of each beam. At the same time, profiles of each beam were recorded using the CCD array. The scrapers are calibrated such that their position was known. Due to the limited range of movement of the scraper, it became necessary to use a closed bump to move the beam close enough to the scraper to reduce the lifetime to approximately 60 minutes. The bump was calibrated by taking the difference between the orbits with and without the bump. Since it was not possible to bring the beam lifetime to exactly 60 min every time, some uncertainty is introduced, and it is of about the same size as the uncertainty of the damping time, about 1%. When the lattice was commissioned, the β-functions were corrected to match the theoretical lattice to about 5%. The uncertainty of the fitted σ's for the CCD profiles is estimated to be about 5%.

The average positron emittance as inferred from the CCD profile was 50.6 nm-rad, whereas the average electron emittance was 60.6 nm-rad; however, the emittance inferred from the scraper measurements was the same for both beams, so the emittances were rescaled to the average of the CCD measurements, 55.6 nm-rad. In all figures in this chapter, the emittances plotted are the rescaled emittances.

6.2.3 Emittance Blowup

During the round beam collision experiments, emittance blowup was measured as a function of the tune along the coupling resonance to verify that $\overline{Q} = 0.77$ was the optimal tune in the region of tune space above 0.75, as predicted by simulation (see Figure 5.12). The tune scans were done with weak-strong collisions to enhance the blowup of the weaker beam and were repeated at three different strong beam currents. The emittance blowup of each beam, $b_\pm = \varepsilon_\pm/\varepsilon_0$, is plotted against the average of the normal mode tunes, $\overline{Q} = (Q_A + Q_B)/2$, in Figures 6.4 through 6.6. There is evidence of a resonance near $\overline{Q} = 0.80$ and also at $\overline{Q} = 0.83$. No tune scans were done during strong/strong collisions, and at high currents, beam losses usually occurred if the tune was raised even a small amount. Also, at high currents the colliding beams seemed to “prefer” $\overline{Q}$ closer to the three-quarters resonance, even though that is an unstable resonance. The reason for this is unknown and deserves further investigation.

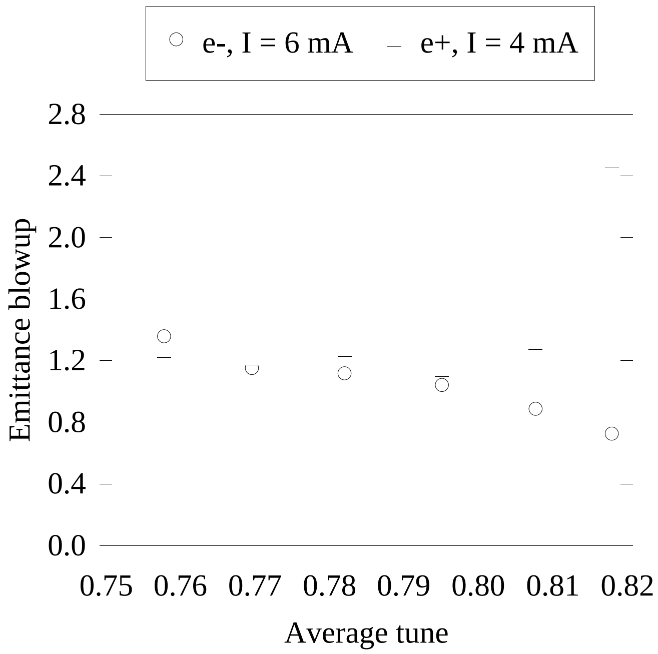

Figure 6.4: Emittance blowup, $b_{\pm}$, of each beam as a function of the average tune, $\overline{Q} = (Q_A + Q_B)/2$. $I_{-} \simeq 6$ mA, $I_{+} \simeq 4$ mA are the approximate initial currents. These data points correspond to CCD profiles #60–65 (see Appendix B). The lifetime of the weak beam decreased near $\overline{Q} = 0.80$. When an attempt was made to raise the tune to $\overline{Q} = 0.83$, the weak beam became too diffuse to be seen on the CCD, and the beams seemed to become "locked" into this state. The tunes had to be lowered to $\overline{Q} < 0.80$ before the beam sizes returned to normal.

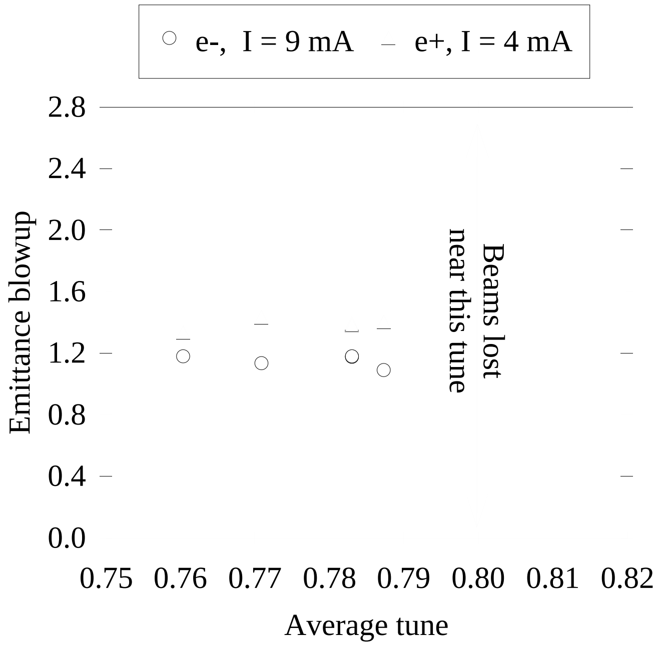

Figure 6.5: Emittance blowup, $b_{\pm}$, of each beam as a function of the average tune, $\overline{Q} = (Q_A + Q_B)/2$. $I_{-} \simeq 9$ mA, $I_{+} \simeq 4$ mA are the approximate initial currents. These data points correspond to CCD profiles #70–74 (see Appendix B). The lifetimes of both beams were good until $\overline{Q} \simeq 0.80$ was attempted, at which time the positron lifetime become poor, so that measurement was done at $\overline{Q} = 0.79$ instead. An attempt was made to hop over the "resonance," but all positrons were lost in the process.

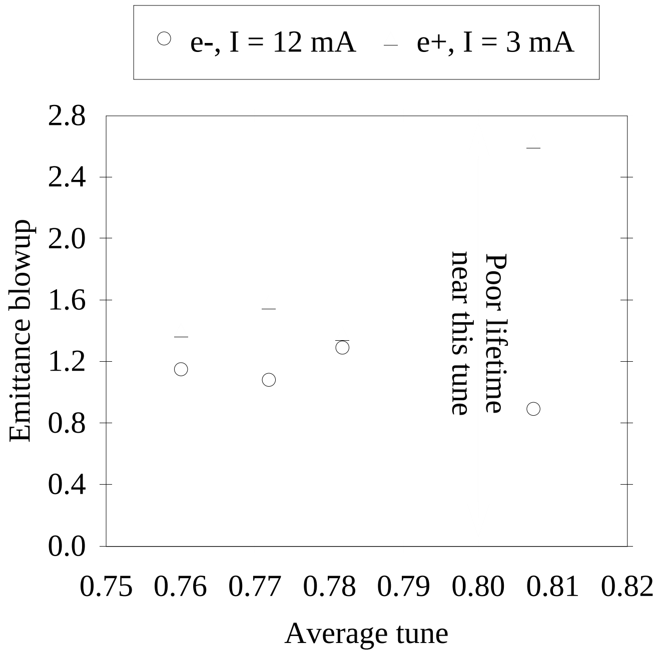

Figure 6.6: Emittance blowup, $b_{\pm}$, of each beam as a function of the average tune, $\overline{Q} = (Q_A + Q_B)/2$. $I_- \simeq 12$ mA, $I_+ \simeq 3$ mA were the approximate initial currents. These data points correspond to CCD profiles #75–78 (see Appendix B). The edge of the region of poor lifetime was at $\overline{Q} = 0.78$, so two data points had to be skipped. Some positron loss was incurred in attempting to hop the region of bad lifetime. For $\overline{Q} > 0.81$, the positron profile was so diffuse that it disappeared into the noise background of the CCD.

6.3 The Beam-Beam Tune Shift Parameter

Since the beams did not necessarily have exactly the same current, and since they rarely had equal beam sizes, the beam-beam force "experienced" by each beam was not the same. The beam-beam tune shift parameter, $\xi_\pm$, experienced by each beam was calculated from the measured emittance and current using Equation 2.22. Recall that the subscript on ξ in this context refers to the affected beam. For example, ξ_+ is the strength of the beam-beam forces experienced by the *positrons*, so it is calculated from the *electron* beam size and current. The emittance blowup of each beam as a function of the tune shift parameter to which they were subjected, $\xi_\pm$, are plotted in Figure 6.7, and $\xi_\pm$ vs. the current per beam are plotted in Figure 6.8. Despite the fact that most of these data points were recorded at nearly equal electron and positron currents, the electrons are consistently blown up more than the positrons, a tendency also observed during normal flat beam operation of CESR. Figure 6.7 includes only data points for which the coherent π mode was also observed and recorded. The correlation between ξ_+ and ξ_- is plotted in Figure 6.9, and the currents and emittances used to calculate $\xi_\pm$ are tabulated in Appendix B.

If the tune shift parameter were saturated, one would expect the data points in Figure 6.7 to approach a vertical line. In other words, above the saturation point, attempting to increase ξ by increasing the current per bunch is futile – the beam size blows up, and ξ remains constant. In addition, after saturation ξ vs. I would lie along a horizontal line. There is no indication of this behavior in either Figure 6.7 or Figure 6.8. Also, as $\xi_- \to 0.09$, it became progressively more difficult to bring the beams into collision without loss; however, once in collision the beam lifetimes did not differ significantly from the pre-collision lifetimes, indicating that the tails of the beam distributions are not being populated.

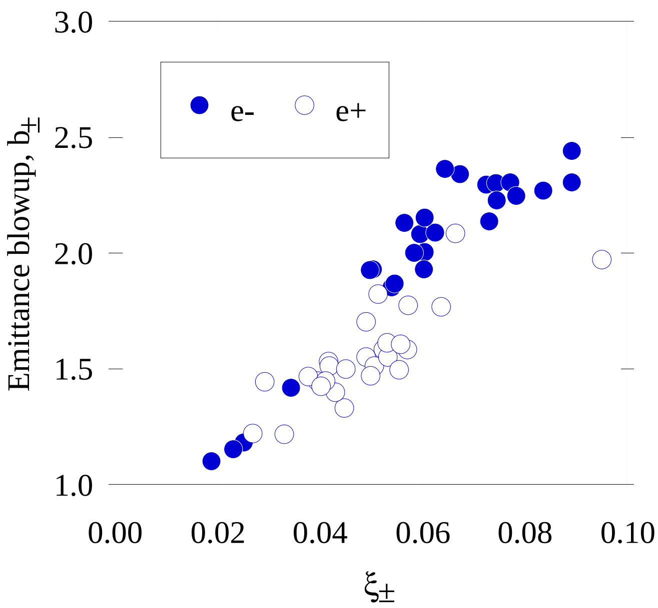

Figure 6.7: The emittance blowup of each beam, $b_{\pm}$ as a function of the tune shift parameter which it experienced, $\xi_{\pm}$. Only data points for which the coherent π mode was also observed and recorded are included, and they correspond to CCD profiles #50, 51, 60, 101, 106, 107, 109, 110, 113–121, 150–155, and 157–160. In most cases, $I_+ \simeq I_-$. If the tune shift were saturated, the data points would approach a vertical line. No tune shift saturation is evident.

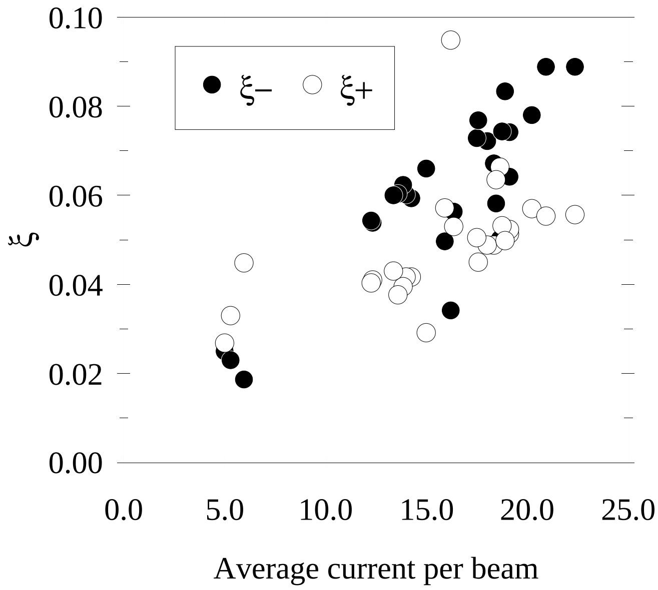

Figure 6.8: The tune shift parameter experience by each beam, $\xi_{\pm}$, vs. the average current per beam. In most cases, $I_+ \simeq I_-$. This is the same set of data as was plotted in Figure 6.7. If the tune shift were saturated, ξ would be constant with current. No tune shift saturation is evident.

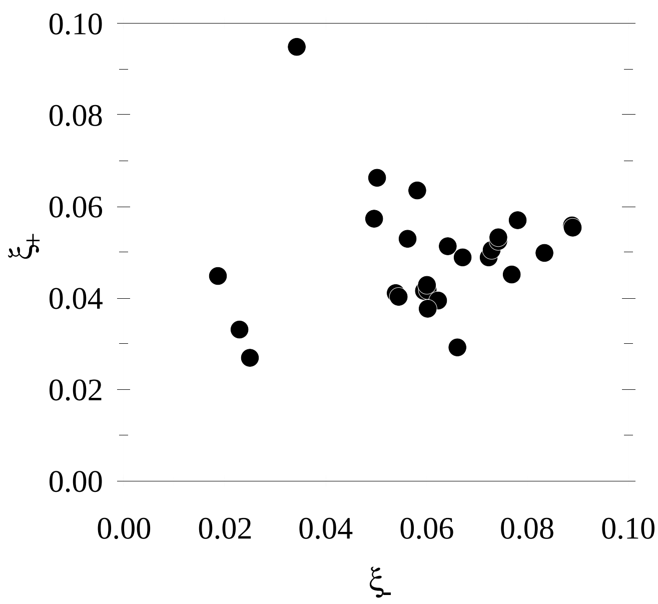

Figure 6.9: The tune shift parameter experienced by the positrons, ξ_+, vs. the tune shift parameter experienced by the electrons, ξ_-. This is the same set of data as was plotted in Figure 6.7. As this plot shows, even though the currents were nearly the same in most cases, ξ_- tends to be larger than ξ_+. This tendency is also seen during normal flat beam operation of CESR, which corresponds to the electron emittance being more blown up than the positron emittance.

6.4 Beam-Beam Coherent Oscillation Modes

The coherent mode frequencies were monitored by a spectrum analyzer connected to pickup electrodes. There are two sets of pickups in CESR, one oriented to observe horizontal motion and one oriented to observe vertical motion. Since the motion of the beams was strongly coupled during these experiments, both mode A and mode B (as discussed in Chapter 3) were visible in both spectra, and both modes have approximately the same amplitude, as seen in Figure 6.10. During collisions, the beam-beam interaction may induce coherent π mode motion corresponding to each single beam mode, in which case four peaks are expected in the spectrum, and in fact all four modes were easily identifiable in the colliding round beam spectra in most cases. An example is shown in Figure 6.11. The colliding beam profiles, the conditions under which they were recorded, and $\overline{\Delta Q_\pi}$ for each one are cataloged in Appendix B.

During most runs the π mode shift was slightly different for the two coupled modes; this probably indicates that the beams were slightly out of round. For comparing ΔQ_π with ξ, the average of the two tune splits, $\overline{\Delta Q_\pi} = (\Delta Q_{\pi_A} + \Delta Q_{\pi_B})/2$, was used. Figure 6.12 shows the colliding beam spectrum with the largest observed tune split that we succeeded in obtaining, $\overline{\Delta Q_\pi} = 0.098$ at a current per bunch of $I = 21$ mA. Yokoya and Koiso's model[10] implies that this tune shift corresponds to $\xi = 0.074$, nearly twice ξ_y^{max} achieved during normal flat beam operation of CESR. Since in most cases $\xi_+ \neq \xi_-$, ΔQ_π should be compared to the species average, $\xi_{avg} = (\xi_+ + \xi_-)/2$, where $\xi_\pm$ are obtained from the measured bunch currents and emittances using Equation 2.22. The maximum ξ_{avg} was 0.072, also at $I = 21$ mA.

For each run the observed average tune shift, $\overline{\Delta Q_\pi}$, was compared to ξ_{avg}, and

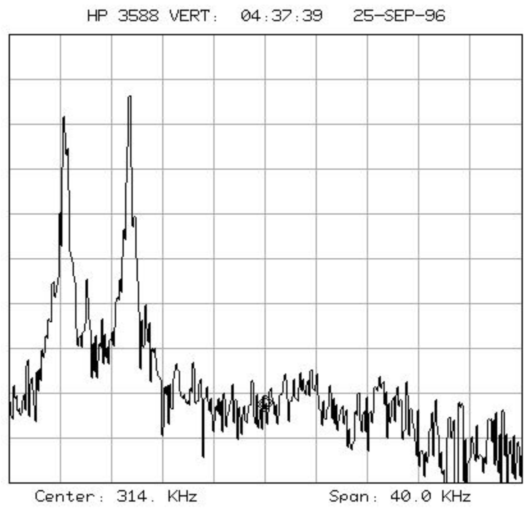

Figure 6.10: Spectrum of a single coupled beam showing both normal mode tunes, Q_A and Q_B. Which peak is Q_A and which peak is Q_B is essentially arbitrary.

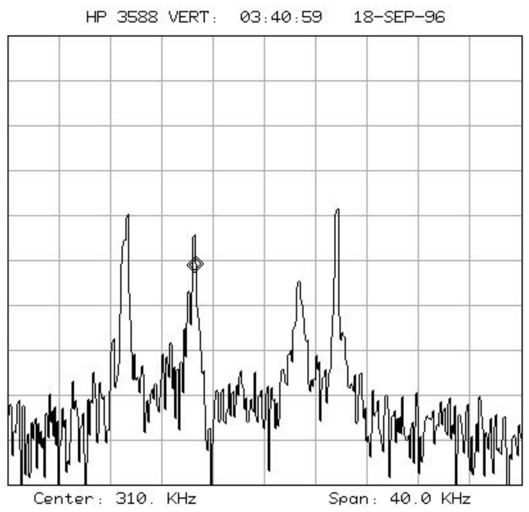

Figure 6.11: Spectrum of colliding coupled beams showing four coherent modes. The two peaks on the left are the σ modes, Q_A and Q_B, which are the same as the single beam modes shown in Figure 6.10. The two peaks on the right are the corresponding coherent π modes.

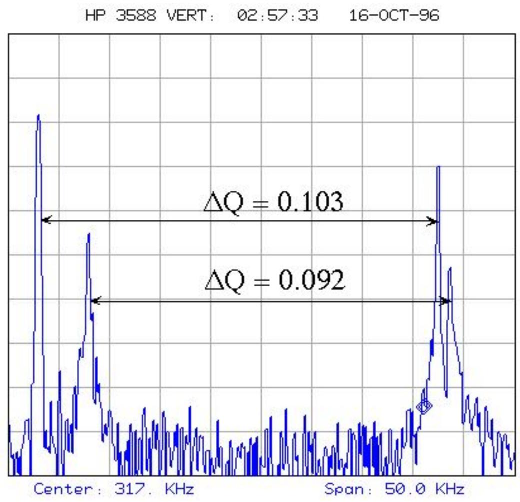

Figure 6.12: Spectrum of colliding beams showing the maximum observed tune split, $\overline{\Delta Q_\pi} = 0.098$, $\overline{\Delta Q_\pi} = (\Delta Q_{\pi_A} + \Delta Q_{\pi_B})/2$. During most runs the coherent π mode tune shifts for each mode were slightly different.

a value of the derating factor, λ, was calculated using Equation 2.39. The average value of the derating factor was $\lambda = 1.28 \pm 0.07$; this data is shown in Figure 6.13. As discussed in Chapter 2, Yokoya and Koiso[10] calculated the derating factor, λ, for a range of beam size ratios, assuming $\varepsilon_+ = \varepsilon_-$, both for the case $\xi_+ = \xi_-$ and $\xi_+ \neq \xi_-$. For the latter, they repeated the calculation for various ratios ξ_+/ξ_-. For round beams with $\varepsilon_+ = \varepsilon_-$ and $\xi_+ = \xi_-$, they calculate $\lambda = 1.21$, and for $\xi_+/\xi_- \simeq 2$, $\lambda = 1.28$. Using Equation 2.39, $\lambda = 1.28 \pm 0.07$ fits the measured ξ_{avg} and $\overline{\Delta Q_\pi}$. For most of the data points both $\varepsilon_+ \neq \varepsilon_-$ and $\xi_+ \neq \xi_-$. The theoretical calculation has not been done for this case; however, since λ changes slowly with ξ_+/ξ_- in Yokoya and Koiso's model, it is reasonable to assume that it also changes slowly with $\varepsilon_+/\varepsilon_-$, so to the accuracy with which ξ and ΔQ_π could be determined, these data confirm the calculations in the references [10] and [12].

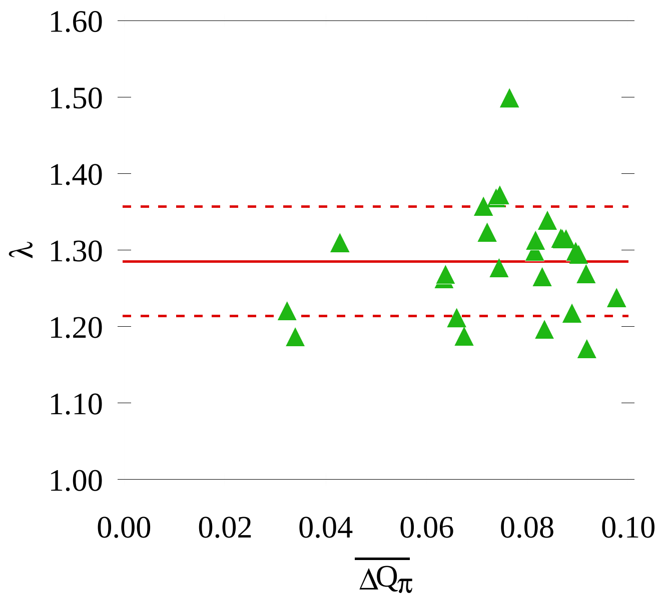

Figure 6.13: The derating factor, λ, calculated from ξ_{avg} and $\overline{\Delta Q_\pi}$, vs. ΔQ_π. The average value of the derating factor, $\lambda = 1.28 \pm 0.07$, is indicated by the horizontal lines.

6.5 Luminosity

As a final consistency check, the luminosity was measured using the CLEO-II endcap detector during the final two runs. From Equations 2.4a and 2.12, using the design emittance and current per bunch of $I = 20$ mA, a luminosity of 1.5×10^{31} cm^{-2} s^{-1} and $\xi = 0.1$ was expected, assuming no beam blowup. A maximum luminosity of 1.1×10^{31} cm^{-2} s^{-1}, $\overline{\Delta Q_\pi} = 0.098$ and $\xi_{avg} = 0.072$ (from the current and emittance) were achieved at a current per bunch of $I = 21$ mA. The electrons were blown up more than the positrons, and the currents were not precisely equal, so actually Equation 2.3 should be used to calculate the expected luminosity. A graphical comparison of the expected luminosity, calculated from Equation 2.3, and the measured luminosity is displayed in Figure 6.14. The agreement between the expected and measured luminosity indicates that the measurements of $I_\pm$ and $\varepsilon_\pm$ are trustworthy within the quoted error. Equation 2.3 can be thus used to infer the luminosity for data points at which the luminosity was not directly measured. Figure 6.15 shows the inferred luminosity and the simulated luminosity from Figure 5.13 for the resonantly coupled round beam lattice, E9A303000.JJ1_4S_15KG. The simulation and data agree at low currents, but simulation assumed that $\varepsilon_+ = \varepsilon_-$, so it is not surprising that it overestimates the luminosity at high currents.

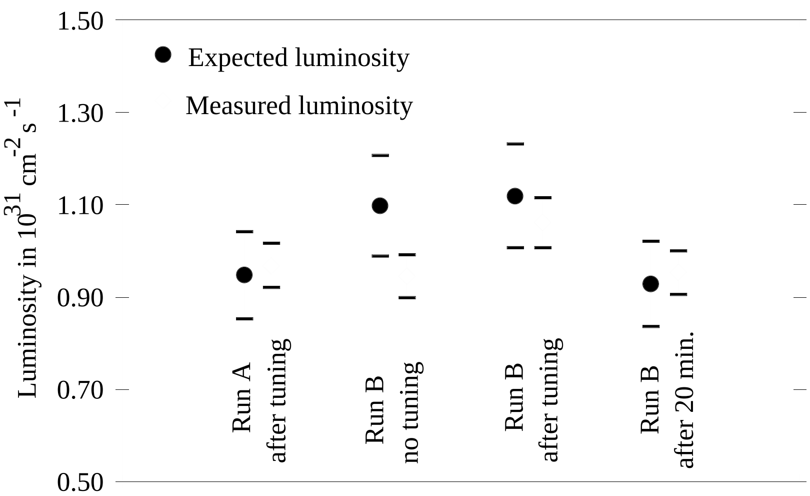

Figure 6.14: The expected luminosity (filled circles) was calculated from the measured beam currents and emittances using Equation 2.3. The measured luminosity (open diamonds) was obtained using the CLEO endcap detector during the two runs at the highest beam currents.

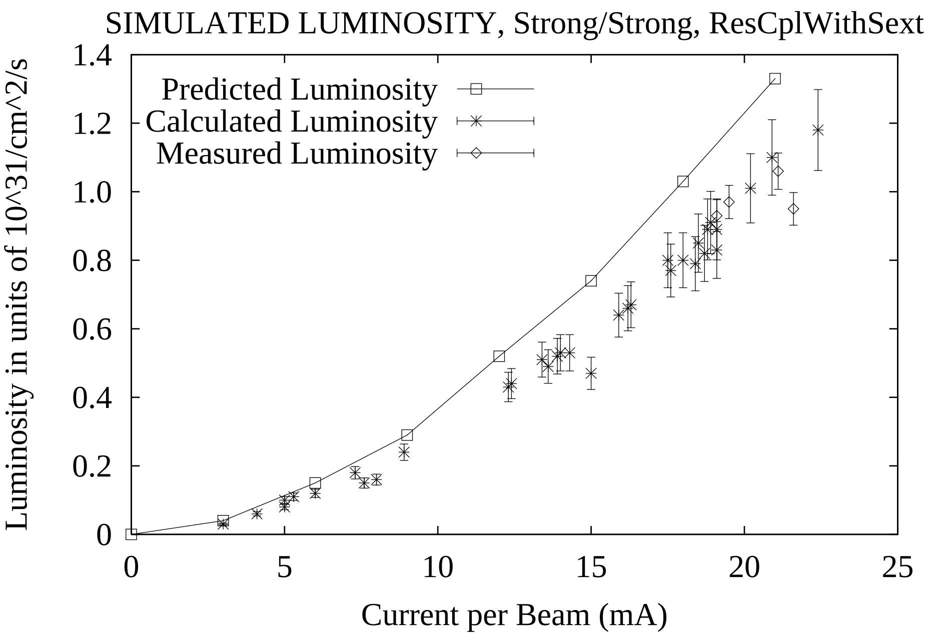

Figure 6.15: Figure 5.13[33] with the measured luminosity data points added. The measured luminosity was obtained using the CLEO endcap detector. The expected luminosity was calculated from the measured beam currents and emittances using Equation 2.3. In the simulation $\varepsilon_+ = \varepsilon_-$ was assumed, whereas during the experiment, usually $\xi_+ \neq \xi_-$.

6.6 Summary

The design tunes of $Q_x = Q_y = 0.77$ were chosen because in simulations, at that tune the luminosity was highest with the lowest beam blowup for both Möbius and resonantly coupled collisions. The tune scans done during weak-strong collisions, shown in Figures 6.4 through 6.6, support this choice.

As stated in Chapter 2, two factors that limit luminosity performance as a result of the beam-beam interaction are beam blowup and tune shift saturation. After the saturation point the beam sizes of both beams continue to increase with current, but the beam-beam tune shift parameter remains constant. Although the emittance blowup of both beams increased with ξ, there was no indication from the data that the saturation point had been reached.

The highest average tune shift observed was $\overline{\Delta Q_\pi} = 0.098$ and $\xi_{avg} = 0.072$, which are in line with predictions of what should be possible for round beams. The applicable theoretical derating factor λ has not been derived for the case $\varepsilon_+ \neq \varepsilon_-$[10], but for round beams with equal emittances, the theoretical λ increases from 1.21 to 1.28 as the emittance ratio, $\xi_+ : \xi_-$, increases to 2:1. $\lambda = 1.28 \pm 0.07$ is consistent with the data. It is remarkable that the theory and data agree so well since Yokoya and Koiso assumed that $2\pi\xi \ll 1$.

Finally, the luminosity measured during the last two runs agreed within errors with that predicted by the standard formulas, indicating that the emittance measurement and calibration of the CCD can be trusted. Since $\varepsilon_+ = \varepsilon_-$ is assumed in the simulations, but $\varepsilon_+ \neq \varepsilon_-$ in practice, further work needs to be done to refine the simulations, but as they stand, the simulation results can place an upper bound on the predicted round beam luminosity.

Chapter 7
Conclusion

In the introduction, arguments were presented for prefering round beams rather than flat beams. Recall that the formula for luminosity can be written as

$$\mathcal{L} = \frac{\gamma_0}{2er_e}\frac{\xi_y I}{\beta_y^*}\left(1 + \frac{\sigma_y^*}{\sigma_x^*}\right).$$

There is an automatic factor of two to be gained in luminosity because $(1 + \sigma_y^*/\sigma_x^*)_{flat} \simeq 1$ whereas $(1 + \sigma_y^*/\sigma_x^*)_{round} = 2$. However, the principal advantage of round beams is their stability in the presences of the beam-beam interaction, which allows large tune shift parameters, ξ, to be achieved. For instance, at CESR, the vertical beam-beam tune shift parameter, ξ_y, is typically about 0.04 during normal flat beam operation, whereas round beam simulations predict that $\xi > 0.1$ is possible before the beam size blows up enough to saturate ξ or cause beam lifetime limitations. At CESR $\beta_x^* = \beta_y^* = \beta^*$ is possible only for relatively large β^*, which limits achievable luminosity. On the other hand, ξ for a round beam is independent of β^*. For that reason the focus of the experiment was on ξ, along with other manifestations of the beam-beam interaction, the coherent π mode tune shift and emittance blowup.

These experiments successfully demonstrated that round beams can produce tune shifts and tune shift parameters of about twice that achieved during normal flat beam operation of CESR. The maximum tune shift observed was $\overline{\Delta Q_\pi} = 0.098$ at 21 mA per bunch, and during that same run, $\xi_{avg} = 0.072$, which was independently determined from the bunch currents and emittances. The correlation between independent measurements of ΔQ_π and ξ agree with the predictions of the models by Yokoya and Koiso[10] and Alexahin[12]. Although there was some emittance blowup of both beams, the tune shift was not yet saturated.

As is often the case with experimental data, there were a few unexplained observations. First, the electron bunch tended to be more blown up than the positron bunch. This tendency is also seen during flat beam operation of CESR. Certainly, if one bunch gains some sort of advantage and blows up the opposing bunch, then the inbalance will perpetuate itself; however, it is unclear why the "winning" bunch is almost always the positrons. Secondly, ΔQ_π^A and ΔQ_π^B typically differed by approximately 10%. This is perhaps an indication that the beams are slightly out of round.

The next step is to repeat these experiments with a Möbius insert in CESR. Simulations, such as the ones discussed in Section 5.4, have shown that beams made round by a Möbius insert are capable of even better luminosity, as well as being able to take advantage of chromaticity sharing. Because this preliminary work with resonantly coupled round beams has been done, the researchers at CESR who complete the studies of collisions in a Möbius storage ring will have an additional point of comparison. Happily, work has begun toward establishing collisions in the Möbius configuration.

Appendix A
Solenoid Compensation

As mentioned in Chapter 4, extraneous sources of transverse coupling, such as the CLEO solenoid, can produce undesirable effects which degrade luminosity. First, the width of the beam can be coupled to the height leading to an increase in the beam height at the IP which reduces beam density at the IP; this is of great concern during flat beam operation since the vertical beam size is much smaller than the horizontal beam size, so small increases can have a large effect on luminosity. Second, coupling can introduce vertical dispersion at the IP leading to an increase in the beam height due to the momentum spread of the beam and to misalignment if the beams have different average energies at the IP. Third, horizontal displacement of the beam in the arcs can contribute to vertical displacement at the IP resulting in non-head-on collision; this is a potential problem whether the beams are round or flat. Traditionally, the skew quadrupole components needed to compensate the CLEO solenoid have been introduced by rotating the pair of rare earth quadrupoles and the two pairs of iron core quadrupoles nearest the IP. Quadrupoles rotated about their axes by an arbitrary angle ϕ can be represented by the superposition of a normal quadrupole and a skew quadrupole. In this appendix, the derivation of the formulas presented in Chapter 4 will be presented in more detail[19, 22]. In this discussion, it is assumed that the only source of coupling to be compensated is

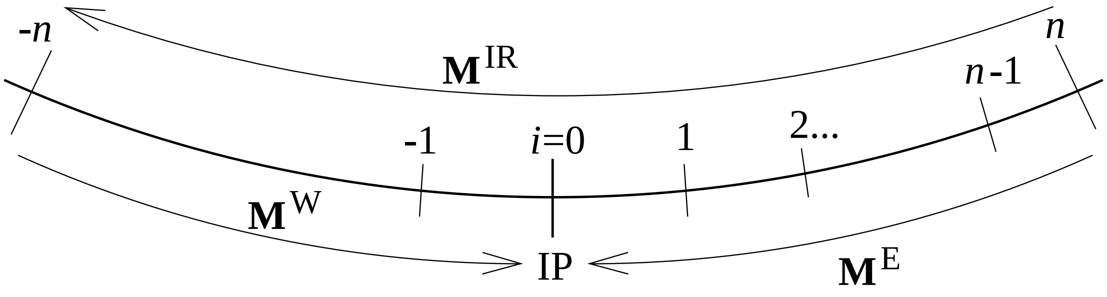

Figure A.1: A schematic definition of $\mathbf{M}^{\mathrm{IR}}$, the transfer matrix from east to west through the interaction region (IR); $\mathbf{M}^{\mathrm{E}}$, the transfer matrix from the east end of the IR to the interaction point (IP); and $\mathbf{M}^{\mathrm{W}}$, the transfer matrix from the IP to the west end of the IR.

the CLEO solenoid, and that outside the interaction region (the arcs), the transfer matrices are block diagonal. Figure 4.1 provides an illustration of the notation used to distinguish various IR transfer matrices; it is reprinted here as Figure A.1 for convenience.

To avoid the problems mentioned above, the following requirements must be met:

1. In order for horizontal and vertical motion to be uncoupled outside the interaction region, the full turn transfer matrix must be block diagonal. If there are no coupling elements outside the IR, then the transfer matrix through the IR, $\mathbf{M}^{\mathrm{IR}}$, must be made block diagonal,

$$\mathbf{M}^{\mathrm{IR}} = \begin{pmatrix} \mathbf{A}^{\mathrm{IR}} & \mathbf{0} \\ \mathbf{0} & \mathbf{D}^{\mathrm{IR}} \end{pmatrix}. \tag{A.1}$$

2. To prevent horizontal displacements or angles from being transported to the interaction point as vertical displacements, the first two elements of the third

row of the transport matrices from the arcs to the IP must be zero,

$$M_{31}^{\mathrm{E}} = 0, \quad M_{32}^{\mathrm{E}} = 0, \quad M_{31}^{\mathrm{W}} = 0, \quad M_{32}^{\mathrm{W}} = 0. \tag{A.2}$$

3. If the coupling and its compensation take place within a region that contains no dipole magnets so that variations of particle energy do not affect particle motion in that region, then no vertical dispersion will be introduced at the IP. Since the solenoid is compensated by rolling the first three quadrupoles on either side of the IP, this is automatically true.

The above equations seem to imply that as many as twelve variable parameters are needed to achieve compensation, eight to make $\mathbf{M}^{\mathrm{IR}}$ block diagonal and four to satisfy Equations A.2. However, transfer matrices are symplectic, which means that $\mathbf{M}^T\mathbf{S}\mathbf{M} = \mathbf{S}$ where $\mathbf{M}^T$ is $\mathbf{M}$ with rows and columns transposed and $\mathbf{S}$ is a $2k \times 2k$ matrix with $\begin{pmatrix} 0 & -1 \\ 1 & 0 \end{pmatrix}$ along the k 2×2 diagonal blocks and zeroes elsewhere[5]. For an arbitrary 4×4 symplectic matrix if one of the 2×2 off-diagonal blocks is zero, then the other off-diagonal block is zero as well.

Following Peggs[19] and Rubin[22], $\mathbf{M}^{\mathrm{IR}}$ and $\mathbf{M}^{\mathrm{E}}$ can be factored into the uncoupled transfer matrices between the couplers and matrices for weak coupling elements,

$$\begin{aligned} \mathbf{M}^{\mathrm{IR}} = {} & \mathbf{M}_{-n,-n+1}\mathbf{R}_{-n+1}\mathbf{M}_{-n+1,-n+2}\cdots \\ & \times\mathbf{R}_{-2}\mathbf{M}_{-2,-1}\mathbf{R}_{-1}\mathbf{M}_{-1,0}\mathbf{R}_{\mathbf{S}}\mathbf{M}_{0,1}\mathbf{R}_{1}\mathbf{M}_{1,2}\mathbf{R}_{2}\cdots \\ & \mathbf{M}_{n-2,n-1}\mathbf{R}_{n-1}\mathbf{M}_{n-1,n}, \end{aligned} \tag{A.3}$$

$$\mathbf{M}^{\mathrm{E}} = \mathbf{R}_{\frac{1}{2}S}\mathbf{M}_{0,1}\mathbf{R}_{1}\mathbf{M}_{1,2}\mathbf{R}_{2}\ldots\mathbf{M}_{n-2,n-1}\mathbf{R}_{n-1}\mathbf{M}_{n-1,n}. \tag{A.4}$$

The uncoupled transfer matrices are

$$\mathbf{M}_{i-1,i} \equiv \begin{pmatrix} \mathbf{T}_{i-1,i}^{x} & \mathbf{0} \\ \mathbf{0} & \mathbf{T}_{i-1,i}^{y} \end{pmatrix}, \tag{A.5}$$

where $\mathbf{T}_{i-1,i} = \mathbf{T}(\beta_i, \alpha_i; \beta_{i-1}, \alpha_{i-1}; \phi_i - \phi_{i-1})$ given by Equation 3.51, and matrices for weak coupling elements have the form

$$\mathbf{R}_i = \begin{pmatrix} \mathbf{I} & \mathbf{F}_i \\ -\mathbf{F}_i^\dagger & \mathbf{I} \end{pmatrix}, \tag{A.6}$$

where $\mathbf{F}$ are given below. $\mathbf{R}_S$ represents the solenoid at the IP, and $\mathbf{R}_{\frac{1}{2}S}$ represent one half of the solenoid. "Weak" implies that terms like $\mathbf{F}_i^2$ can be neglected when $\mathbf{M}^{\mathrm{E}}$ is expanded. This leads to a first approximation of the skew strengths needed to compensate the solenoid which can be refined numerically later. For instance, for $\mathbf{M}^{\mathrm{E}}$

$$\begin{aligned}
\mathbf{M}^{\mathrm{E}} &= \mathbf{R}_{\frac{1}{2}S}\mathbf{M}_{0,1}\mathbf{R}_1\mathbf{M}_{1,2}\mathbf{R}_2\ldots\mathbf{M}_{n-2,n-1}\mathbf{R}_{n-1}\mathbf{M}_{n-1,n} && \text{(A.7a)}\\
&= \mathbf{R}_{\frac{1}{2}S}\mathbf{M}_{0,1}\mathbf{R}_1\mathbf{M}_{0,1}^{-1}\mathbf{M}_{0,2}\mathbf{R}_2\mathbf{M}_{0,2}^{-1}\ldots\mathbf{M}_{0,n}\mathbf{R}_n\mathbf{M}_{0,n}^{-1}\mathbf{M}^{\mathrm{E^o}} && \text{(A.7b)}\\
&= \begin{pmatrix} \mathbf{I} & \mathbf{F}_{\frac{1}{2}S} \\ -\mathbf{F}_{\frac{1}{2}S}^\dagger & \mathbf{I} \end{pmatrix}\begin{pmatrix} \mathbf{X}^{0,1} & \mathbf{0} \\ \mathbf{0} & \mathbf{Y}^{0,1} \end{pmatrix}\begin{pmatrix} \mathbf{I} & \mathbf{F}_1 \\ -\mathbf{F}_1^\dagger & \mathbf{I} \end{pmatrix}\begin{pmatrix} \mathbf{X}_{0,1}^{-1} & \mathbf{0} \\ \mathbf{0} & \mathbf{Y}_{0,1}^{-1} \end{pmatrix}\\
&\quad \begin{pmatrix} \mathbf{X}_{0,2} & \mathbf{0} \\ \mathbf{0} & \mathbf{Y}_{0,2} \end{pmatrix}\begin{pmatrix} \mathbf{I} & \mathbf{F}_2 \\ -\mathbf{F}_2^\dagger & \mathbf{I} \end{pmatrix}\begin{pmatrix} \mathbf{X}_{0,2}^{-1} & \mathbf{0} \\ \mathbf{0} & \mathbf{Y}_{0,2}^{-1} \end{pmatrix}\cdots\begin{pmatrix} \mathbf{X}^{\mathrm{E}} & \mathbf{0} \\ \mathbf{0} & \mathbf{Y}^{\mathrm{E}} \end{pmatrix} && \text{(A.7c)}\\
&= \prod_{i=0}^{n}\begin{pmatrix} \mathbf{I} & \mathbf{X}_{0,i}\mathbf{F}_i\mathbf{Y}_{0,i}^{-1} \\ -\mathbf{Y}_{0,i}\mathbf{F}_i^\dagger\mathbf{X}_{0,i}^{-1} & \mathbf{I} \end{pmatrix}\begin{pmatrix} \mathbf{M}_x^{\mathrm{E}} & \mathbf{0} \\ \mathbf{0} & \mathbf{M}_x^{\mathrm{E}} \end{pmatrix} && \text{(A.7d)}\\
&\simeq \begin{pmatrix} \mathbf{I} & \sum_{i=1}^{n}\mathbf{X}_{0,i}\mathbf{F}_i\mathbf{Y}_{0,i}^{-1} \\ -\sum_{i=1}^{n}\mathbf{Y}_{0,i}\mathbf{F}_i^\dagger\mathbf{X}_{0,i}^{-1} & \mathbf{I} \end{pmatrix}\begin{pmatrix} \mathbf{M}_x^{\mathrm{E}} & \mathbf{0} \\ \mathbf{0} & \mathbf{M}_x^{\mathrm{E}} \end{pmatrix} && \text{(A.7e)}\\
&= \mathbf{M}^{\mathrm{E}'}\mathbf{M}^{\mathrm{E^o}}, && \text{(A.7f)}
\end{aligned}$$

where $\mathbf{M}^{\mathrm{E^o}}$ is the unperturbed, uncoupled transfer matrix for the east half of the IR, and $i = 0$ refers to the east half of the solenoid. A matrix $\mathbf{M}^{\mathrm{IR}'}$ can be similarly defined,

$$\mathbf{M}^{\mathrm{IR}'} = \begin{pmatrix} \mathbf{I} & \sum_{i=-n}^{n}\mathbf{X}_{0,i}\mathbf{F}_i\mathbf{Y}_{0,i}^{-1} \\ -\sum_{i=1}^{2n}\mathbf{Y}_{0,i}\mathbf{F}_i^\dagger\mathbf{X}_{0,i}^{-1} & \mathbf{I} \end{pmatrix}. \tag{A.8}$$

It is a simple exercise to show that if $M^{\mathrm{E}'}{}_{31} = 0$ and $M^{\mathrm{E}'}{}_{32} = 0$, then $M^{\mathrm{E}}{}_{31} = 0$ and $M^{\mathrm{E}}{}_{32} = 0$ and that if $\mathbf{M}^{\mathrm{IR}'}$ is block diagonal, then $\mathbf{M}^{\mathrm{IR}}$ is block diagonal also.

A solenoid's transfer matrix, $\mathbf{R}_S$, can be factored into a rotation through an angle, $\theta = KL$ and a lens which focuses in both planes with a strength proportional to θ^2. If the solenoid is weak, then the focusing can be ignored, and rotation can be approximated as $\mathbf{R}_\mathrm{S} = \begin{pmatrix} \mathbf{I} & \theta\,\mathbf{I} \\ -\theta\,\mathbf{I} & \mathbf{I} \end{pmatrix}$. In other words, $\mathbf{F}_\mathrm{S} = \begin{pmatrix} \theta & 0 \\ 0 & \theta \end{pmatrix}$. For the CLEO solenoid θ is 0.084, so it certainly qualifies as weak. For a skew quadrupole $\mathbf{F}_\mathrm{Skew} = \begin{pmatrix} 0 & 0 \\ -1/f & 0 \end{pmatrix}$ where f is the focal length of the skew quad. If these are substituted into Equation A.8, then for the off-diagonal blocks of $\mathbf{M}^\mathrm{IR}$ to be zero,

$$\theta\,\mathbf{I} + \sum_{i=-n, i\neq 0}^{n} q_i \mathbf{Q}_i, \tag{A.9}$$

where q_i is the "normalized" strength of a skew quadrupole, $q_i \equiv \sqrt{\beta_x \beta_y}/f$, and $\mathbf{Q}_i$ is a 2×2 matrix defined as

$$\mathbf{Q} \equiv \begin{pmatrix} -\sqrt{\frac{\beta_x^*}{\beta_y^*}} \sin\phi_x(s_i)\cos\phi_y(s_i) & -\sqrt{\beta_x^*\beta_y^*} \sin\phi_x(s_i)\sin\phi_y(s_i) \\ \frac{\cos\phi_x(s_i)\cos\phi_y(s_i)}{\sqrt{\beta_x^*\beta_y^*}} & -\sqrt{\frac{\beta_y^*}{\beta_x^*}} \cos\phi_x(s_i)\sin\phi_y(s_i) \end{pmatrix} \tag{A.10}$$

and $\phi_{x,y}(s_i)$ are the phase advances from the IP to the location of the coupler, s_i. Notice that for symmetrically placed pairs of skew quads, the elements of $\mathbf{Q}_i$ are either even or odd with respect to the IP such that

$$\mathbf{Q}_i = \begin{pmatrix} \text{odd} & \text{even} \\ \text{even} & \text{odd} \end{pmatrix}. \tag{A.11}$$

If the pairs of skew quadrupoles are powered anti-symmetrically[1] so that $q_{-i} = -q_i$, the four equations represented by Equation A.9 reduce to two equations,

$$\theta - 2\sum_{i=1}^{n} q_i \sqrt{\frac{\beta_x^*}{\beta_y^*}} \sin\phi_x(s_i)\cos\phi_y(s_i) = 0, \tag{A.12a}$$

$$\theta - 2\sum_{i=1}^{n} q_i \sqrt{\frac{\beta_y^*}{\beta_x^*}} \cos\phi_x(s_i)\sin\phi_y(s_i). \tag{A.12b}$$

[1] The term "anti-symmetric" means that the quadrupoles on the west side of the IP are rotated by angles equal and opposite to those on the east side, which is equivalent to skew quadrupoles on either side of the IP having equal absolute strengths but opposite polarities.

Thus, only two pairs of skew quadrupoles are needed to make $\mathbf{M}^{\mathrm{IR}}$ block diagonal.

In terms of q_i and $\mathbf{Q}_i$, ${M^{\mathrm{E}}}'_{31} = 0$ and ${M^{\mathrm{E}}}'_{32} = 0$ become

$$\frac{1}{2}\theta - \sum_{i=1}^{n} q_i \sqrt{\frac{\beta_x^*}{\beta_y^*}} \sin\phi_x(s_i)\cos\phi_y(s_i) = 0 \tag{A.13a}$$

$$-\sum_{i=1}^{n} q_i \sqrt{\beta_x^*\beta_y^*} \sin\phi_x(s_i)\sin\phi_y(s_i) = 0. \tag{A.13b}$$

The first of these two, Equation A.13a, is just one half of Equation A.12a, so it is automatically satisfied by making $\mathbf{M}^{\mathrm{IR}}$ block diagonal. Thus, only one additional pair of skew quadrupoles is necessary to satisfy Equations A.1 and A.2.

Stated another way, if $\mathbf{M}^{\mathrm{IR}'}$ is written in terms of $\mathbf{M}^{\mathrm{E}'}$ and anti-symmetric pairs of skew quadrupoles are assumed from the start, then with a little algebra it is possible to show the following:

- If $M^{\mathrm{E}'}_{31} = 0$ and $M^{\mathrm{E}'}_{32} = 0$, then $M^{\mathrm{E}}_{31} = 0$ and $M^{\mathrm{E}}_{32} = 0$.
- If $\mathbf{M}^{\mathrm{IR}'}$ is block diagonal, then $\mathbf{M}^{\mathrm{IR}}$ is block diagonal also.
- If $M^{\mathrm{E}'}_{31} = 0$, $M^{\mathrm{E}'}_{32} = 0$, and $M^{\mathrm{E}'}_{42} = 0$, then $\mathbf{M}^{\mathrm{IR}'}$ is block diagonal.

So in terms of $\mathbf{M}^{\mathrm{E}'}$, to compensate the solenoid

$${M^{\mathrm{E}}}'_{31} = 0, \tag{A.14}$$

$${M^{\mathrm{E}}}'_{32} = 0, \tag{A.15}$$

$${M^{\mathrm{E}}}'_{42} = 0, \tag{A.16}$$

will satisfy Equations A.1 and A.2.

Equations A.14 can be written in terms of the β-functions and coupler strengths. Assuming $\alpha_x^0 = 0$ and $\alpha_y^0 = 0$, the uncoupled transfer matrices, $\mathbf{T}_{0,i}$, in terms of the β-functions and phase advances are

$$\mathbf{T}_{0,i} = \begin{pmatrix} \sqrt{\beta^*/\beta^i}(\cos\phi_i - \alpha_i \sin\phi_i) & \sqrt{\beta^*\beta_i}\sin\phi_i \\ (-\sin\phi_i - \alpha_i\cos\phi_i)/\sqrt{\beta^*\beta_i} & \sqrt{\beta_i/\beta^*}\cos\phi_i \end{pmatrix}. \tag{A.17}$$

Multiplying out $\mathbf{M}^{\mathrm{E}\prime}$, equations (A.14) become

$$\sum_i \tilde{q}_i S_y^i C_x^i + \theta\sqrt{\beta_x^0/\beta_y^0} = 0, \tag{A.18}$$

$$-\sum_i \tilde{q}_i S_x^i C_y^i + \theta\sqrt{\beta_y^0/\beta_x^0} = 0, \tag{A.19}$$

$$\sum_i \tilde{q}_i S_y^i S_x^i = 0. \tag{A.20}$$

where $\tilde{q}_i = q_i/\sqrt{\beta_x^i\beta_y^i}$ is the "normalized" strength of the skew quadrupoles, $\theta = (KL)_{\text{solenoid}}$, $S_{x,y}^i = \sin\phi_{x,y}^i$, and $C_{x,y}^i = \cos\phi_{x,y}^i$. Each of the skew quadrupoles is characterized by an array of the coefficients, $V_i = (\, S_y^i C_x^i \quad -S_x^i C_y^i \quad S_y^i S_x^i \,)$. An economical arrangement of the skew quadrupoles has the V_i's nearly orthogonal. If such an arrangement is not possible, then the skew quadrupoles may need to be quite strong.

An assumption made in deriving Equation A.20 was that the solenoid's transfer matrix could be approximated as a small angle rotation ignoring the focusing effect at the ends of the solenoid. In practice, the solenoidal focusing cannot be ignored; however, in most cases, solving Equation A.20 is a good first first approximation. More general forms for $\mathbf{M}^{\mathrm{E}}$ and $\mathbf{M}^{\mathrm{E}\prime}$ that can be used to refine the solution of Equations A.20 and that do not assume knowledge of the β-functions are

$$\mathbf{M}^{\mathrm{E}} = \begin{pmatrix} \mathbf{A}^{\mathrm{E}} & \mathbf{B}^{\mathrm{E}} \\ \mathbf{C}^{\mathrm{E}} & \mathbf{D}^{\mathrm{E}} \end{pmatrix} \tag{A.21a}$$

$$\mathbf{M}^{\mathrm{E}\prime} = \mathbf{M}^{\mathrm{E}} \begin{pmatrix} \mathbf{A}_{\mathrm{E}}^{-1} & \mathbf{0} \\ \mathbf{0} & \mathbf{D}_{\mathrm{E}}{}^{-1} \end{pmatrix} = \begin{pmatrix} \mathbf{1} & \mathbf{B}^{\mathrm{E}\prime} \\ \mathbf{C}^{\mathrm{E}\prime} & \mathbf{1} \end{pmatrix}. \tag{A.21b}$$

Multiplying out Equations A.21b, Equations A.14 expressed in terms of elements of $\mathbf{M}^{\mathrm{E}}$ are

$$M^{\mathrm{E}\prime}{}_{31} = M_{31}^{\mathrm{E}} M_{22}^{\mathrm{E}} - M_{32}^{\mathrm{E}} M_{21}^{\mathrm{E}} = 0, \tag{A.22a}$$

$$M^{\mathrm{E}\prime}{}_{32} = M_{32}^{\mathrm{E}} M_{11}^{\mathrm{E}} - M_{31}^{\mathrm{E}} M_{12}^{\mathrm{E}} = 0, \tag{A.22b}$$

$$M^{\mathrm{E}\prime}{}_{42} = M_{42}^{\mathrm{E}} M_{11}^{\mathrm{E}} - M_{41}^{\mathrm{E}} M_{12}^{\mathrm{E}} = 0. \tag{A.22c}$$

If thin element skew quadrupoles are used in multiplying out $\mathbf{M}^{\mathrm{E}}$, then Equations A.22c are polynomials in powers of the skew quadrupole strengths and are easily solved with a symbolic algebra program. If thick element skew quadrupoles are used, Equations A.22c are polynomials in powers of transcendental functions of the skew quadrupole strengths — a bit more difficult to solve, but possible numerically.

In the course of compensating the solenoid, the β functions become distorted, which is a serious problem. The solution used at the time these experiments began was to treat the solenoid, rolled quadrupoles, and a few normal quadrupoles as an insert, and adjust quadrupole strengths and roll angles until the insert matched the β-functions at the IP and at the junction with the arcs. This solution was chosen because the lattice design machinery that was used assumed an uncoupled machine. Later, the machinery for designing CESR lattices was updated to handle weak coupling as simply another variable to be optimized, and the insert approach was abandoned.

Appendix B
Data from Resonantly Coupled Round Beam Collision

This appendix documents the colliding beam data. Section B.1 contains four tables. Table B.1 lists the kef for the comments in the tables of data. Table B.2 through Table B.5 document recorded beam profiles, corresponding beam spectra, and the conditions under which the profiles and spectra were recorded.

The beam profiles and corresponding fits are plotted in Section B.2. The figure captions correspond to the names of the original files of the digitized CCD data, and the final digits of the file name are the “CCD file #” used to identify each profile in Tables B.2 through B.5. The original files can be found on the CESR control system computers in the [cesr.mslog.mobius.data] area.

Plots of the beam spectra are collected in Section B.3. As for the beam profiles, the figure captions correspond to the names of the original files, which are in GIF format, and the last four digits are the “spectrum #” used to identify each spectrum in Tables B.2 through B.5. The original files can be found on the CESR control system computers in the [cesr.mslog.mobius.img] area.

B.1 Tables of Data

Table B.1: Key to comments in Tables B.2 through B.5.

Key	Meaning
a	Profile is not mentioned in machine studies log.
b	Beams are not colliding.
c	Positrons only.
d	Frequencies of modes were not recorded in CCD file.
e	Frequencies of coherent π modes not visible or not recorded in CCD file.
f	Each spectrum corresponds to a different setting for VCROSING7. Profile was recorded at setting that produced maximum tune split.
g	Positron CCD was saturated, so a reliable fit is not possible.
h	Electron profile is not symmetric, so fit to left side only.
i	Positron profile is missing.
j	Electron profile is missing.
k	$\|Q_A - Q_B\| \simeq 8$ kHz.

Table B.2: Data recorded on 18 September, 1996

				Normalize to average ε_0				
CCD file #	spectrum #	I_- mA	I_+ mA	ε_- nm-rad	ε_+ nm-rad	$\overline{Q}$	$\overline{\Delta Q_\pi}$	Comments
30		2.6	9.6		63.1			a,d,i
31		2.5	9.5	87.7	63.7			d
32		2.4	6.0	50.5	70.8	0.7687		b,g
33	2774	2.3	5.9	70.4	54.8	0.7689		e,f
	2773							
	2775							
	2776							
34		2.3	3.8	81.6	50.5	0.7610		b,g
35		2.3	3.8	93.3	46.2	0.7697		e
40		10.3	10.6	69.5	56.0	0.7621		b,g,h
41	2778	9.8	8.0	111.0	64.6	0.7696	0.0481	f,g,h
	2777							
42		5.7	4.3	67.9	45.4	0.7669		b
43	2779	5.7	4.3	91.4	61.6	0.7738	0.0314	g,h

Table B.3: Data recorded on 25 September, 1996

CCD file #	spectrum #	I_- mA	I_+ mA	Normalize to average ε_0: ε_- nm-rad	ε_+ nm-rad	$\overline{Q}$	$\overline{\Delta Q_\pi}$	Comments
50	2839	5.1	4.9	65.8	68.1	0.7695	0.0323	
51		7.9	4.0	61.2	74.2	0.7694	0.0428	
52		11.8	4.2	59.6	98.7	0.7681		a
53		11.8	3.2	58.5				a,d
54		11.8	3.4	58.5	85.5	0.7683		e
55		11.8	4.4	55.7		0.7669		e,i
60	2840	6.1	4.5	64.1	67.9	0.7696	0.0340	
61	2841	6.1	4.4	75.5	70.6	0.7578	0.0571	
62	2842	6.1	4.1	62.3	71.0	0.7821	0.0326	
63	2843	6.1	4.1	58.1	63.7	0.7951	0.0341	
64	2844	6.1	4.1	49.4	73.5	0.8077	0.0347	
65	2845	6.1	4.1	40.5	139.1	0.8179	0.0294	
66		6.1	4.1	40.2	140.4	0.8179	0.0294	a,d
67			4.5		59.0	0.7731		c
68			4.7		58.9	0.7731		c
69		9.3	5.2	65.1	79.3	0.7731		a,d
70	2846	9.3	5.2	63.2	79.9	0.7709		d
71		9.3	4.7	65.7	74.4	0.7604		d
72		9.3	4.4	65.5	77.7	0.7831		d
73		9.3	4.4	65.7	77.1	0.7831		d
74		9.3	4.4	60.8	78.2	0.7873		d

Table B.3 (Continued)

CCD file #	spectrum #	I_- mA	I_+ mA	Normalize to average ε_0 ε_- nm-rad	ε_+ nm-rad	$\overline{Q}$	$\overline{\Delta Q_\pi}$	Comments
75		12.1	3.8	60.2	88.4	0.7719		d
76		12.1	3.8	63.9	78.3	0.7601		d
77		12.1	3.0	71.7	76.9	0.7818		d
78		12.1	1.9	49.6	146.5	0.8074		d
79			5.0		59.0	0.7705		c
80			5.0		59.0	0.7576		c
81			5.1		57.4	0.7823		c
82			5.2		56.7	0.7942		c
83			4.7		53.4	0.8072		c
84			5.0		50.1	0.8204		c
85			4.7		46.4	0.8331		c

Table B.4: Data recorded on 9 October, 1996

CCD file #	spectrum #	I_- mA	I_+ mA	Normalize to average ε_0 ε_- nm-rad	ε_+ nm-rad	$\overline{Q}$	$\overline{\Delta Q_\pi}$	Comments
100		15.2	15.5		85.4			d,j
101		14.7	15.3	174.7	80.4	0.7687	0.0765	
105		14.1	14.9	113.8	82.0	0.7683	0.8422	a
106	2918	13.9	14.6	115.8	85.3	0.7691	0.0783	k
107	2919	13.4	14.6	111.4	84.1	0.7676	0.0746	k
108		13.3	14.4	115.4	79.9			a,d
109	2920	13.2	14.5	116.2	80.6	0.7716	0.0721	
110	2921	13.0	14.2	119.7	81.8	0.7743	0.0713	
111			14.0		63.5	0.7745		c
112		18.4	18.3	39.8	61.4	0.7666		b
113	2922	18.4	18.3	130.1	94.9	0.7674	0.0840	
114	2923	18.0	18.0	127.6	86.4	0.7685	0.0867	
115	2924	17.3	17.7	118.8	84.3	0.7641	0.0877	
116	2925	20.5	16.8	107.2	116.2	0.7679	0.0815	
117	2926	20.4	16.5	111.3	98.4	0.7672	0.0869	
118	2927	21.6	10.8	78.8	109.8	0.7679	0.0835	
119	2928	19.4	18.8	131.3	101.5	0.7674	0.0817	
120	2929	19.3	18.9	128.1	88.3	0.7676	0.0896	
121	2930	19.0	18.5	123.8	86.3	0.7678	0.0902	

Table B.5: Data recorded on 15 October, 1996

CCD file	spectrum	I_-	I_+	Normalize to average ε_0		$\overline{Q}$	$\overline{\Delta Q_\pi}$	Comments
				ε_-	ε_+			
#	#	mA	mA	nm-rad	nm-rad			
150		13.3	13.5	107.2	77.9	0.7696	0.0660	
151		12.2	12.5	102.9	80.7	0.7729	0.0635	
152		12.1	12.4	103.9	79.3	0.7756	0.0638	
153		18.1	14.6	118.5	89.9	0.7679	0.0745	
154	2974	17.7	14.1	107.1	98.9	0.7712	0.0674	
155	2975	16.6	18.5	128.2	83.4	0.7654	0.0830	
156		20.4	20.3	49.5	54.2	0.7618		b
157	2976	20.5	19.9	125.0	88.3	0.7630	0.0889	
158		21.8	22.9	135.7	89.4	0.7623	0.0918	
159	2979	20.5	21.4	128.2	83.4	0.7623	0.0978	
160		18.1	19.7	126.2	81.9	0.7628	0.0917	
161		26.9	26.9	56.0	40.6	0.7591		a

B.2 Plots of Beam Profiles

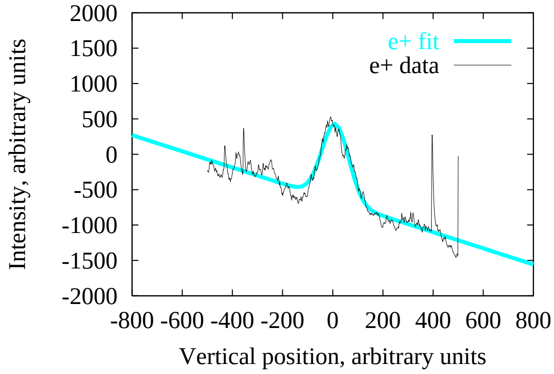

Figure B.1: COMET_CCD.DAT_30

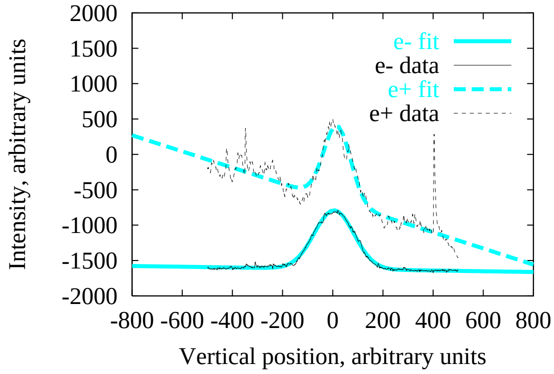

Figure B.2: COMET_CCD.DAT_31

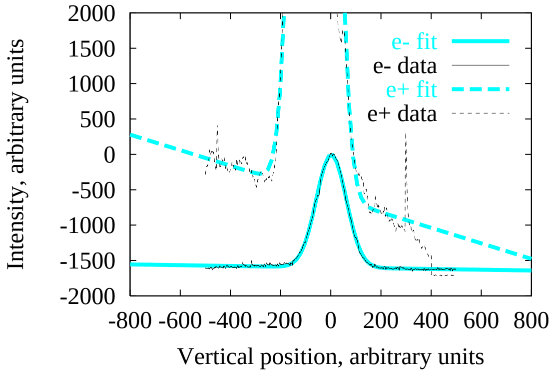

Figure B.3: COMET_CCD.DAT_32

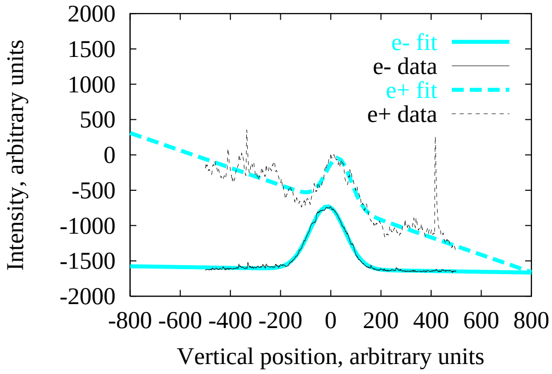

Figure B.4: COMET_CCD.DAT_33

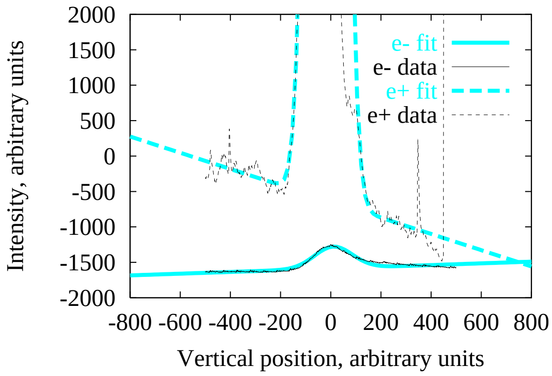

Figure B.5: COMET_CCD.DAT_34

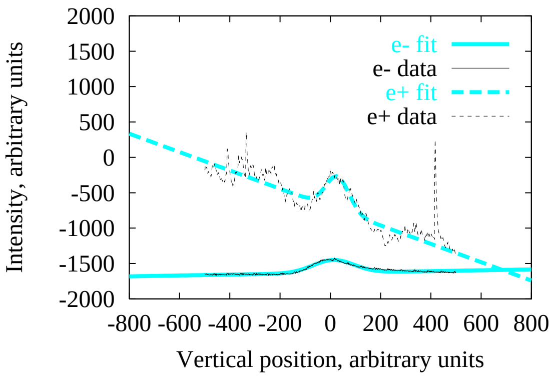

Figure B.6: COMET_CCD.DAT_35

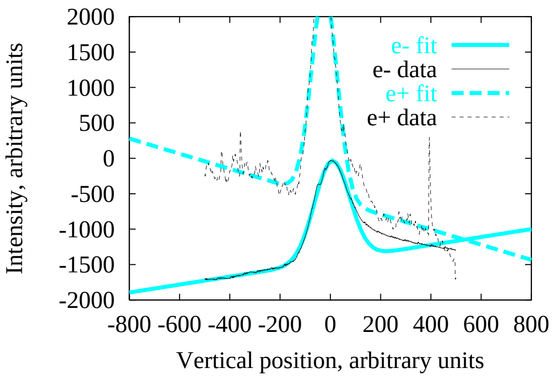

Figure B.7: COMET_CCD.DAT_40

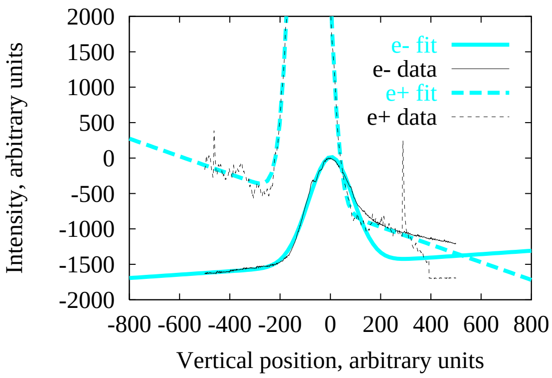

Figure B.8: COMET_CCD.DAT_41

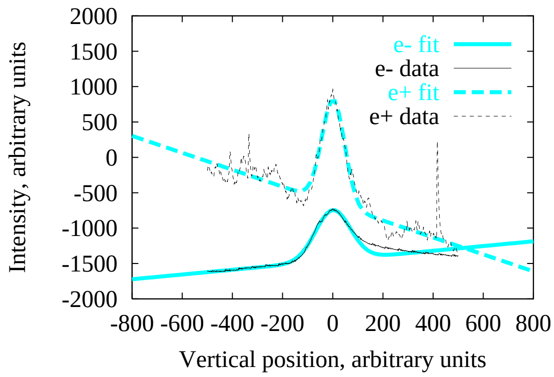

Figure B.9: COMET_CCD.DAT_42

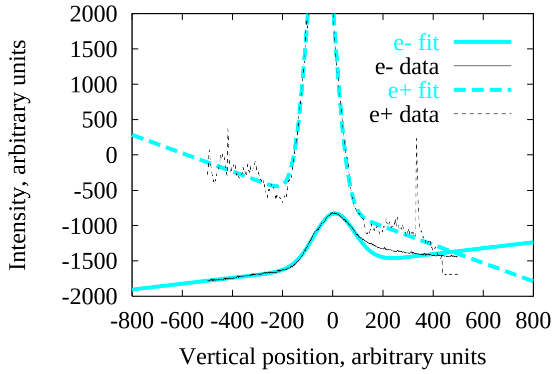

Figure B.10: COMET_CCD.DAT_43

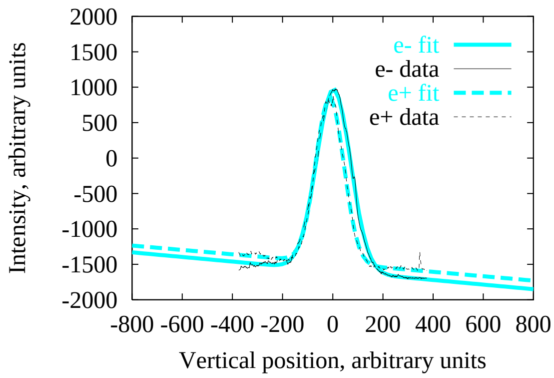

Figure B.11: COMET_CCD.DAT_50

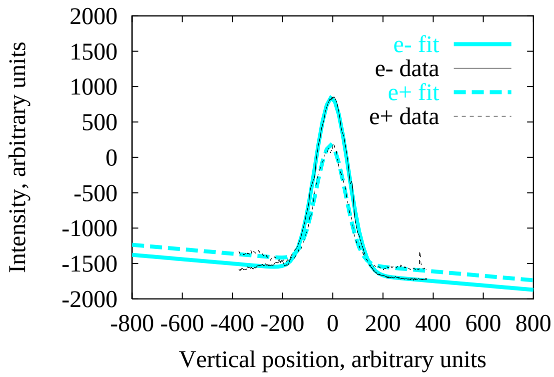

Figure B.12: COMET_CCD.DAT_51

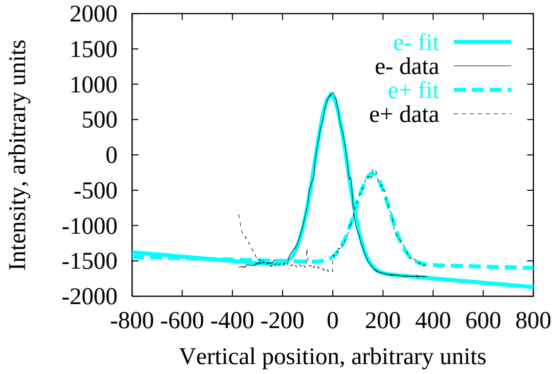

Figure B.13: COMET_CCD.DAT_52

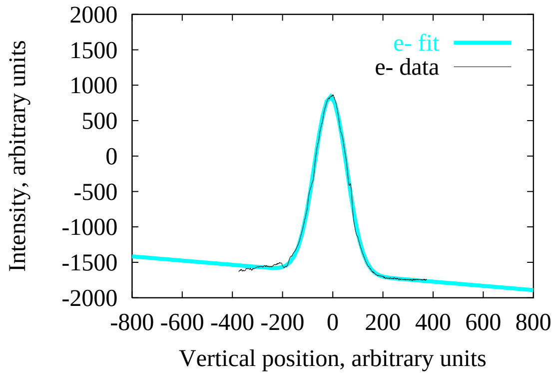

Figure B.14: COMET_CCD.DAT_53

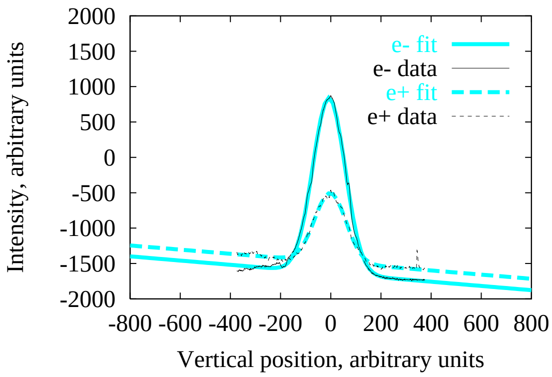

Figure B.15: COMET_CCD.DAT_54

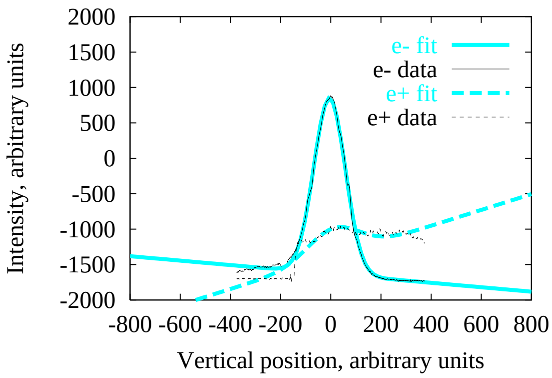

Figure B.16: COMET_CCD.DAT_55

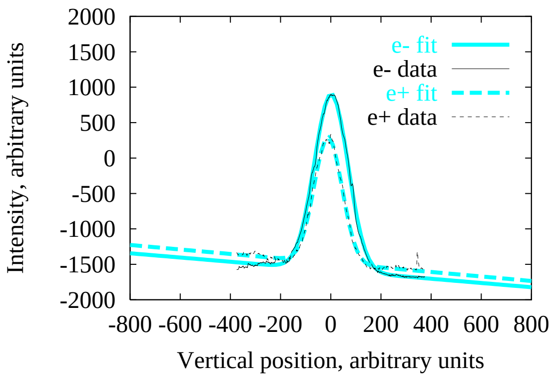

Figure B.17: COMET_CCD.DAT_60

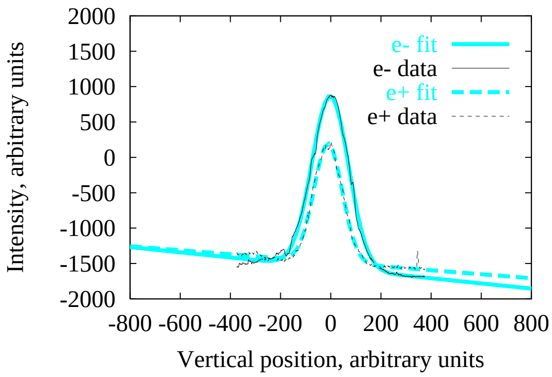

Figure B.18: COMET_CCD.DAT_61

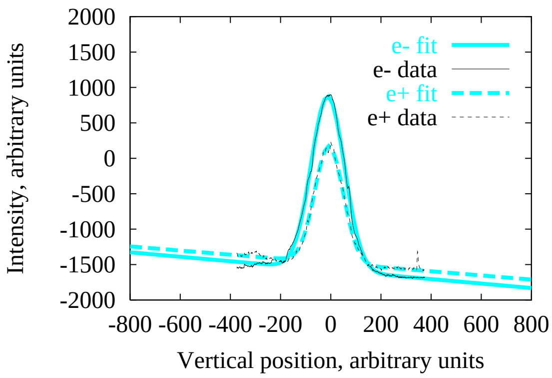

Figure B.19: COMET_CCD.DAT_62

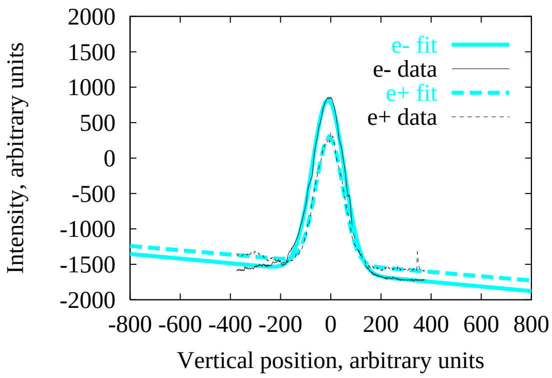

Figure B.20: COMET_CCD.DAT_63

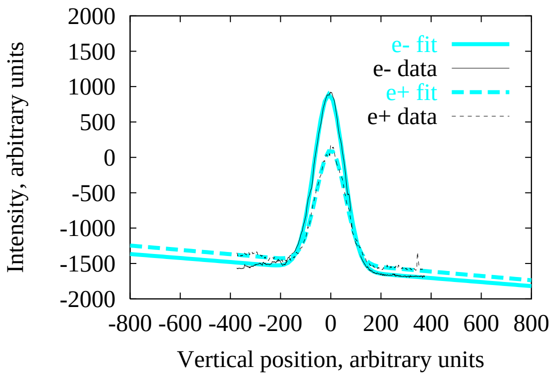

Figure B.21: COMET_CCD.DAT_64

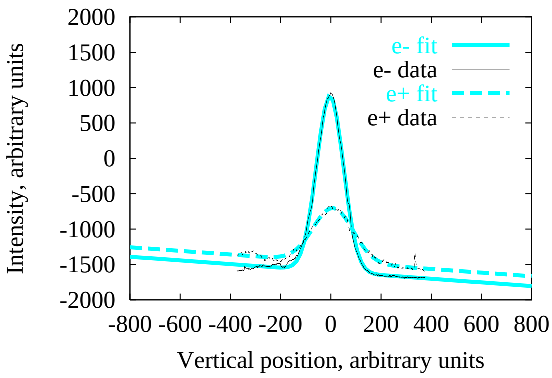

Figure B.22: COMET_CCD.DAT_65

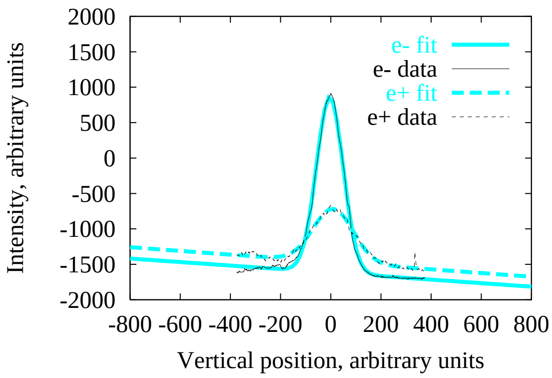

Figure B.23: COMET_CCD.DAT_66

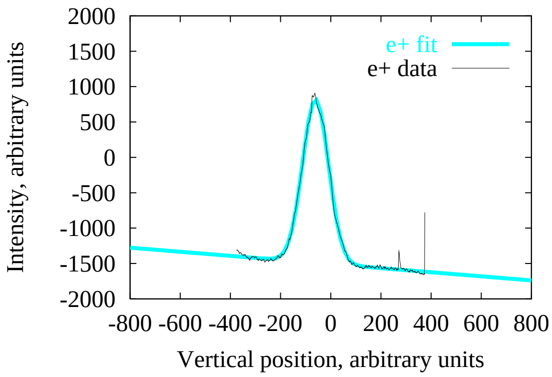

Figure B.24: COMET_CCD.DAT_67

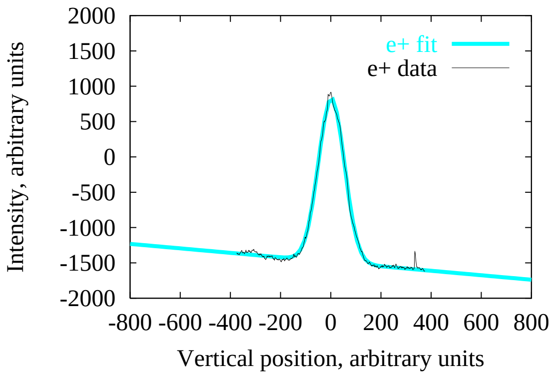

Figure B.25: COMET_CCD.DAT_68

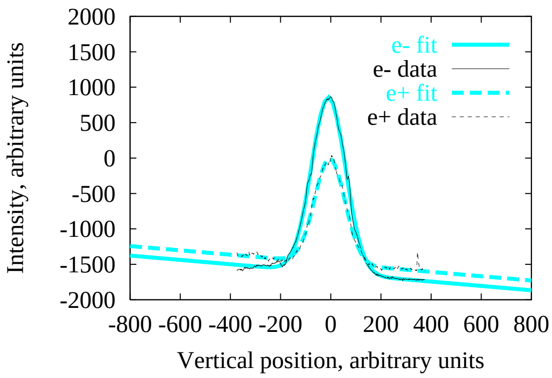

Figure B.26: COMET_CCD.DAT_69

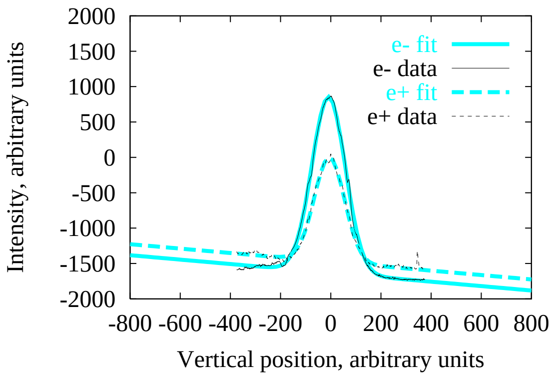

Figure B.27: COMET_CCD.DAT_70

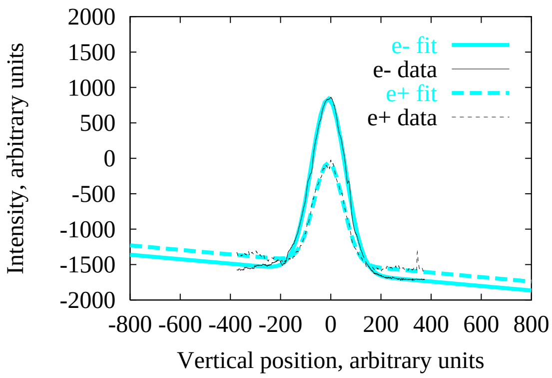

Figure B.28: COMET_CCD.DAT_71

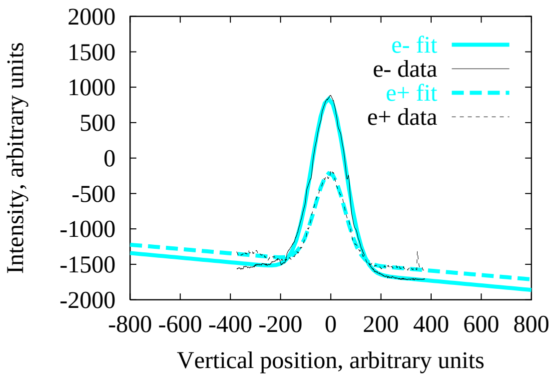

Figure B.29: COMET_CCD.DAT_72

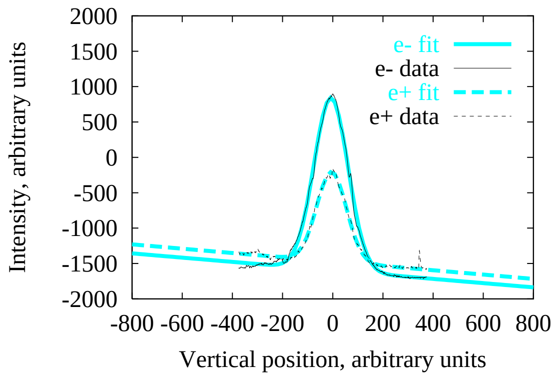

Figure B.30: COMET_CCD.DAT_73

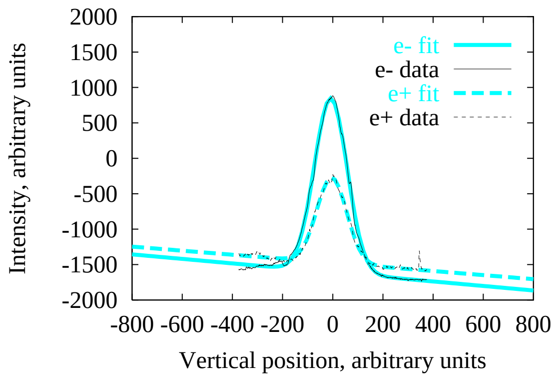

Figure B.31: COMET_CCD.DAT_74

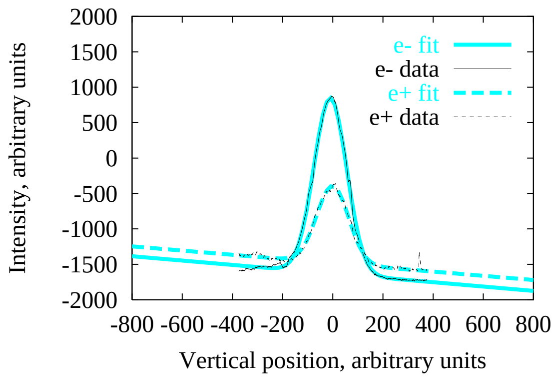

Figure B.32: COMET_CCD.DAT_75

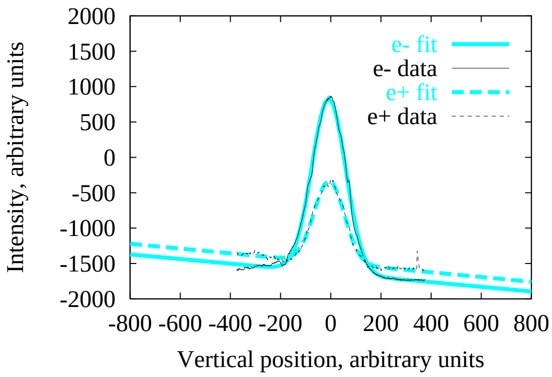

Figure B.33: COMET_CCD.DAT_76

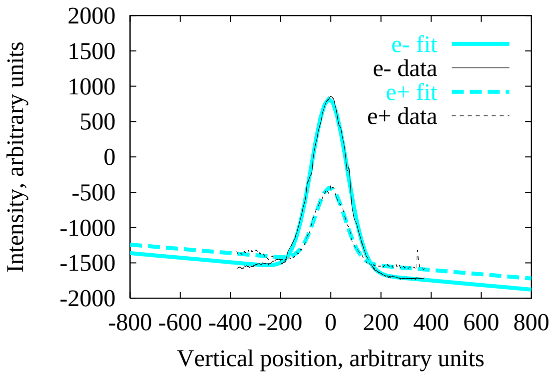

Figure B.34: COMET_CCD.DAT_77

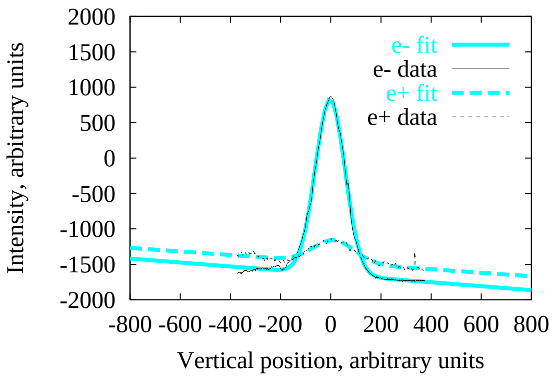

Figure B.35: COMET_CCD.DAT_78

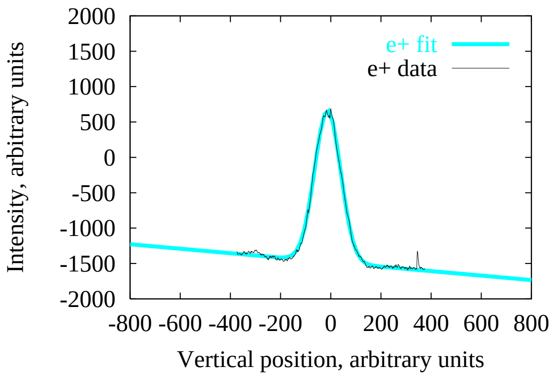

Figure B.36: COMET_CCD.DAT_79

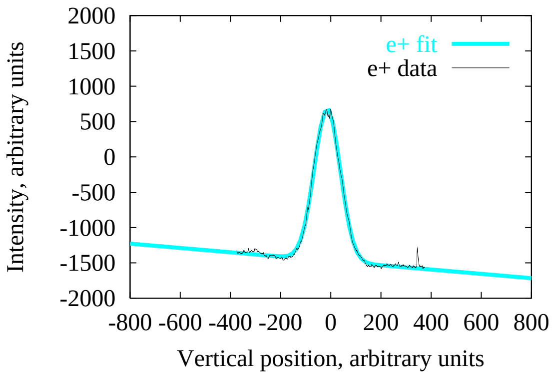

Figure B.37: COMET_CCD.DAT_80

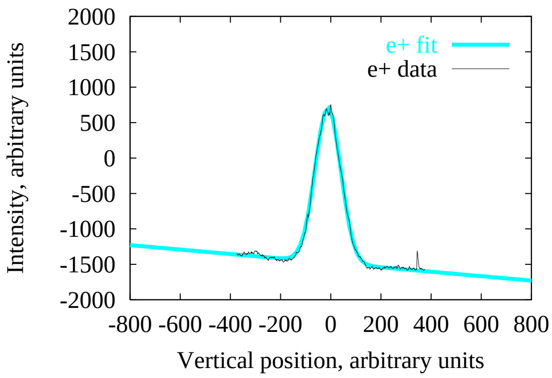

Figure B.38: COMET_CCD.DAT_81

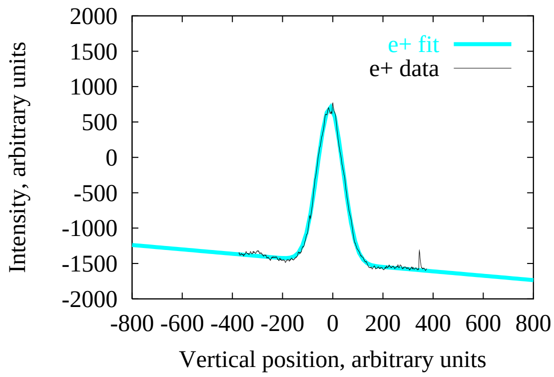

Figure B.39: COMET_CCD.DAT_82

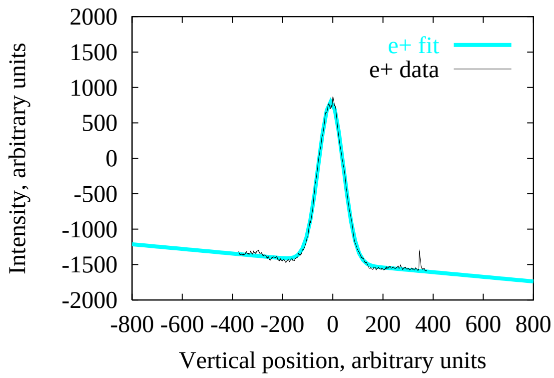

Figure B.40: COMET_CCD.DAT_83

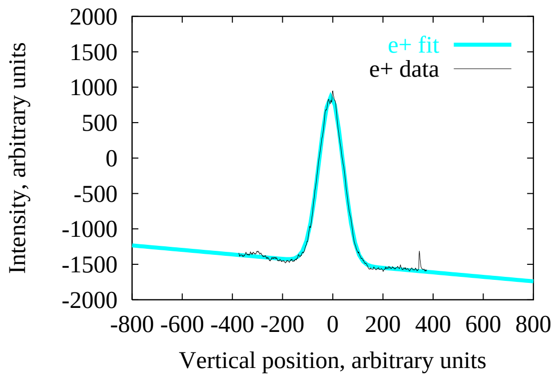

Figure B.41: COMET_CCD.DAT_84

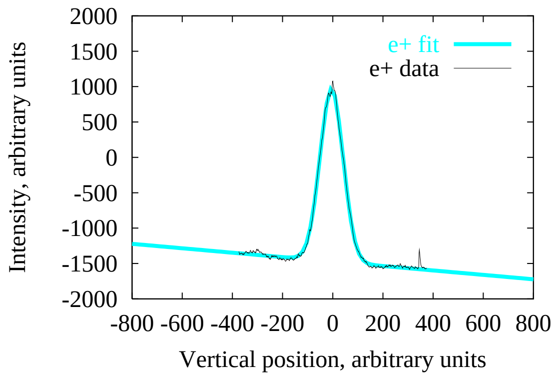

Figure B.42: COMET_CCD.DAT_85

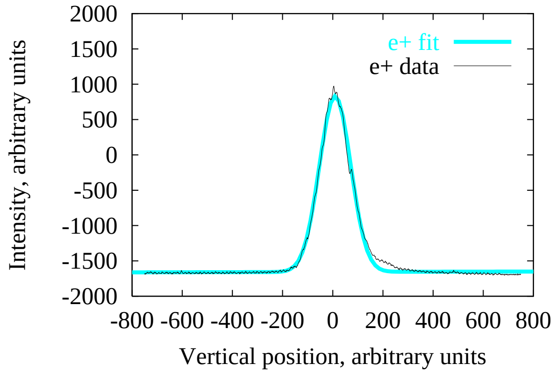

Figure B.43: COMET_CCD.DAT_100

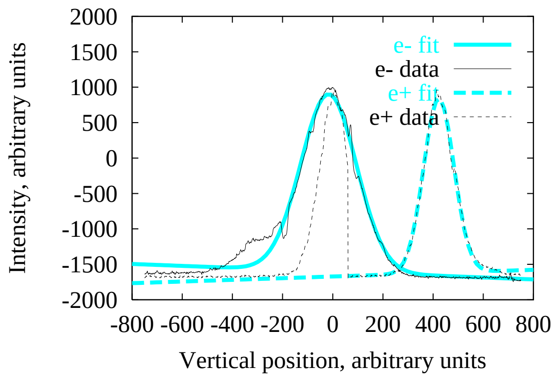

Figure B.44: COMET_CCD.DAT_101

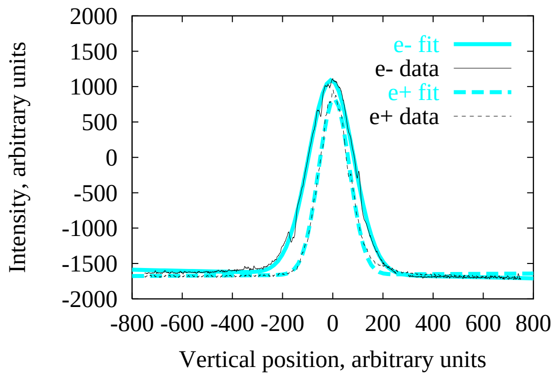

Figure B.45: COMET_CCD.DAT_105

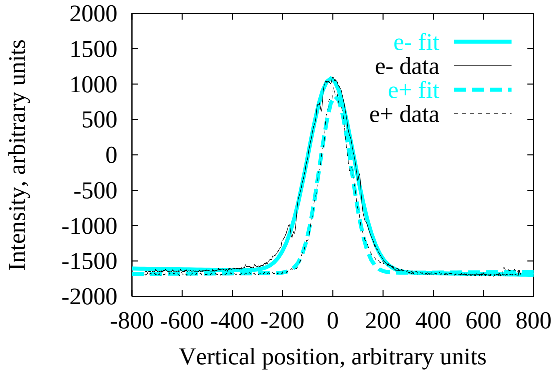

Figure B.46: COMET_CCD.DAT_106

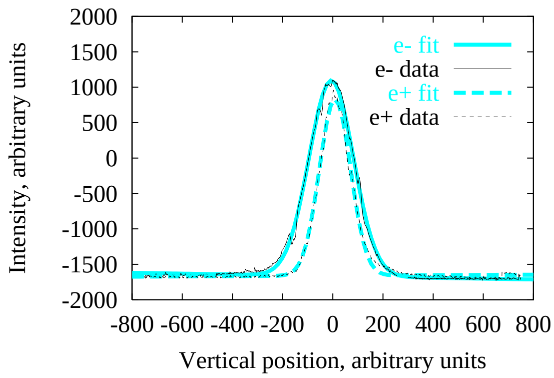

Figure B.47: COMET_CCD.DAT_107

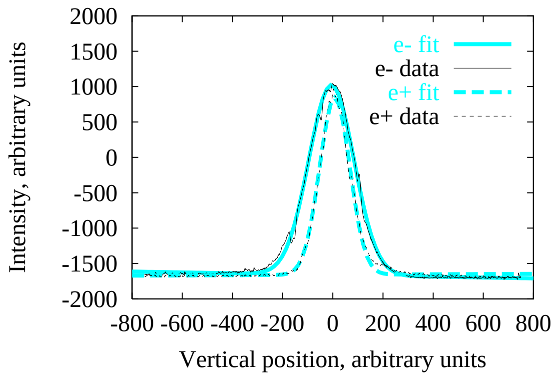

Figure B.48: COMET_CCD.DAT_108

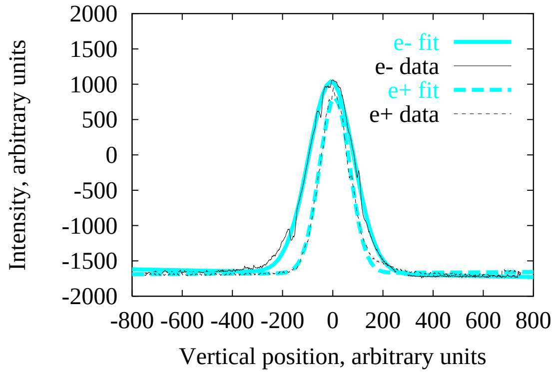

Figure B.49: COMET_CCD.DAT_109

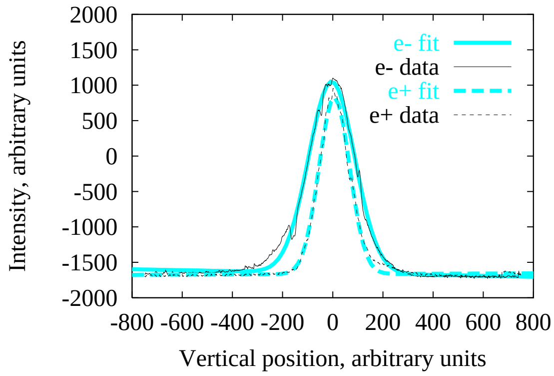

Figure B.50: COMET_CCD.DAT_110

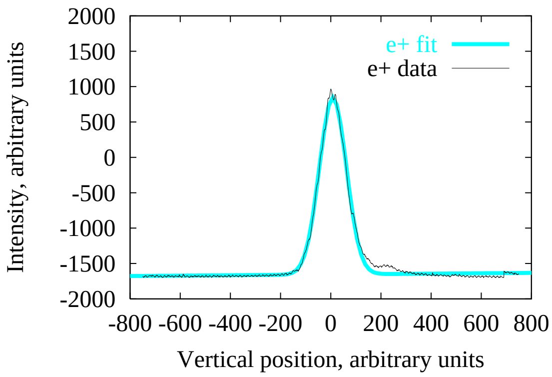

Figure B.51: COMET_CCD.DAT_111

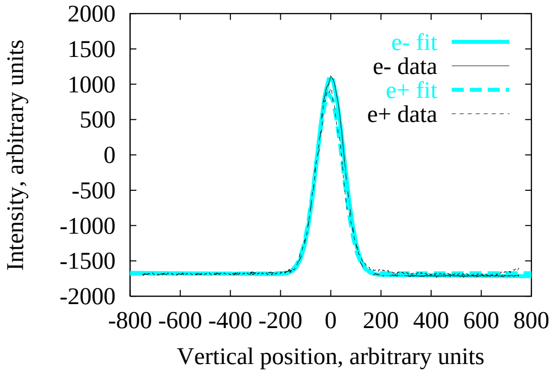

Figure B.52: COMET_CCD.DAT_112

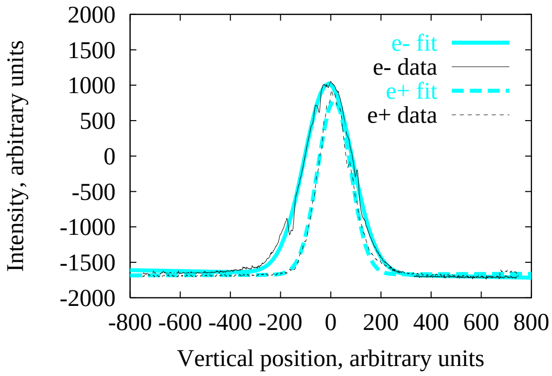

Figure B.53: COMET_CCD.DAT_113

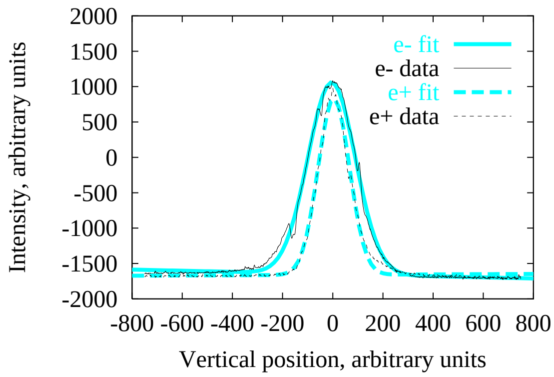

Figure B.54: COMET_CCD.DAT_114

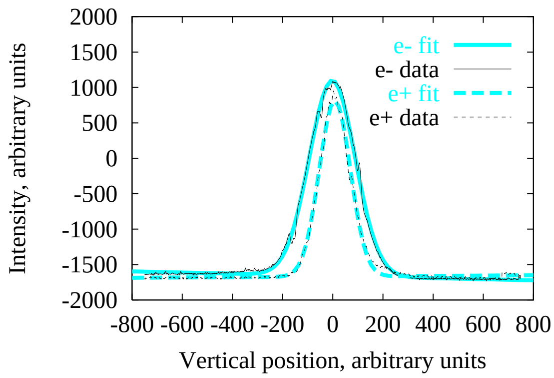

Figure B.55: COMET_CCD.DAT_115

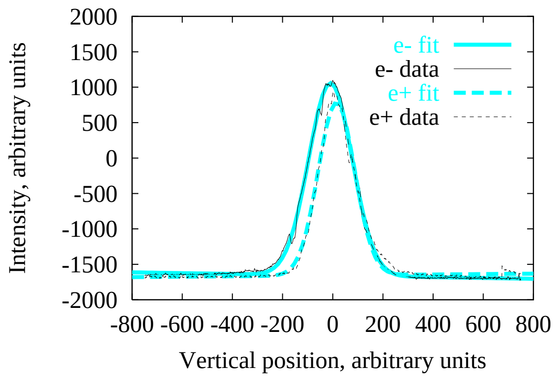

Figure B.56: COMET_CCD.DAT_116

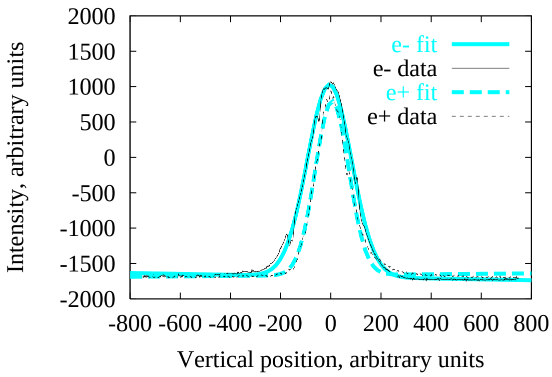

Figure B.57: COMET_CCD.DAT_117

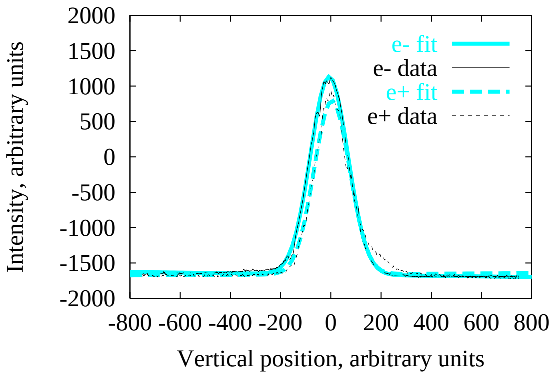

Figure B.58: COMET_CCD.DAT_118

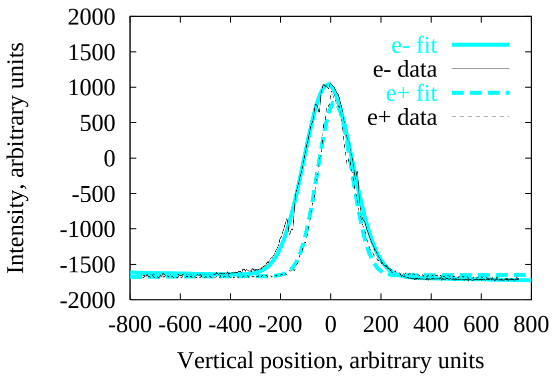

Figure B.59: COMET_CCD.DAT_119

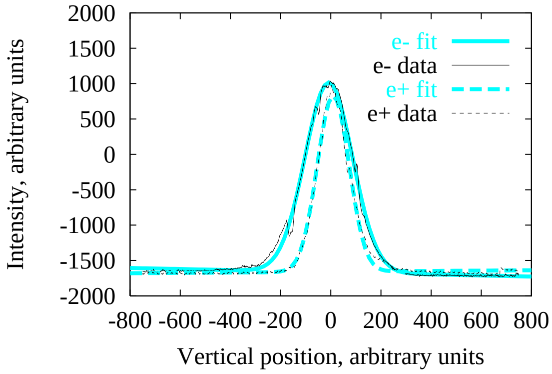

Figure B.60: COMET_CCD.DAT_120

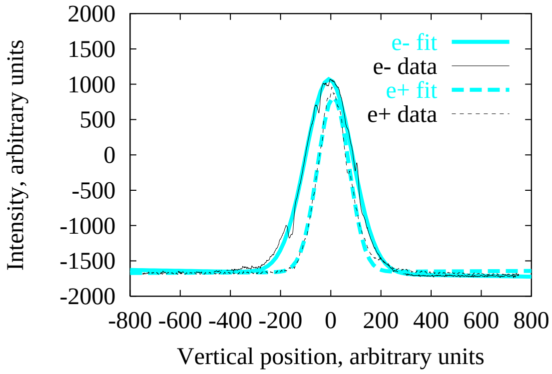

Figure B.61: COMET_CCD.DAT_121

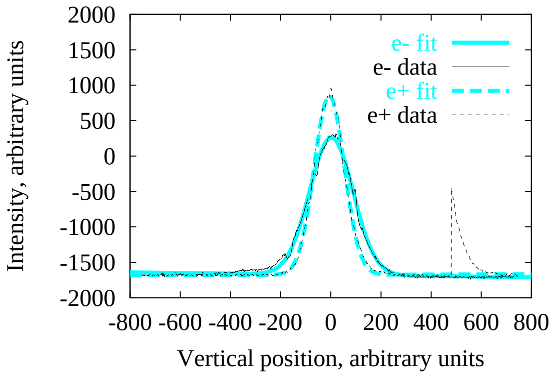

Figure B.62: COMET_CCD.DAT_150

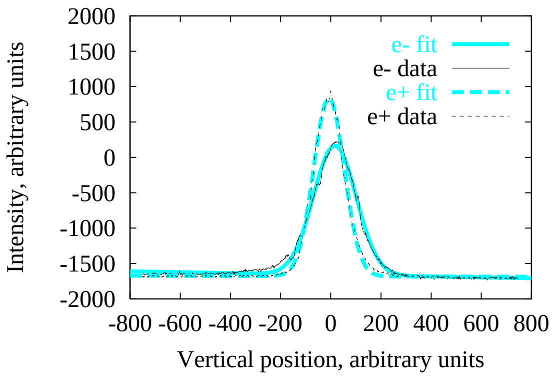

Figure B.63: COMET_CCD.DAT_151

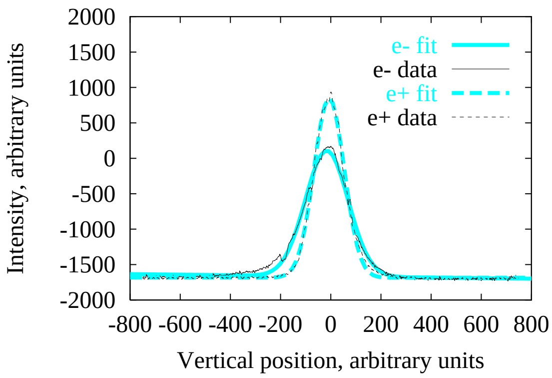

Figure B.64: COMET_CCD.DAT_152

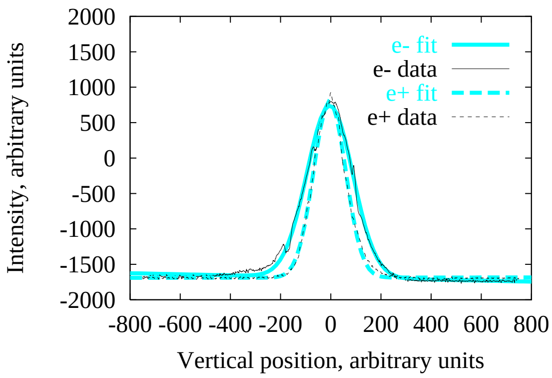

Figure B.65: COMET_CCD.DAT_153

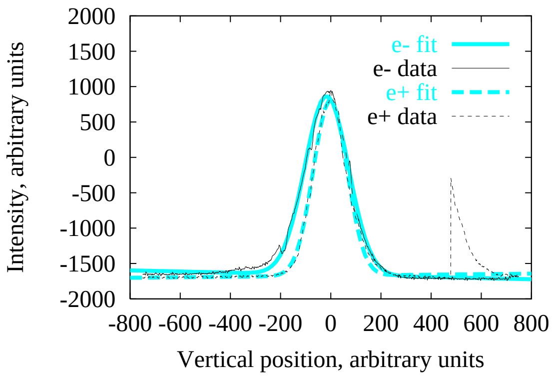

Figure B.66: COMET_CCD.DAT_154

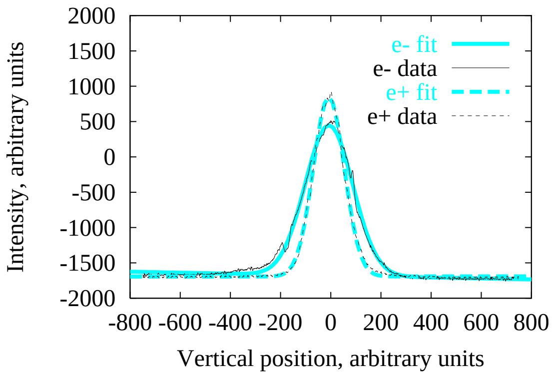

Figure B.67: COMET_CCD.DAT_155

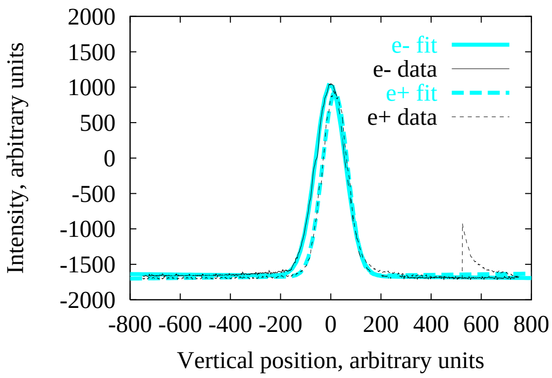

Figure B.68: COMET_CCD.DAT_156

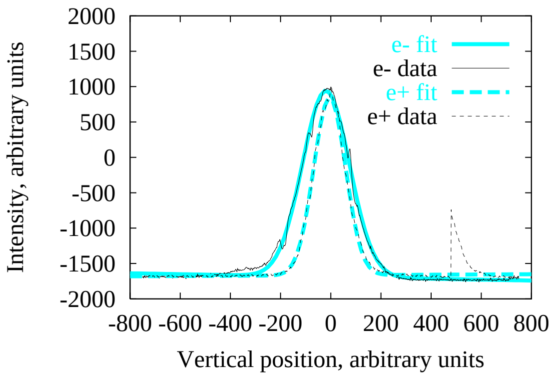

Figure B.69: COMET_CCD.DAT_157

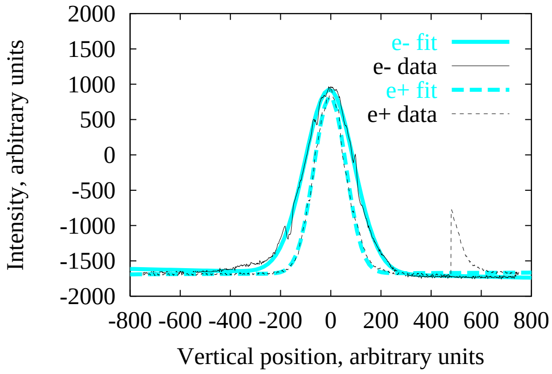

Figure B.70: COMET_CCD.DAT_158

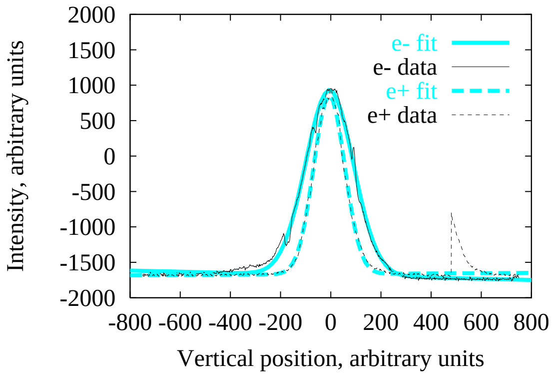

Figure B.71: COMET_CCD.DAT_159

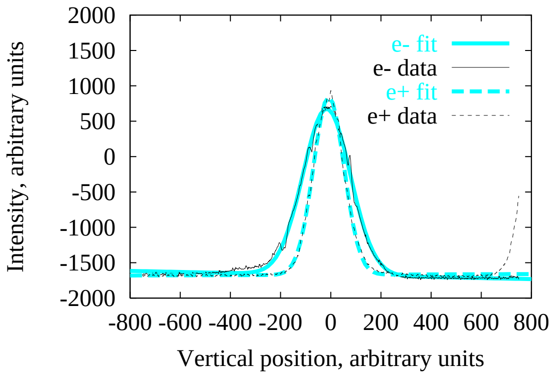

Figure B.72: COMET_CCD.DAT_160

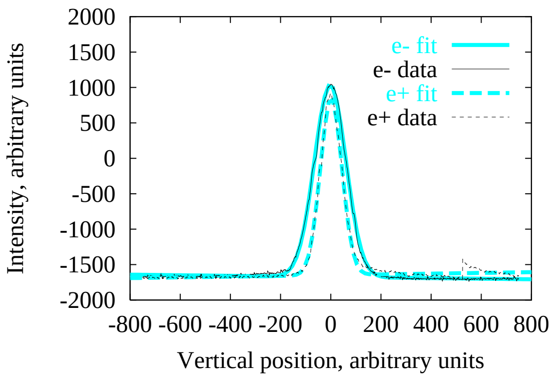

Figure B.73: COMET_CCD.DAT_161

B.3 Plots of Beam Spectra

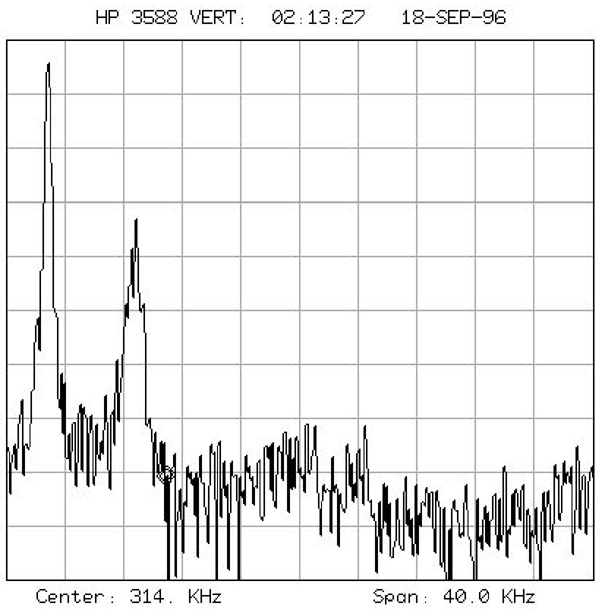

Figure B.74: STD_00002773.GIF

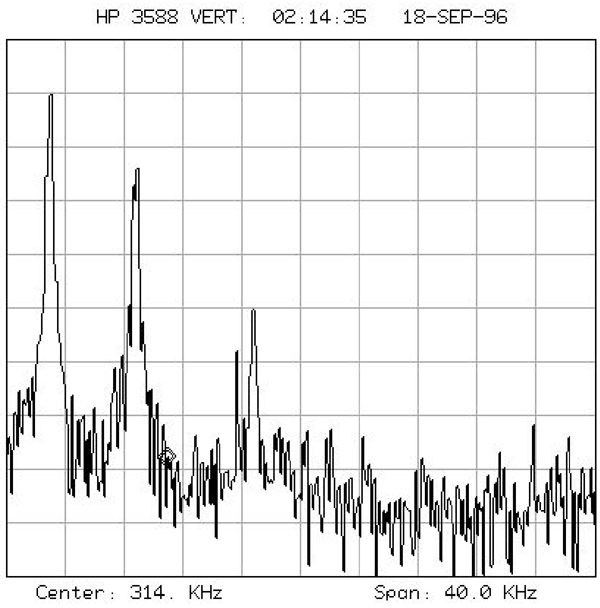

Figure B.75: STD_00002774.GIF

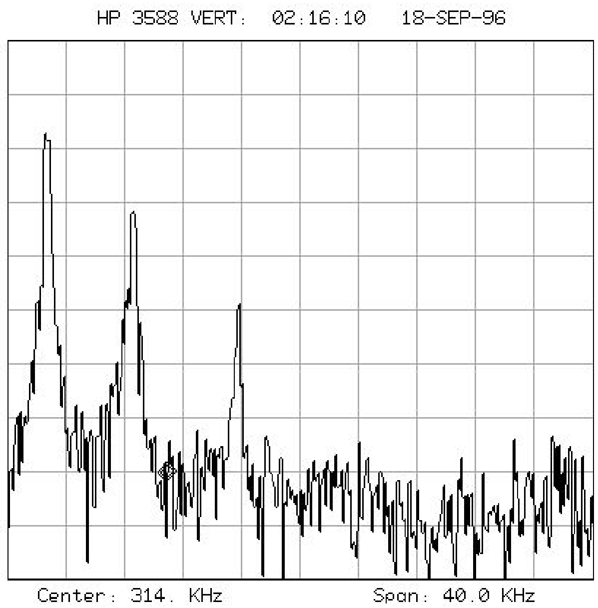

Figure B.76: STD_00002775.GIF

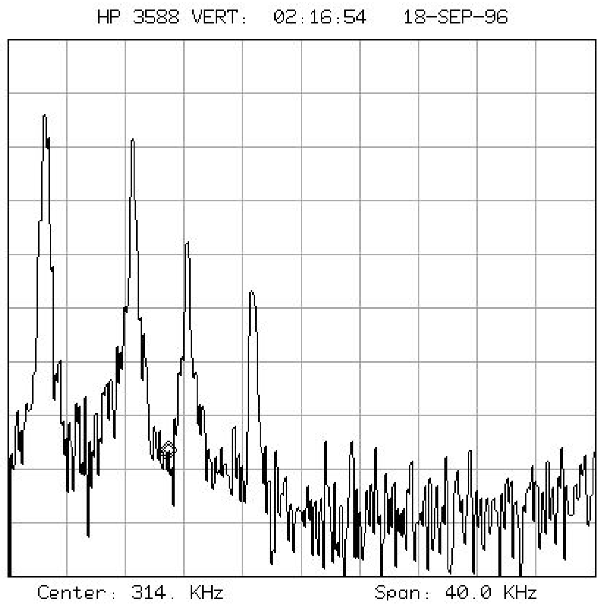

Figure B.77: STD_00002776.GIF

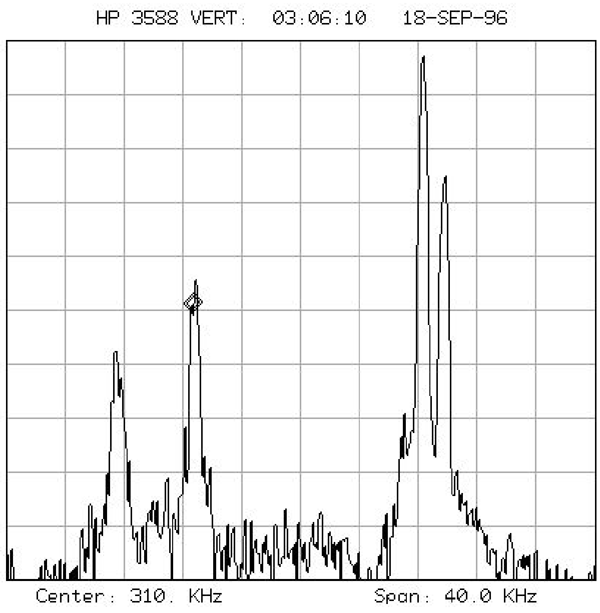

Figure B.78: STD_00002777.GIF

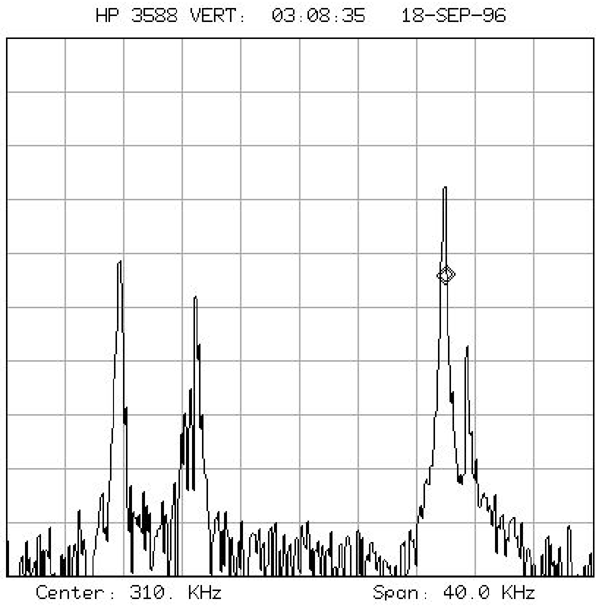

Figure B.79: STD_00002778.GIF

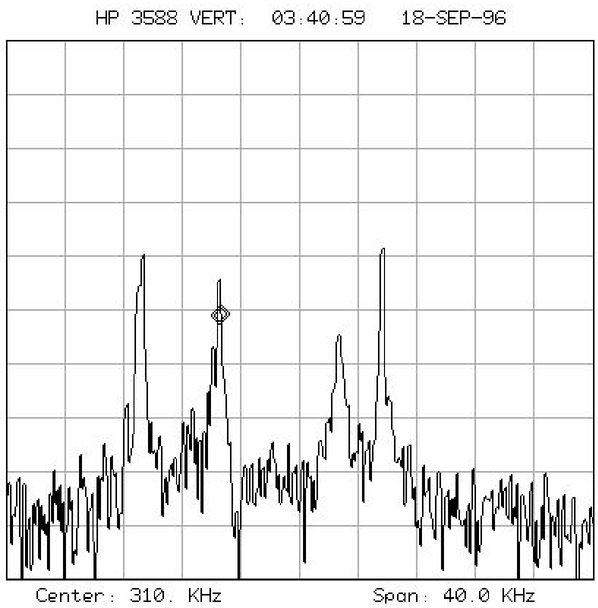

Figure B.80: STD_00002779.GIF

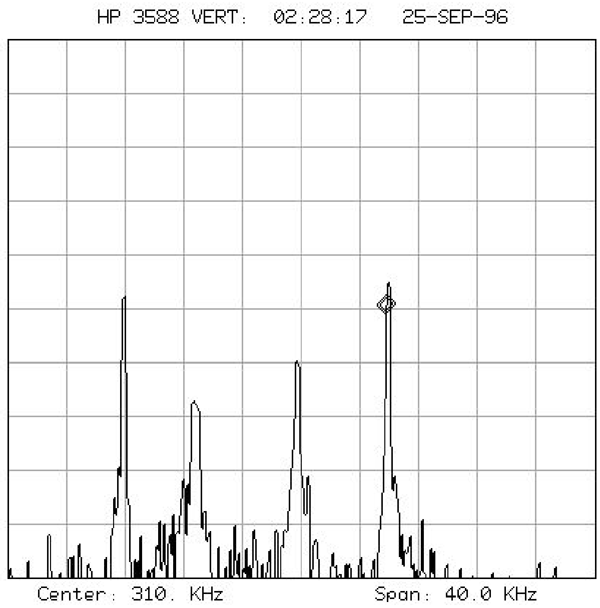

Figure B.81: STD_00002839.GIF

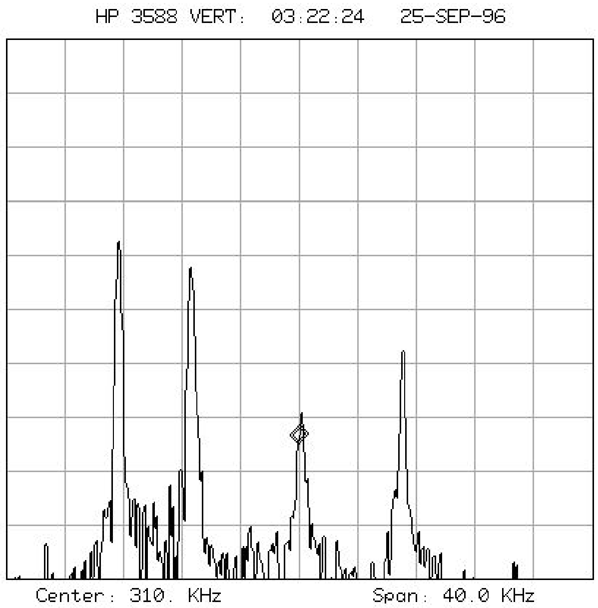

Figure B.82: STD_00002840.GIF

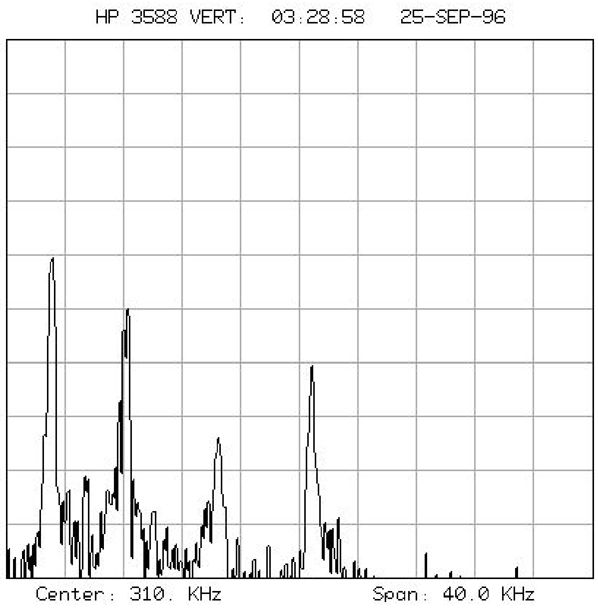

Figure B.83: STD_00002841.GIF

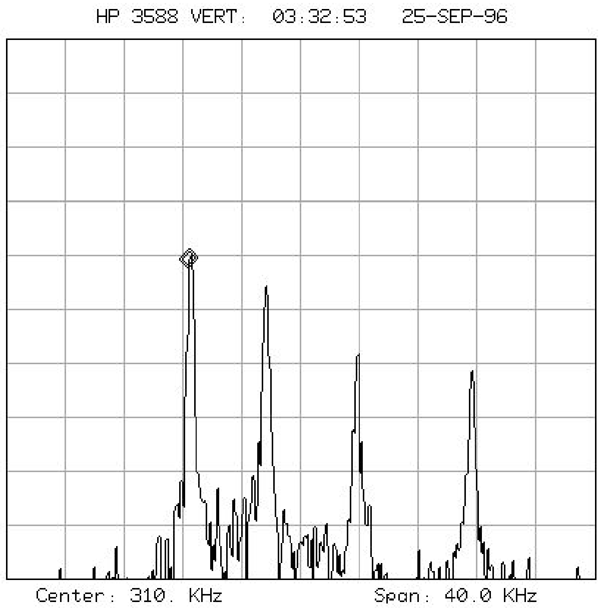

Figure B.84: STD_00002842.GIF

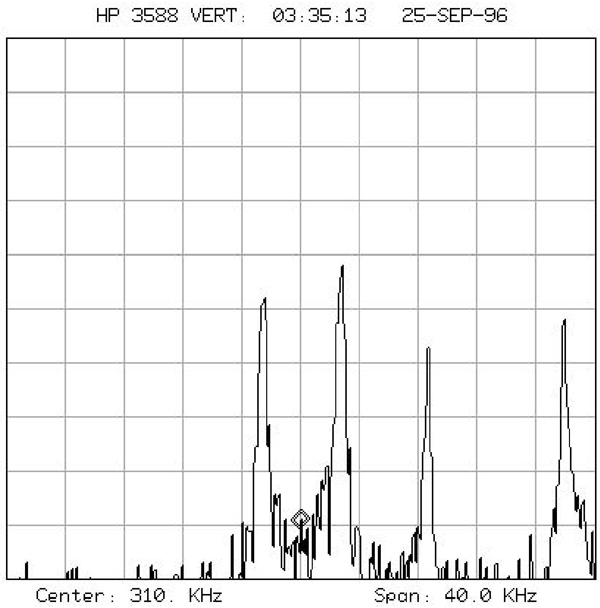

Figure B.85: STD_00002843.GIF

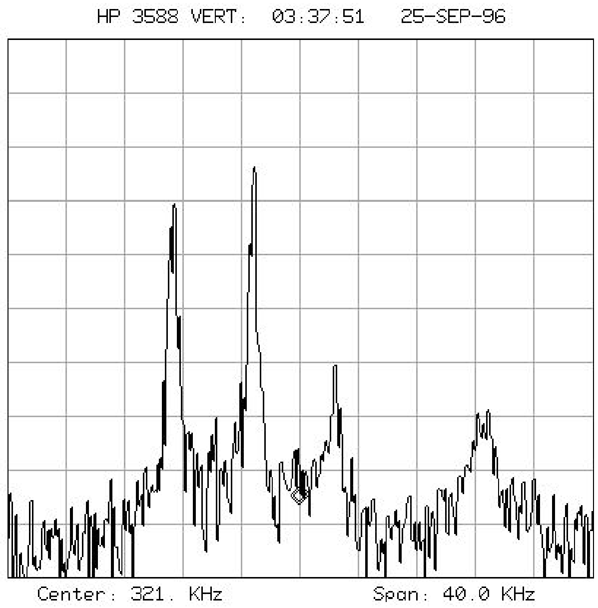

Figure B.86: STD_00002844.GIF

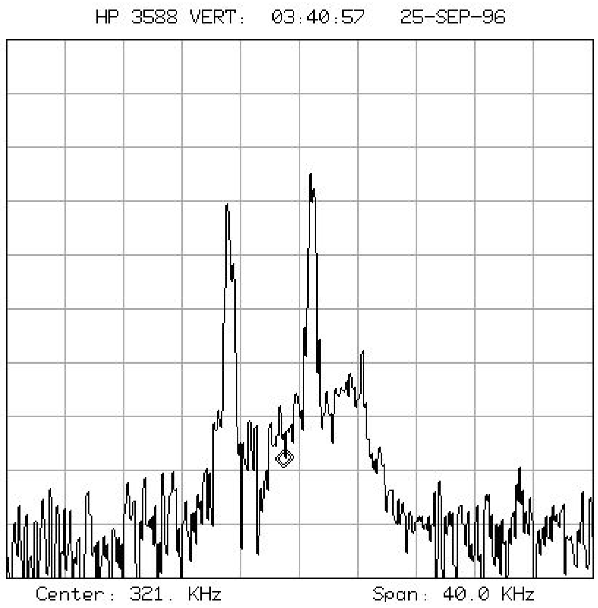

Figure B.87: STD_00002845.GIF

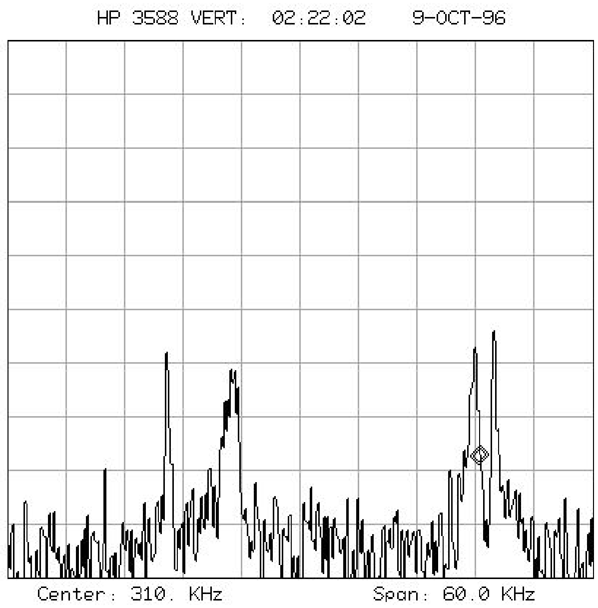

Figure B.88: STD_00002918.GIF

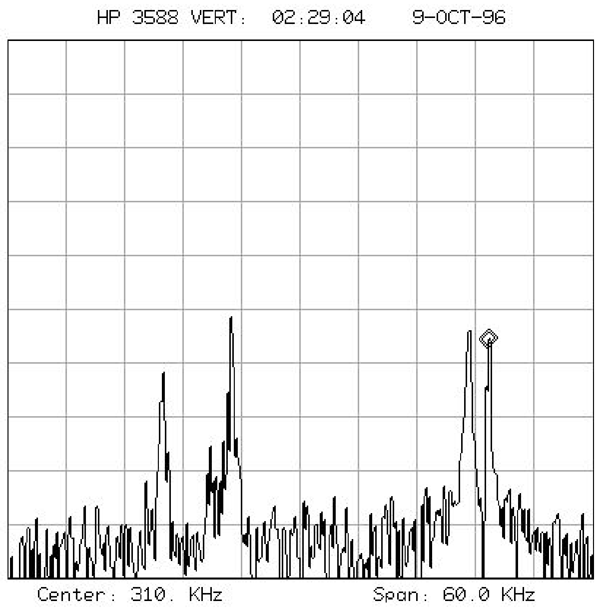

Figure B.89: STD_00002919.GIF

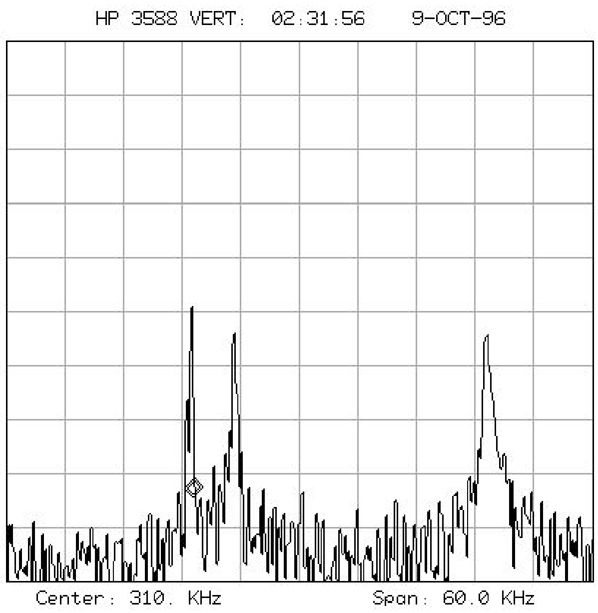

Figure B.90: STD_00002920.GIF

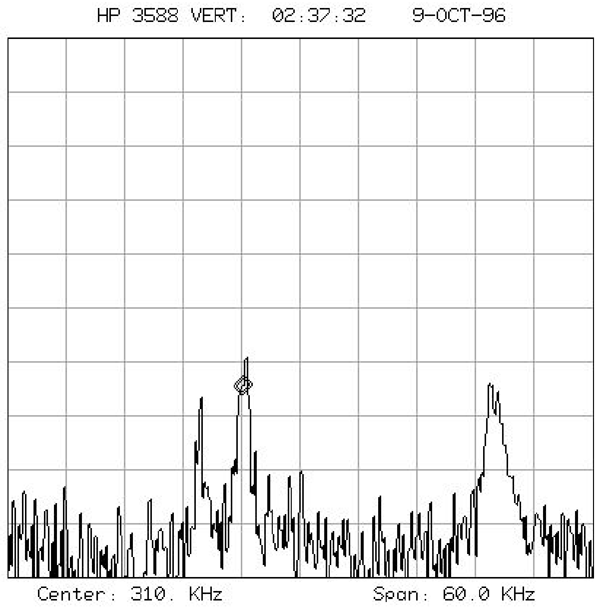

Figure B.91: STD_00002921.GIF

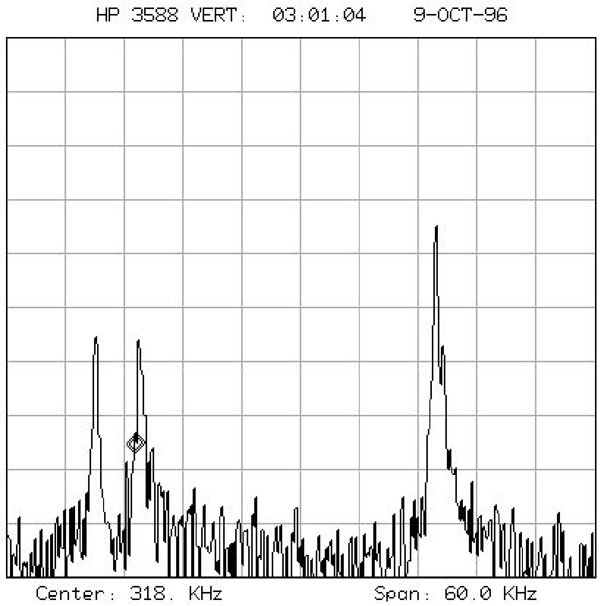

Figure B.92: STD_00002922.GIF

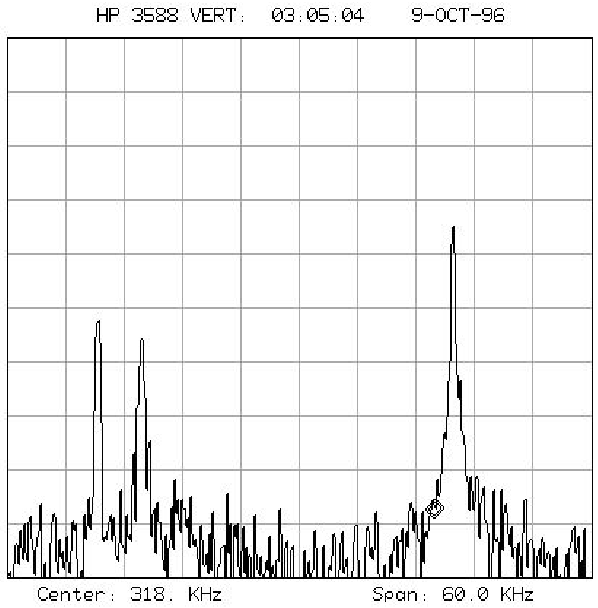

Figure B.93: STD_00002923.GIF

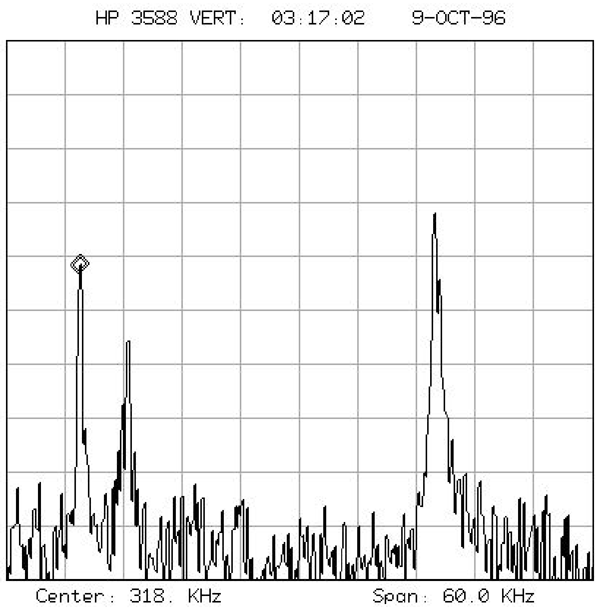

Figure B.94: STD_00002924.GIF

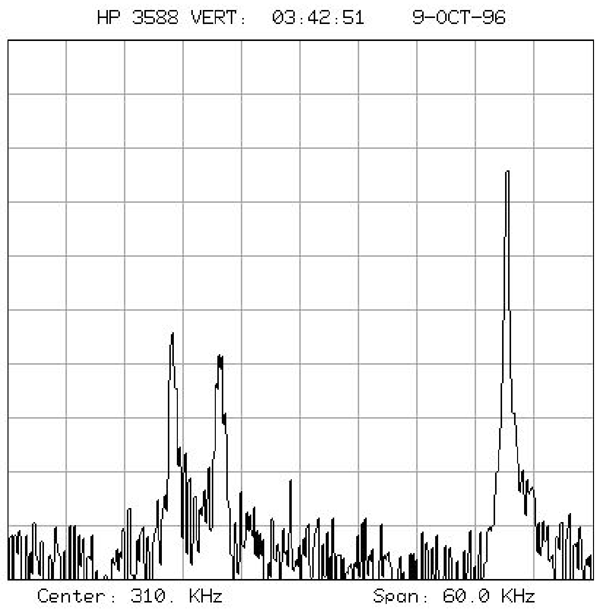

Figure B.95: STD_00002925.GIF

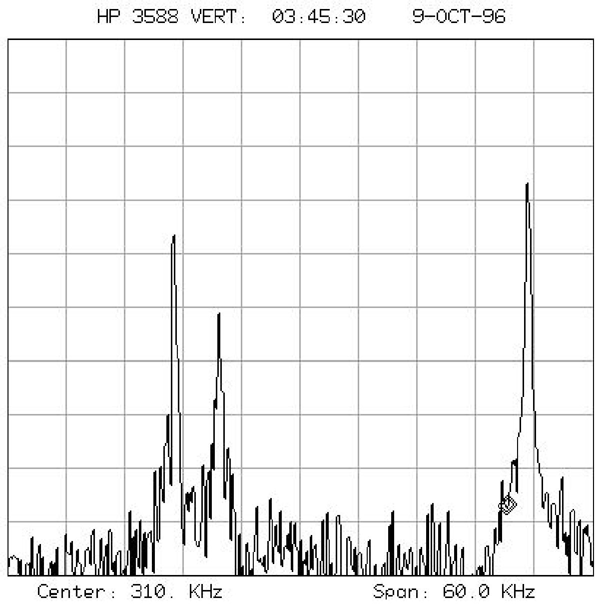

Figure B.96: STD_00002926.GIF

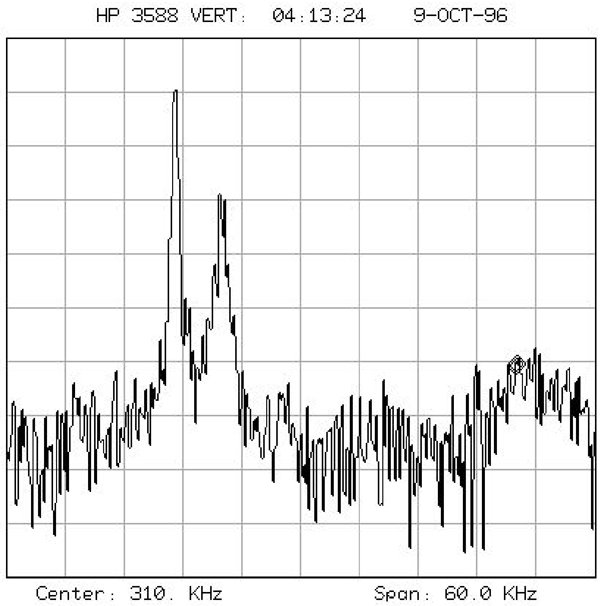

Figure B.97: STD_00002927.GIF

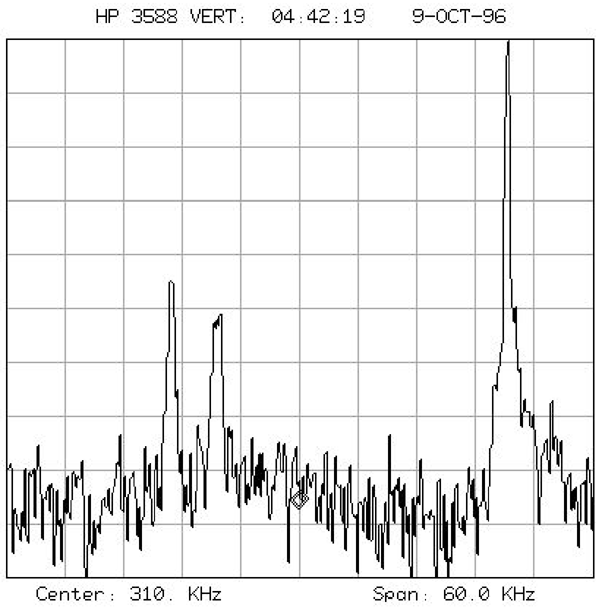

Figure B.98: STD_00002928.GIF

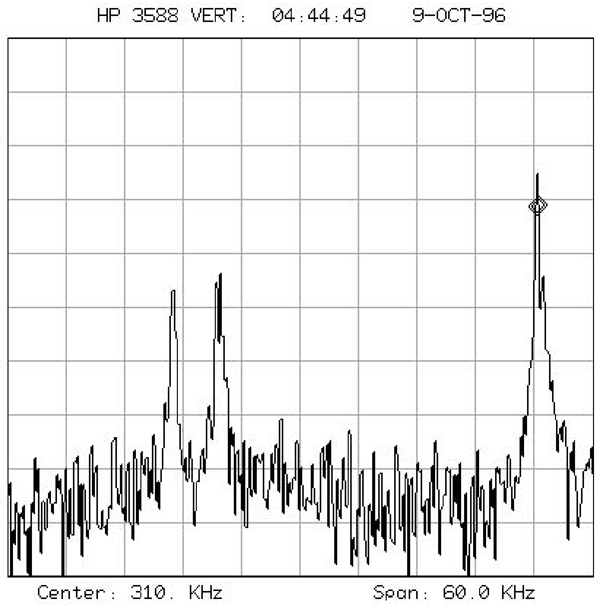

Figure B.99: STD_00002929.GIF

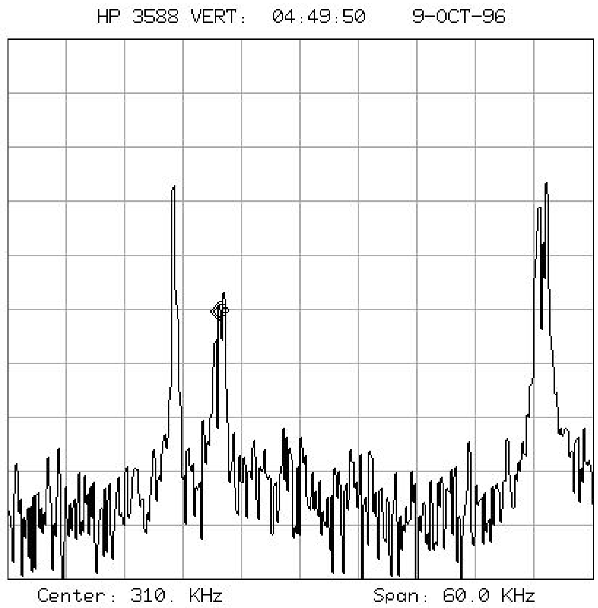

Figure B.100: STD_00002930.GIF

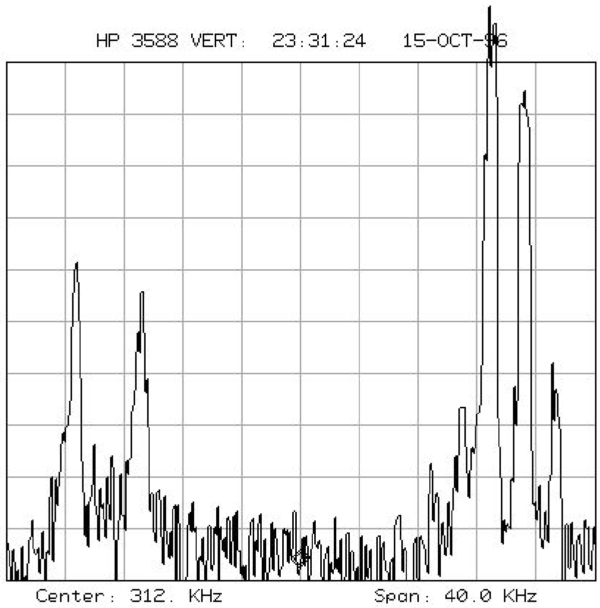

Figure B.101: STD_00002921.GIF

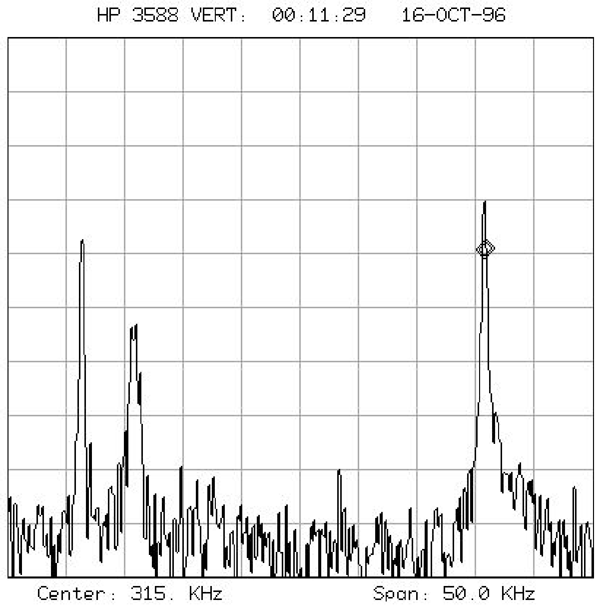

Figure B.102: STD_00002975.GIF

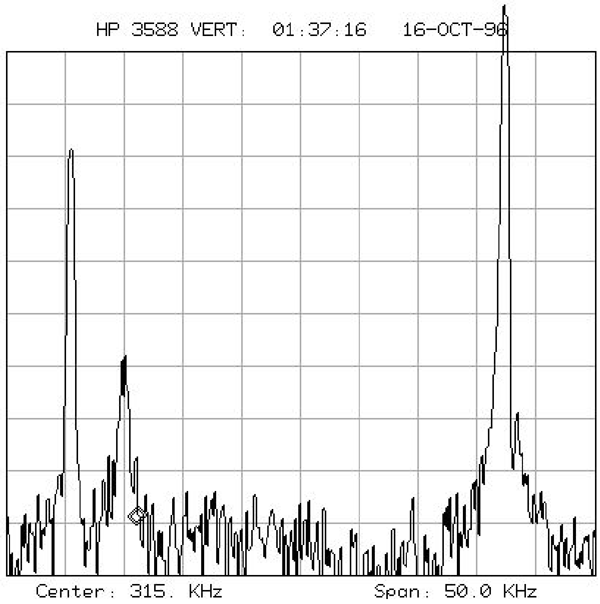

Figure B.103: STD_00002976.GIF

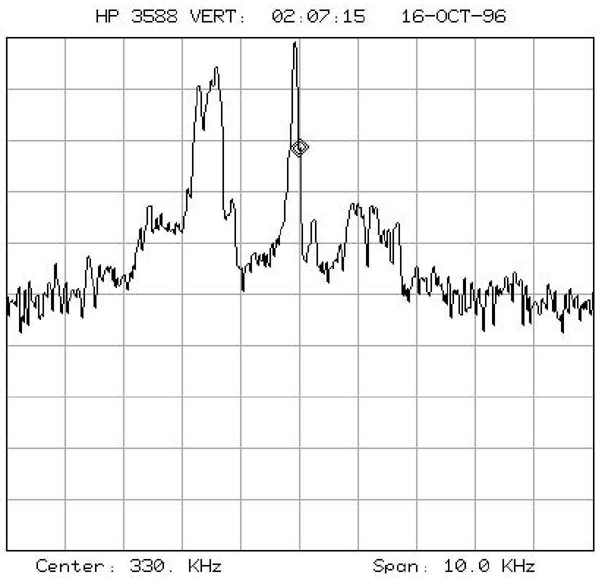

Figure B.104: STD_00002977.GIF

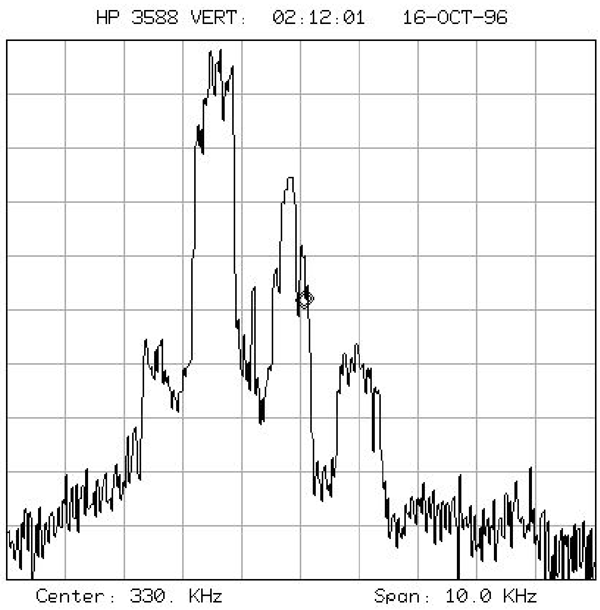

Figure B.105: STD_00002978.GIF

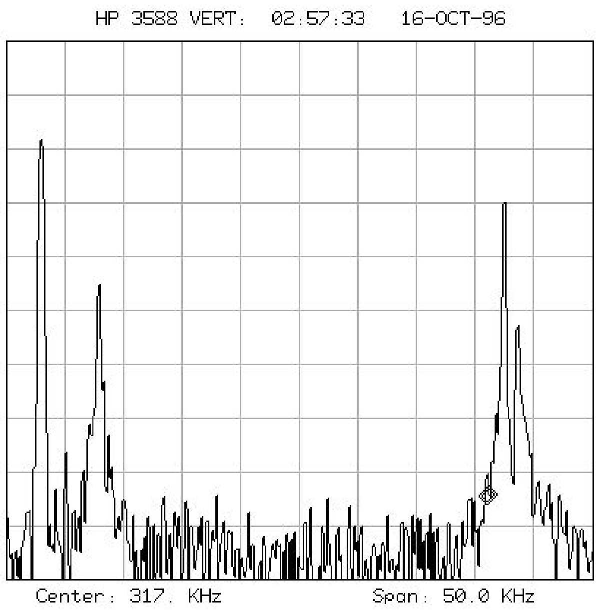

Figure B.106: STD_00002979.GIF

REFERENCES

[1] R. Talman. The Mobius accelerator. *Phys. Rev. Lett.*, 74:1590, 1995.

[2] S. Krishnagopal and R. Siemann. In *IEEE Proc. Int. Conf. Magnet. Technol.*, page 836, 1989.

[3] Richard Talman. Colliding Beam Note CBN 97-16, 1997.

[4] Peter Paul Bagley. *Experiment and Simulations with Nearly Equal Horizontal and Vertical Focussing: Single and Colliding Beam Results from the Cornell Electron Storage Ring (CESR).* PhD thesis, Cornell University, May 1995.

[5] E. D. Courant and H. S. Snyder. Theory of the alternating-gradient synchrotron. *Annals of Physics*, 3:1–48, 1958.

[6] J. Seeman. Cornell Laboratory of Nuclear Studies Reports CLNS 82/531, 1982.

[7] A. Piwinski. Observation of beam-beam effects in PETRA. *IEEE Trans. Nucl. Sci.*, 26:4268, 1979.

[8] Richard Talman. Multiparticle phenomena and Landau damping. In *Physics of Particle Accelerators*, page 789, New York, 1987. American Institute of Physics. AIP Conference Proceedings No. 153.

[9] Kohji Hirata. The beam-beam interaction: Coherent effects. In *Beam Dynamics Issues of High-Luminosity Asymmetric Collider Rings*, page 175, New York, 1990. American Institute of Physics. AIP Conference Proceedings No. 214.

[10] Kaoru Yokoya and Haruyo Koiso. Tune shift of coherent beam-beam oscillations. *Part. Accel.*, 27:181–186, 1990.

[11] R. E. Meller and R. H. Siemann. Coherent normal modes of colliding beams. *IEEE Trans. Nucl. Sci.*, 28:2431, 1981.

[12] Y. I. Alexahin. On the Landau damping and decoherence of transverse dipole, oscillations in colliding beams. Technical Report CERN-SL-96-64, 1996.

[13] Haruyo Koiso et al. Measurement of the coherent beam-beam tune shift in the TRISTAN accumulation ring. *Part. Accel.*, 27:83–88, 1990.

[14] Matthew Sands. The physics of electron storage rings: An introduction. Technical Report SLAC-121, 1970.

[15] D. A. Edwards and L. C. Teng. Parametrization of linear coupled motion in periodic systems. *IEEE Trans. Nucl. Sci.*, 20:885, 1973.

[16] S. Peggs. Coupling and decoupling in storage rings. *IEEE Trans. Nucl. Sci.*, 30:2460, 1983.

[17] Peter P. Bagley and David L. Rubin. Correction of transverse coupling in a storage ring. In *Proceedings of the 1989 IEEE Particle Accelerator Conference*, page 874, 1989.

[18] M. Billing. The theory of weakly coupled transverse motion in storage rings. Colliding Beam Note CBN 85-2, 1985.

[19] S. Peggs. The projection approach to solenoid compensation. *Part. Accel.*, 12:219–229, 1982.

[20] S. K. Kowalski and H. Enge. In *Proc. Int. Conf. Magnet. Technol.*, page 181, 1972.

[21] Hermann Wollnik. *Optics of Charged Particles.* Academic Press, Orlando, 1987.

[22] D. Rubin. Solenoid compensation in micro-beta lattices. CESR Operations Note CON 84-5, 1984.

[23] John Theodore Seeman. *Injection Process of the Cornell Electron Storage Ring CESR.* PhD thesis, Cornell Univerity, May 1979.

[24] L. Schachinger and R. Talman. TEAPOT: A thin element accelerator program for optics and tracking. *Part. Accel.*, 22:35, 1987.

[25] D. Rubin. Personal communication.

[26] D. A. Edwards and M. J. Syphers. *An Introduction to the Physics of High Energy Accelerators.* John Wiley & Sons, New York, 1993.

[27] S. Henderson et al. Investigation of chromaticity sharing at the Cornell Electron Storage Ring. In *Proceedings of the 1997 Particle Accelerator Conference.*

[28] Stephen Val Milton. *The Beam-Beam Interaction in Electron Storage Rings: A Study of the Weak/Strong Case.* PhD thesis, Cornell University, January 1990.

[29] S. Peggs. Beam-beam synchrobetatron resonances. *IEEE Trans. Nucl. Sci.*, 30, 1983.

[30] Gerald Peter Jackson. *The Theory, Simulation, and Measurement of the Cornell Electron Storage Ring Luminosity Performance.* PhD thesis, Cornell Universtiy, January 1988.

[31] T. Koyama, N. Malitsky, and R. Talman. Beam-beam simulation using the unified accelerator libraries. In *Proceedings of the 1997 Particle Accelerator Conference.*

[32] R. Talman. Memo to Möbius group.

[33] R. Talman. Personal communication.

[34] Stephen Val Milton. *A synchrotron light monitor using charged coupling device technology.* Master's thesis, Cornell University, May 1988.

[35] Omnibyte Corporation, 245 West Roosevelt Road, West Chicago, Illinois 60185. *COMET™: VMEbus I/O Board Multi-Channel Analog Digitizer Reference Manual*, February 1994.

[36] Ryan Scott Smith. *Measuring the coherent beam beam effect.* Master's thesis, Cornell University, May 1997.

[37] Michael Billing. Method for deducing particle distribution functions from scraper data. Colliding Beam Note CBN 82-43, 1982.